This is to certify that the

dissertation entitled

A NEW APPROACH TO MEASURING INSTANEOUS FLOW RATES IN UNSTEADY DUCT FLOWS

presented by

Mahmood Ahmad Akhtar Rahi

has been accepted towards fulfillment
of the requirements for

Ph.D. degree in MECHANICAL ENGINEERING

Major professor

Date 25th April 2002

A NEW APPROACH TO MEASURING INSTANTANEOUS FLOW RATES IN UNSTEADY DUCT FLOWS

B y

Mahmood Ahmad Akhtar Rahi

A DISSERTATION

Submitted to
Michigan State University
in partial fulfillment of the requirements
for the degree of

DOCTOR OF PHILOSPHY

Department of Mechanical Engineering

2002

ABSTRACT

A New Approach to Measuring Instantaneous Flow Rates in Unsteady Duct Flows

By

Mahmood Ahmad Akhtar Rahi

In transient duct flows, there are presently few reliable techniques for measuring instantaneous flow rates accurately. Although transient flows have been studied previously the understanding gained has not led to improved unsteady flow metering devices. The main outcome has been to link steady and unsteady flows through semi-empirical relations. One possible path to devising an accurate measurement technique is through relationships from the solved, unsteady fluid mechanics equations; however this has not been undertaken. In this thesis, solutions to unsteady, fully developed Navier-Stokes equations and Reynolds averaged momentum equations are found and tested in an experimental test facility that emulates a prototype instantaneous unsteady flow metering device.

In the case of laminar flow metering, unsteady, fully developed Navier Stokes equations are solved to express the flow rate as a functional of pressure drop. The solution consists of a quasi-steady term which is supplemented by an unsteady correction term. This unsteady correction term is a convolution integral of the product of momentary pressure drop and a weighting function. This unsteady correction term is an analytically exact description of the flow history and is necessary in unsteady duct flows. In order to ascertain the feasibility of unsteady flow metering, an experimental test facility was

designed and fabricated, with miniature pressure sensors embedded in a long transparent acrylic pipe to measure the instantaneous pressure drop. The momentary flow rate was then inferred from the pressure-drop functional and compared with the instantaneous flow rate as inferred from the cumulative collected flow. In test experiments, the principle appears to work perfectly for duct flows with arbitrary unsteadiness histories.

A similar approach was adopted for unsteady turbulent flow metering. In this approach Reynolds averaged momentum equations were solved with a modified eddy viscosity model incorporating a time delayed or history response to the turbulence. This model represents the averaged eddy viscosity across the duct and was tested against the experimental data for changes in the Reynolds shear stress during imposed transients. The solution of the Reynolds averaged momentum equation is similar to the laminar flow result of flow rate as a functional of pressure drop and consists of a quasi steady term augmented by an unsteady correction term incorporating an eddy viscosity. Using the same experimental facility, test experiments revealed that this approximate approach seems to work reasonably accurate in prediction of instantaneous flow rates in unsteady turbulent duct flows.

This thesis is dedicated to my parents

Bashir Ahmad Akhtar (late)

&

Salima Akhtar

For their love, kindness and prayers for my success

ACKNOWLEDGMENT

I would like to pay special thanks to a few important people:

First, I would like to extend my sincere gratitude to Dr. Giles Brereton, my Major Professor, for being my adviser, and for his support and patient guidance throughout my thesis work and studies.

I would also like to extend my sincere thanks to member of my committee Dr. Harold Schock, Dr. Tom Shih, Dr. Ahmed Naguib and Dr. Milan Miklavcic, for being on my committee, their helpful comments and thought provoking questions. I would also like to thank Dr. Kyle Judd for his valuable comments and, Tom Stueken for his help in fabrication of tallest structure in the lab for this research, and for his cheerful company. I would also like to thank my fellows at MSUERL, for their day to day guidance and their wonderful company; Mark Novak, Edward Timm, Anthony Christie, Boon Keat Chui, Yuan Shen, Andrew Sasak and Andrew Fedewa.

Finally, my wife Rashda, for her patience and support throughout my Masters and Ph. D. Program, and my mother without whose prayers and encouragements this day would not have been possible.

TABLE OF CONTENTS

LIST OF TABLES

LIST OF FIGURES

NOMENCLATURE

English Symbols

Name	Meaning	Units
$A(x)$	local duct cross-sectional area	m^2
C	Constant	-
D	Diameter of pipe	m
D_s	Sensor diameter	m
E	Excitation voltage	volts
E_o	Output voltage	volts
E_i	Input voltage	volts
E	Modulus of elasticity (equation (C.1))	N/m^2
$F(t)$	pressure gradient defined as $F(t)=\frac{1}{\rho}\frac{\partial p}{\partial x}$	m/s^2
g	Acceleration due to gravity	m/s^2
$h(t)$	Weighting function defined in equation 2.22	-
$H(t)$	Heaviside step function	-
h	Water column height	m
J_0	Bessel function of first kind order zero	-
J_1	Bessel function of first kind of order 1	-
$\mathcal{J}_1$	ratio of Bessel functions, J_0/J_1	-

K	Bulk modulus of fluid	N/m^2
$K(t')$	Weighting Function defined in equation 2.19	-
K	Thermal conductivity	W/m^2K
L	Length of pipe	m
$\dot{m}$	Mass flow rate	Kg/s
P_0	Initial pressure	Pa
p	Pressure	Pa
p'	Transient component of pressure	Pa
P	Axial load	N
Q	Heat generated defined as $Q=\left(E^2/\mathbb{R}\right)\times t$	Joules
Q_s	Heat loss to the substrate	Joules
r	distance from pipe axis	m
R	Radius of the pipe	m
$\mathbb{R}$	Sensor impedance	Ohms
s	Frequency domain variable	s^{-1}
S_g	Gauge factor	-
t	Time	s
Re_{ta}	Time averaged Reynolds Number	-
Re_D	Reynolds number based on diameter	-
U_τ	Friction velocity	m/s
U^*	Friction velocity	m/s
u'	Transient component of the velocity	m/s
u_0	Initial velocity	m/s

U	Mean velocity	m/s
U_{cL}	Center line mean velocity	m/s
v	Velocity	m/s
v_x	Velocity in axial direction	m/s
v_r	Velocity in radial direction	m/s
v_Θ	Velocity in circumferential direction	m/s
$W(t)$	Weighting function	-
$u'v'$	Reynolds shear stress	m^2/s^2

Greek Symbols

α	Dimensionless frequency as $\alpha = R(\omega/\nu)^{1/2}$	-
τ	Dimensionless time parameter $\tau = \nu t/R^2$	-
τ_0	Shear Stress at the wall	N/m^2
τ_w	Shear Stress at the wall	N/m^2
ρ	Density	kg/m^3
μ	Dynamic viscosity	$N\text{-}s/m^2$
ν	Kinematic Viscosity	m^2/s
ν	Poisson's ratio	-
$\lambda_u(t)$	Instantaneous friction factor	-
λ_q	Quasi-Steady friction factor	-
λ_s	Quasi-steady friction factor	-
ω	Oscillating frequency	Rad/s

ε^*	$\varepsilon^* = \varepsilon + \Delta\varepsilon$ Time dependent eddy viscosity	m^2/s
ε	Quasi-steady eddy viscosity	m^2/s
ε	Strain	-
ε_a	Axial strain	-
ε_t	Transverse strain	-
$\Delta\varepsilon$	Oscillatory component of eddy viscosity	m^2/s
δ	Dirac delta function	-
$\mathcal{L}^{-1}$	Inverse Laplace transform	-

Acronyms

FFT	Fast Fourier Transform
LDV	Laser Doppler Velocimeter
DAC	Data Acquisition and Control
STC	System Timing Controller
PGIA	Programmable Gain Instrument Amplifier
TZS	Thermal Zero Shift
FSO	Full Scale Output
TSS	Thermal Sensitivity Shift
os	Oscillatory components
ta	Time averaged component
$\widehat{(\,)}$	Laplace transformed variable

Chapter 1 Introduction

1.1 Statement of the Problem

In transient duct flows, there are presently no reliable techniques to measure instantaneous flow rates accurately. The quasi-steady approach is generally used in most of the unsteady flow measurements, provided that frequencies of pulsation or transients are small. The common practice has been to relate steady and unsteady flows using semi-empirical relations. The need for instantaneous flow rate measurement arises for the following reasons:

i). Unsteady flow with spatial pressure gradients fluctuating around non-zero values occur frequently in nature and engineering. Similarly transient flows are important and found in many situations. Accurate measuring techniques are needed for them.

ii). While transient flows have been studied previously, the understanding gained has not led to improved flow metering devices and devices which use steady flow approximations are inaccurate. The recent series of laboratory tests carried out by Arasi [1] indicates that orifice or venturi meters give seriously inaccurate results for pulsating flows.

iii). As there is no generality in the time-dependence of unsteady flow, it seems that a transient flow metering solution must be based on time-dependent solutions to the unsteady fluid mechanics equations, though this has not yet been done.

iv). There are quite a number of theoretical and experimental accounts of steady flow through ducts and pipes. However, unsteady flow analysis is relatively limited. While

there is a well-developed theory concerning the energy loss in steady pipe flow, very limited knowledge exists about the nature of energy dissipation in unsteady flow systems.

v). With the ever-increasing development of microelectronics, real time data is easier to obtain and process. In order to improve the real time measurements of unsteady flow rates, there is a great demand for improving and elucidating flow metering systems. There is also a demand for a new real time flow sensor with improved performance, in terms of high accuracy and fast response under time varying conditions.

vi). In bio-fluid engineering, many flows are pulsating. Many engineering flows are also unsteady, predominantly in dynamic equipment such as reciprocating engines, turbo-machinery, and control valves; these kind of equipment create pulsations with frequencies that are a function of the rate of revolution and its harmonics. Similarly, in the intake and exhaust manifold of an internal combustion engine, we encounter accelerating, decelerating and reversing flows. The fluid flow in hydraulic and pneumatic lines and control systems often pulsate. Unsteady flows are also encountered in aerodynamics, wind engineering and liquid propellant rocket system. However, there are no means available to predict the momentary flow rates through these unsteady flow devices accurately.

Several methods for estimating the unsteady laminar flow rates have been proposed that uses flow parameters that are functions of the instantaneous mean velocity and acceleration. In sinusoidally varying flows, the velocity amplitudes, the velocity phase shifts, and unsteady flow parameters are often expressed or modeled as functions of the dimensionless parameter $\alpha = R(\omega/\nu)^{1/2}$. When flow varies arbitrarily with time, the instantaneous values of flow parameters can now be expressed as functions of the

instantaneous velocity, pressure gradient or shear stress and the weighted past changes of these quantities, in which the weighting function depends on the dimensionless time parameter $\tau = \nu t / R^2$. In this chapter, a review of the related work in transient or unsteady flows, both in laminar and turbulent regimes is undertaken. The motivation for the present study will be discussed in the end of this chapter.

1.2 Review of Laminar Flow Studies

Many investigators have studied pulsatile and oscillatory flows theoretically, which are two representative types of unsteady flows. Analytical and numerical solutions of continuity, momentum, and energy equations can be found in the laminar regime but are limited as a result of mathematical complexities involved. Analytical solutions are particularly difficult to obtain because of the non-linearity of the governing equations when solving in more than one dimension. However many researchers have attempted numerical and approximate solutions of these equations when restricted to Newtonian fluids.

1.2.1 Unsteady Laminar Flow-Theoretical Background

Early studies of the Navier-Stokes equations in parallel duct flows focused on those with specific time dependent pressure gradients. Sexl [2] developed an analytical solution to the momentum equation for a Newtonian fluid flow in a horizontal circular pipe subjected to a pressure gradient of the form $dp/dx = Ce^{i\omega t}$. He found an exact solution of the Navier-Stokes equations, which resulted in an expression for the velocity distribution throughout the cross section. Shortly thereafter, Szymanski [3] in 1932, using a similar technique, developed an analytical solution to the momentum equation for a flow subjected to a step change in pressure gradient such that $dp/dx = 0$ for $t \le 0$ and $dp/dx = C$ for $t \ge 0$, where C is a constant. The time dependence of the axial velocity in both of the solutions

was assumed to be of the form $u = F(r)e^{i\omega t}$, where $F(r)$ was expressed in terms of Bessel functions. For the non-periodic case, he gave another exact solution to Navier-Stokes equation with the pressure gradient varying as a Heaveside unit step function.

Uchida [4] developed solutions which were variations on Sexl's oscillatory pressure gradient flow, by superimposing the oscillations on a constant pressure gradient with $dp/dx = 0$ for $t \leq 0$ and $dp/dx = Ce^{i\omega t}$ for $t \geq 0$. He presented an exact solution of pulsating laminar flow superposed on the steady flow in a circular pipe. His calculations showed that in rapid pulsations, fluid velocity at the centerline had a phase lag of 90° behind the pressure gradients and its amplitude diminished with increasing frequency. In addition his calculations showed that the phase of the sectional mean velocity is delayed behind that of the pressure gradient while that of shearing stress is delayed less.

Womersley [5] considered the oscillatory flow of a Newtonian fluid studied by Sexl and Szymanski from a biological perspective by using both rigid and elastic pipe walls. Womersley also analyzed the phase relationship between the pressure gradient and resulting velocity field. Womersley showed that, in oscillatory flow, the interaction between viscous and inertial effects altered the velocity profile so that it no longer resembled the parabolic shape of a steady flow. He noticed that the resistance and inertance to flow could be expressed as a function of a single non-dimensional parameter called the Womersley parameter, $\alpha = R(\omega/\nu)^{1/2}$, where R is the span of the tube, ω is the oscillation frequency and ν is kinematic viscosity, though the function would clearly depend on the kind of unsteadiness encountered.

In summary, analytical solution for velocity profiles in some unsteady flows with particular time dependences have long been known. However, these studies have not led to ways in which the instantaneous flow rate in arbitrarily unsteady flows might be expressed as a simple function of pressure gradient, as might be useful for design of unsteady flow meters.

1.2.2 Development of Transient Response Theory and Experimental Verifications

The early investigations on unsteady fluid flow in straight pipes were based on linearized two-dimensional Navier-Stokes equations. Their main purpose was either to analyze the surging phenomena, "water hammer", or to evaluate the energy loss due to fluid friction. Hence, most of the attention was given to the transient response of the fluid lines with frequency dependent friction. Therefore, in the 1950's most research was focused on the frequency response characteristics of the fluid lines. It was later reported by Leonhard [6] that it is theoretically possible to convert frequency response results to transient response results.

Based on constant viscosity Navier-Stokes equations, Brown [7] derived the operator forms of the basic transmission parameter, called the "propagation operator" and characteristic impedance. The propagation operator was expressed as $\Gamma(s) = l\sqrt{Y(s)Z(s)}$, where l was the distance separating the two stations and Y(s) and Z(s) were the shunt admittance and series impedance of the fluid transmission line. Given the end conditions, this propagation operator and the characteristic impedance could be easily applied to determine either frequency or transient response. With the help of these operators, Brown was able to describe the effect of frequency dependent viscosity on the propagation of acoustic waves in fluid transmission lines and provided an analysis for impulse and step

transient decay in lines. However, he neglected the variations of the pressure gradient and velocity along the length of the line.

Brown and Nelson [8] presented further solutions of step responses to small signal disturbances for rigid cylindrical lines containing Newtonian, incompressible liquid in laminar flow. They concluded that the pressure, flow step inputs, and flow outputs for semi-infinite lines containing constant viscosity fluid can, with the principle of superposition, be used to estimate the responses of a network of lines for any transient input.

D'Souza and Oldenburger [9], using the basic Navier-Stokes equations, derived a transfer matrix relating the dynamic pressure and cross-sectional average velocity for small diameter hydraulic lines. They then compared the theoretical results with experimental data obtained from a frequency response run on a half-inch inner diameter test tube. It was then proposed that the dynamic response of small diameter lines could be predicted correctly by including the effect of viscosity and compressibility while deriving the transfer function of the pipe with sinusoidal input. These transfer functions related the pressure and cross-sectional average velocity variables at two cross sections of the line.

Holmboe and Rouleau [10], performed two experiments to display the effect of viscous shear on transients in liquid lines. These experiments included a propagation of a short, rectangular pulse of pressure in a cylindrical tube with initially undisturbed liquid and a pressure surge resulting from a step change of flow in a pipe. The experimental data confirmed Brown's [7] constant viscosity transmission parameter theoretical results. They also noted that in the pulse propagation and water hammer experiments, the one-dimensional analysis, utilizing a frequency dependent shear term, is valid and can

accurately predict the distortion and decay of transients in a constant diameter line filled with viscous fluid.

The analytical expressions of Brown, D'Souza and Oldenburger were very complex. In these expressions frequency dependent effects were deduced from the linear theory of transfer operators for pressure and flow at two cross sections of the pipe. These transfer operators required all input functions to be expressed as a summation of step functions, and in addition all reflections had to be taken into account individually. This became somewhat tedious for complicated systems consisting of series, branches or parallel pipes. In the method of characteristics, all reflections could be considered automatically and complicated systems could be handled without significantly increasing the difficulty.

Zielke [11], using the method of characteristics, included the effect of the time varying velocity profile in unsteady laminar flow, deduced from a solution to the one dimensional Navier-Stokes equation. He solved the problem of transient variation of the flow exactly relating the wall shear stress to the instantaneous mean velocity and to the weighted past velocity changes. It constituted a friction law for fully developed pipe flow undergoing arbitrary unsteadiness from an initially steady state. Therefore exact calculations of laminar wall friction in transient fully developed pipe flows could be made, provided that the history of the bulk flow acceleration at all earlier times in the transients were known. This solution took the form:

$$\tau_0(t) = \tau_0(0) + \int_0^t \left[\frac{\partial U}{\partial t}(t-t') - \frac{\partial U}{\partial t}(0)\right] \mathcal{L}^{-1}\left\{\frac{\rho R}{\mathcal{J}_1\left(i\sqrt{s/\nu R}\right) - 2}\right\} dt' \qquad (1.1)$$

or

$$\tau_0(t) = \tau_0(0) + \int_0^t \left[\frac{\partial U}{\partial t}(t-t') - \frac{\partial U}{\partial t}(0) \right] W(t')\,dt' \tag{1.2}$$

where $W(t)$ is the weighting function, τ_0 is the wall shear stress, U the bulk flow velocity, $\mathcal{L}^{-1}$ an inverse Laplace transform operator, R the pipe radius, and $\mathcal{J}_1$ the ratio of Bessel functions, J_0 to J_1.

The practical significance of Zeilke's result was that momentary pressure gradients depend on both local flow conditions and all previous ones, in flows of arbitrary unsteadiness. Comparison of the theoretical results with experimental data of Holmboe and Rouleau showed good agreement and an accurate prediction of the distortion effects. His solution was expressed in terms of the dimensionless time τ, given by

$$\tau = \frac{\nu}{R^2} t \tag{1.3}$$

Zielke used two distinct series for approximating the inverse Laplace transform in equation (1.1) or weighting function $W(t)$, one for τ greater than ~ 0.02 and second for values of τ smaller than ~ 0.02. This method was also considered expensive in terms of computer time, since it required excessive computer storage and computation time, and was considered to be impractical for analysis of large fluid systems.

Trikha [12] developed a method for simulating frequency dependent friction based on Zeilke's result, which was claimed to make the inclusion of the frequency dependent friction in the method of characteristics almost as convenient and practical as the inclusion of steady state friction. He also proposed an approximate weighting function to replace the

inverse Laplace transform in Zielke's expression, which offered the advantage of not requiring the storage of mean velocity at all earlier times. Tsang et al. [13] used the FFT method to predict the dynamic behavior of air transmission lines subjected to an impulse, step or arbitrary excitation. The calculation procedure was considered relatively simple, while the numerical results showed good agreement with experimental measurements.

Lisheng and Wylie [14] also proposed a numerical method to compute the transients in complex systems with various frequency dependent factors. They demonstrated the application of numerical schemes to solve problems of water hammer and transients in pipes with frequency dependent friction. Comparisons of computed results with the standard method of characteristics and with physical experiments of Holmboe and Rouleau [8] showed good agreement. Both Trikha, and Lisheng and Wylie's methods are discretized implementations of Zielke's result, in which the 'memory' of earlier transients is truncated at a convenient point.

The major disadvantage of Zielke's [11] solution is that it cannot be implemented easily for large fluid systems because of large memory requirements. In contrast Trikha's weighting function was an approximate expression, constructed by adding three exponential terms and did not match well with the exact weighting function of Zielke for τ less than 0.00005. Brereton [15], using Zielke's technique, solved the reciprocal problem of deducing the momentary flow rate from wall friction or pressure gradient. The potential advantage of his solution was its applicability for devising sensors for accurate measurement of unsteady flow. He also introduced the approximation to Zielke's weighting function to reduce the storage requirements, by retaining only the most recent flow rate history, and thus improving its practicality for predicting the transient behavior of large

fluid systems. Using the numerical inverse Laplace transform techniques, his expressions provided a means of expressing momentary wall friction in terms of bulk-flow acceleration history, like Zielke's expressions and reciprocal expressions for flow rates and cumulative through flow as functions of recent wall friction and pressure gradient histories. His solution took the form:

$$\int_0^t U(t)\,dt' = -\frac{R^2}{8\nu}\int_0^t \frac{1}{\rho}\frac{\partial p}{\partial x}(t')\,dt' + \frac{R^2}{\nu}\int_0^t \left(\frac{1}{\rho}\frac{\partial p}{\partial x}(t-t') - \frac{1}{\rho}\frac{\partial p}{\partial x}(0)\right) K(t')\,dt' \quad (1.4)$$

where $K(t)$ is a different weighting function to $W(t)$ in equation (1.2). These expressions consisted of two terms: first term describing the steady flow behavior for viscous, Newtonian fluid in pipes; and a second term incorporating the unsteady flow corrections based on the pressure gradient or wall friction history.

1.2.3 Experimental Studies on Flow Rate, Friction Factor and Velocity Profile Measurements under Transient Flow Conditions

Kataoka, Kawabata and Miki [16] studied the transient start up response of pipe flow to step inputs of constant flow rate, using an electrochemical technique to measure the velocity profile with velocity electrodes. They noticed that the velocity profile development for the step input had a different trend from that of steady flow development at different positions in the entrance region of the pipe. The velocity profiles showed minima at the pipe centerline axis and a maximum in the intermediate region between the axis and the wall as a result of non-uniformity of the acceleration in the central core.

Muto and Nakane [17] derived an expression for the velocity distribution in a laminar pulsating flow through a rigid circular tube. Transitions of velocity distribution with respect to time were then measured by a flow visualization technique using aluminum

powder suspended in the fluid and photography of the path lines. The experimental data were in good agreement with their theoretical results. They noticed that the velocity distribution varied gradually from an initial rectangular like shape to a parabolic one at steady state. In pulsating flows, they observed that the velocity profile developed in the positive flow direction at all times provided the ratio of the amplitude of the oscillating component of the flow to the steady component was near unity. If this ratio was increased to 2, then the velocity profiles during transition developed in the negative direction as well.

Kurokawa and Morikawa [18] studied accelerated and decelerated flows in a circular pipe in both laminar and turbulent regimes. They noticed different patterns in the formation of sectional velocity profiles and in transition to turbulence. For relatively large accelerations, the flow was characterized by the velocity profile of a wide potential core and a narrow boundary layer. In contrast, when deceleration was imposed, the variation of the velocity profile was comparatively small compared to the quasi-steady flow and this variation became larger with increased deceleration. They also noted that the friction coefficient of an accelerated flow was larger than that of the quasi-steady flow, in the laminar region, and that this trend was opposite in the turbulent regime.

Ohmi and Iguchi [19] investigated the relationship between frictional losses and dimensionless sinusoidal frequency in terms of the instantaneous friction factor $\lambda_u(t) = 8\overline{\tau}_w / \rho \overline{U}^2{}_m$. They characterized the flow in three distinct flow pattern regions based on the dimensionless frequency parameter. These parameters were defined as $\phi_{t,n} = \rho_0 n\omega |u_{m,os,n}| / \left(|\Delta p_{os,n}| / l \right), \phi_{z,n} = \left(4|\tau_{w,os,n}| / D \right) / \left(|\Delta p_{os,n}| / l \right), \alpha_{t,n} = \angle \left(\Delta p_{os,n} / l \right) - \angle u_{m,os,n}$, and $\alpha_{t,n} = \angle \left(\Delta p_{os,n} / l \right) - \angle \tau_{w,os,n}$. Here τ_w is wall shear stress, D is pipe diameter, Δp is the

pressure drop, ω is the angular frequency, and n denotes quantities associated with the nth harmonic in the finite Fourier expansion, while *os* denotes an oscillating component. These regions were the quasi-steady, intermediate and inertia-dominant regions based on the relative value of the non-dimensional frequency. They concluded that the instantaneous friction factor $\lambda_u(t)$ in oscillatory flow was almost equal to the quasi-steady friction factor λ_q in the quasi-steady region. In the intermediate region and inertia-dominant regions $\lambda_u(t)$ was always larger than λ_q in the acceleration zone of the oscillation cycle and it was larger than λ_q in the first part of the deceleration zone of the cycle. However this trend was reversed in the rest of the deceleration zone. Hershey and Song [20] found that above a certain limiting frequency of oscillation, friction factors were greater than their values for steady flow. Consequently, energy losses would be greater than would be expected for a quasi-steady model.

Yokota, Kim, and Nakano [21] proposed a new approach for estimating unsteady flow rates through pipe lines and other components in real time. They demonstrated that unsteady flow rate could be tenuously estimated by using pipeline dynamics containing hydraulic oil and measured pressures at two distant locations along the pipeline. They measured pressure and flow rates at two distinct locations under the unsteady laminar oil flow condition, and results were then compared with the cylindrical choke type instantaneous flow meter. The results were in good agreement with each other. In this approach, an empirical weighting function used for convolution was estimated experimentally, by using the Inverse Fast Fourier Transform technique, because, presumably they were unable to solve the Navier-Stokes equations.

1.3 Review of Turbulent Unsteady Flow Studies

The unsteady duct flows are mostly classified in two main categories: periodic oscillatory flows and non periodic transient flows. The pulsating periodic flows have captured much of the attention of researchers because of their practical importance and the experimental ease with which such flows can be generated. Generally, the investigations on turbulent unsteady flow have been focused on determining the effect of transients and pulsations on the velocity profiles, skin friction and turbulent intensity.

1.3.1 Periodic Turbulent Unsteady Flows

Relatively little attention has been paid to improving the prediction of skin friction in transient turbulent flows. In many flows transient effects are either neglected or allowed for only approximately when representing skin friction. This is understandable because of the resulting simplicity, but it is nevertheless misleading in some cases. Some experiments and theoretical results on frictional losses in incompressible pulsating turbulent pipe flows are reported below.

Schultz-Grunow [26] generated pulsating flow in a 11.5 feet long, 1.95 inch diameter smooth pipe. The instantaneous velocity was varied between 3.8 feet per second and 7.5 feet per second for a time period of oscillation of 2.5 seconds, and from 0.16 feet per second to 7.1 feet per second for 30 seconds. He noticed a strong similarity between velocity profiles of decelerated flow in a uniform pipe and steady flow in a divergent pipe. A similar resemblance was seen for accelerated flow in a straight pipe and steady flow in a convergent pipe. He concluded that the time averaged values of flow resistance were close to the steady state values. It should be noted that in transient flows the instantaneous value is of great importance.

Daily, Hanky, Olive and Jordaun [27] carried out experiments in a 8.5 feet long, and one-inch diameter pipe. They established a steady state flow and then subjected it to a slowly changing acceleration and then a deceleration. In the case of deceleration a rapid velocity change occurred in the start and became more continuous after some time. The range of acceleration and deceleration was between 7 and 80 ft/sec^2. They concluded that during acceleration, friction is slightly higher than the equivalent steady state value, and during deceleration friction is appreciably less than the equivalent steady state value. They also concluded that the initial state from which the flow is initiated affects the subsequent flow history.

Kirmse [28] carried out measurements of velocities and pressure gradients in a pulsating turbulent pipe flow by means of directionally sensitive LDV (Laser Doppler Velocimeter) and inductive pressure transducers. His results suggest that the temporal average over one period of the measured pressure gradient was always larger than the spatial pressure gradient of a quasi-steady turbulent flow of the same averaged Reynolds number. Similarly, results for the Darcy-Weisbach friction factor were between 5 and 10 % larger than in the corresponding steady flows. He also concluded that pulsating turbulent flow can not be correctly predicted by existing turbulence models based on the similarity of the turbulence structure of a stationary boundary layer flow on a flat plate.

Baired, Round and Cardenas [29] measured the frictional pressure drop over one pulsation cycle in a sinusoidally oscillating pipe flow. They showed that the experimental values of the pressure gradient term $\Delta p/L$ agreed well with the values calculated from the integrated form of the one-dimensional momentum equation of the form:

$$\frac{1}{\rho}\frac{\partial p}{\partial x}+\frac{\partial u}{\partial t}+\frac{\lambda_s u^2}{2D}=0 \tag{1.5}$$

Here λ_s was calculated using the Karman-Nikuradse equation with coefficients adjusted to fit the data as $1/\sqrt{\lambda_s}=1.746ln\left(\mathrm{Re}_{ta}\sqrt{\lambda_s}\right)-9.195$. They concluded that the quasi-steady state model was valid within their experimental range. The limiting value of dimensionless frequency in this case was $\alpha_q \geq 0.025\,\mathrm{Re}_{ta}$ where Re_{ta} is a time averaged Reynolds number.

Ohmi and Iguchi [30] estimated friction factors in a pulsating pipe flow from flow pattern diagrams and compared them with experimental data. They described the instantaneous friction factor $\lambda_u(t)=8\overline{\tau}_w/\rho\overline{U}^2{}_m$ and the time averaged friction factor $\lambda_{u,ta}=\left(8/\rho\overline{U}_{m,ta}{}^3T\right)\int_0^T\overline{\tau}_w\overline{U}_m dt$ as a function of $\alpha/\mathrm{Re}_{ta}^{3/4}$, where $\alpha=R(\omega/\nu)^{1/2}$. The instantaneous friction factor $\lambda_u(t)$ and the quasi-steady friction factor λ_q were almost equal in the quasi-steady region denoted by $\alpha/\mathrm{Re}_{ta}^{3/4}\leq 0.145$. With an increase in $\alpha/\mathrm{Re}_{ta}^{3/4}$, $\lambda_u(t)$ became smaller than λ_q in the first part of the acceleration zone and larger in the rest of the acceleration zone. On the other hand, $\lambda_u(t)$ became larger than λ_q in the first part and $\lambda_u(t)$ became smaller than λ_q in the rest of the deceleration zone. In addition, the time averaged friction factor $\lambda_{u,ta}$ was greater than λ_q and it increased with $\alpha/\mathrm{Re}_{ta}^{3/4}$. It was also concluded that pulsatile turbulent flow structure in a pipe differs widely with changing characteristic flow parameters, i.e. time averaged Reynolds number, amplitude of oscillation and the dimensionless frequency.

Ohmi, Kyomen, and Usui [31] later calculated the velocity distribution in a pulsatile incompressible turbulent pipe flow by using a time-dependent eddy viscosity ε^* to model the Reynolds stresses. They noticed that ε^* varied with friction velocity u^* when referenced to the instantaneous axial velocity profile in the pipe. They modeled time-dependent eddy viscosity as $\varepsilon^* = \varepsilon + \Delta\varepsilon$, where ε is the quasi-steady component and $\Delta\varepsilon$ the oscillatory component. The quantity $\Delta\varepsilon$ was considered to arise from the frictional velocity change corresponding to the instantaneous velocity distribution. They concluded that there was a good agreement between numerical and experimental results for the time dependent eddy viscosity in the low and medium dimensionless frequency range.

Kita, Adachi and Hirose [32] also proposed a time-dependent eddy viscosity model to analyze oscillating turbulent flows in straight pipes. The variation of ε was modeled on the basis of similarity with values of ε/u^*R in steady flow. The cross section of the pipe was divided into five layers. The predictions by this model were then compared with experiments. The comparison between calculation and measurements over a wide range of Reynolds number and frequency showed good agreement overall.

Brown, Margolis and Shah [33] applied the $\varepsilon-$distribution models of Taylor&Prandtl and Von Karman by dividing the pipe cross-section into three and four regions. They studied the response of pulsatile turbulent flows to small amplitude oscillations at acoustic frequencies between 50 Hz and 3000 Hz. At these high frequencies, the observed attenuation agreed with calculations using a time–independent viscosity profile. Based on their results, it was concluded that the flow pattern and turbulence did not have time to adjust to rapid fluctuations in velocity, and at these high frequencies, the behavior cannot be considered quasi-steady. Based on these findings they classified the

pulsatile turbulent flow into three kinds with respect to the dimensionless frequency of oscillation: low, intermediate and high frequency regions with the limit between low and intermediate frequency regions at $\alpha_q = 0.014\,\mathrm{Re}_{ta}^{0.84}$, and between intermediate and high frequency regions at $\alpha_t = 0.00025\,\mathrm{Re}_{ta}^{1.6}$.

1.3.2 Non Periodic Turbulent Unsteady Flows

A number of researchers have studied unsteady turbulent flows which are non-periodic, with particular emphasis on measurements of wall shear stress. Measurements of the unsteady wall shear stress are usually based on an indirect method. Shuy [22] carried out measurements of unsteady wall shear stress in a smooth pipe in accelerating and decelerating turbulent flows, using two different approaches simultaneously. He measured wall shear stress directly using a shear tube, and deduced it indirectly from the measured pressure gradient which is only accurate in quasi-steady flows. He concluded that in slowly varying flows, both direct and indirect measurements were generally close to their quasi-steady values. In the case of rapidly accelerating flows, the wall shear deviated increasingly from quasi-steady values as the rate of acceleration was increased and it was consistently lower than the equivalent quasi-steady value. During rapidly decelerating flows, unsteady wall shear stress was consistently higher than the quasi steady values computed from the Karman- Nikuradse equation for steady smooth pipe flow.

Lefebvre and White [23] conducted accelerating flow experiments in an unsteady flow loop facility using LDV measurements with flush mounted pressure sensors and hot film wall shear stress sensors. During the experiments, the starting Reynolds number was about 50,000 at a mean velocity of 1 m/sec. They noticed that during acceleration wall shear stress dropped by about 40% at the beginning of the acceleration but then returned

almost to its quasi-steady value. The turbulence intensity also dropped about 50 % and then returned to its quasi-steady value. They also noticed that the shape of the turbulence and wall shear stress time history curves were strikingly similar. This phenomenon was attributed to the moderate stabilizing effect of the acceleration on the entire flow field.

Jackson and He [24] conducted ramp type transient turbulent flow experiments in a pipe using water as the working fluid. They noticed that after the imposition of accelerating transients, turbulent shear stresses remain completely unchanged during the early period of the transients. They then slowly started to relax towards their quasi-steady flow values. They also observed that the response of the turbulence to imposed excursions of flow rate was characterized by three distinct time delays: a delay in response of turbulence production, a delay in turbulence energy redistribution among its three components and a delay associated with the propagation/diffusion of turbulence radially. They suggested a time scale of ν/U_τ^2 for the delay in turbulence production with its value depending on the initial flow conditions and independent of the nature of the transients. They concluded that as a result of these delays turbulence intensity is attenuated in accelerating flows and is increased in decelerating flows. The same trend was earlier observed by Gerrard [25] in which his findings revealed that the velocity profiles in pulsating turbulent flow change because of the changes in the turbulent structure of the flow i.e. acceleration reducing the turbulent intensity and deceleration increasing it.

1.4 Unsteady Transitional and Other Related Flows

There are a number of other studies that are significant to understanding unsteady flow that have some important general conclusions, discussed here. It is well known that a strong convective acceleration due to a highly favorable free stream pressure gradient has a

stabilizing effect on the steady boundary layer flow. In laminar flow, acceleration is known to delay the transition to turbulence. In turbulent flow, acceleration is believed to thicken the viscous sublayer, damp the inner layer turbulence, and, if sufficiently strong, induce a reversion toward laminar flow conditions. Research has been carried out in these areas, and is described below.

Gilbrech and Combs [34] carried out studies of unsteady pipe flow, in which they defined a Reynolds number for pulsating flow, relating it to the time average of the cross-sectional mean velocity. The critical value of the Reynolds number was interpreted as the value at which the growth rate of turbulent puffs was zero. They suggested that the critical Reynolds number in unsteady flow is a function of the ratio of the amplitude of the periodic components of velocity and the time average velocity, and also a function of the dimensionless frequency $\alpha = R(\omega/\nu)^{1/2}$. They concluded that the critical value of the Reynolds number in pulsating flow was greater than that in steady flow and that it increased with increasing amplitude of pulsation, until it reaches a maximum and decreases with increasing values of dimensionless frequency.

Lefebvere and White [35] carried out experiments to study the transition to turbulence in pipe flows started from rest with a linear increase in mean velocity. With the increase of acceleration rate, the transition Reynolds number Re_D increased monotonically from 2×10^5 to 5×10^5. They further noticed that the transition time is nearly independent of pipe diameter. They also concluded that pipe start up flow has an almost unique transition time, which is independent of spatial position for a uniform acceleration. However their results were not valid for non-constant accelerations. Leutheusser and Lan [36] carried out experiments on the start up of flow in a pipe. They showed that the transition Reynolds

number was delayed. Katako, Kawabata and Miki [37] concluded from their start up flow experiments that transition occurred only after the acceleration had greatly decreased. They also noticed that the time required for transition from laminar to turbulent flow reduced with increasing in Reynolds number.

Van der Sande [38] carried out experiments by opening a valve to generate a flow with slowly decreasing acceleration in a 5 cm diameter water pipe. He noticed that transition to turbulence occurred at a critical Reynolds number of Re_D =58000, far larger than the value of 2000 normally associated with steady transition.

Moss [39] carried out experiments in accelerating pipe flow at Reynolds number $Re_D \leq$ 20000. He did not give any correlation for transition Reynolds number but observed two different modes of transition: 1) a turbulent "slug" arising naturally in the boundary layer; and 2) a turbulent "puff" propagating downstream from the pipe inlet. Ramaprian and Tu [40] carried out LDV measurements in pulsatile oil flow in a smooth circular pipe at a mean Reynolds number of about 2100. The flow was subjected to a nominally sinusoidal flow modulation at frequencies varying from 0.05 to 1.75 Hz. They noticed that flow oscillations increased the critical Reynolds number of a puff type transitional pipe flow. They also noticed that under certain conditions, the transitional pipe flow might be laminarized by periodic pulsation.

Gerrard [25] performed experimental work based on cine photography in pulsatile flow at Re_{ta} = 3700. He observed that flow is inhibited during the acceleration part of the pulsation cycle and enhanced during the deceleration part. Hinu, Sawamoto and Takasu [41] also conducted experiments on transition to turbulence, in a purely oscillatory pipe flow. The Reynolds number was varied from 105 to 5830. They concluded that at a

Reynolds number of 5830 the flow was only partially turbulent. In that partially turbulent flow, they observed that turbulence is generated suddenly in the decelerating phase when the profile of the velocity distribution changes drastically. In the acceleration phase, the flow recovers to a laminar state.

Some more recent information on turbulent flows has come from direct numerical simulations of the Navier-Stokes equations for flows in simple geometries. Statistics from a computation of steady turbulent channel flow have been presented by Kim, Moin and Moser [48]. Although this thesis is focused on the unsteady duct flows, one steady channel flow numerical study is worth mentioning as it deals with non local momentum transfer. Sandam [49] proposed a predictive model for velocity profiles in a turbulent channel flow. In this particular case, individual terms for $\frac{\partial(u'v')}{\partial y}$ model ejection, transferring low momentum fluid away from the wall and, sweep, carrying high momentum fluid towards the wall, with a third term modeling the fluid behavior in the outer region. This model represents transfer of momentum as a non local process depending on the conditions near the wall. This model is claimed to show good agreement with experimental data for skin friction, center line velocity and shape factor.

From the above review, it is concluded that the problem of predicting unsteady wall shear or friction factors in fully developed turbulent flow is still unsolved, but of considerable importance. The above literature review indicates that, even in turbulent flows, wall shear stress or skin friction is dependent upon the history of the flow. Therefore, it may be useful to try to extend the approach proposed by Zielke and Brereton for laminar flow to turbulent flow. However turbulent weighting functions for the velocity

or pressure gradient changes would have to be developed in place of laminar ones. Due to the strong radial diffusion effects of eddies, the time history of the velocity and pressure gradient changes are much shorter for turbulent flow than for laminar flow. This might make the proposed approaches of Zielke and Brereton even more potentially useful, since it could reduce the computation time further relative to laminar flow calculations.

1.5 Motivation and Objectives of the Present Study

Today's engineering analyses of transient flows are based on quasi-steady approximations in which flow characteristics are assumed to be similar to those of steady pipe flow at the same instantaneous Reynolds number. Existing studies have shown that such an assumption is invalid particularly during decelerations or when a pulsation frequency is high. These studies do not give any viable approach for measuring the instantaneous unsteady flow rates using the fluid dynamics equations. Hence, one must use truly unsteady approaches for analyzing, measuring and inferring results for unsteady flow problems.

An exact theoretical solution (Brereton [15]) exists for the instantaneous flow rate as a function of pressure drop history, in laminar flows, but it has not been tested practically. Hence it is important to check it in controlled unsteady laminar flow experiments. This theoretical solution might potentially be extended to prediction of turbulent flows if it could be modified/tuned against turbulent unsteady-flow data. However, while there have been numerous unsteady-flow studies of transient turbulent flows, hardly any include flow rate vs pressure drop data. Therefore it is important to carry out controlled unsteady turbulent flow experiments to create benchmark data against which turbulent variations in the laminar flow-rate-to-pressure drop result can be explored.

With these motivations an experimental study was carried out to explore the applicability and limitations of these flow-rate-to-pressure drop expressions in various incompressible Newtonian fluids for laminar flows. A subsequent series of unsteady turbulent-flow experiments was then carried out to create target data, against which unsteady turbulent models for transient duct flows were then compared.

Chapter 2 Theoretical Background For Laminar Newtonian Flow

2.1 Laminar Flow Theory

Laminar flow theory is concerned with solution of the continuity and linear momentum equations together with a fluid stress to rate of strain model such as the Newtonian "Law of Viscosity". While many steady flow results relating flow rate to pressure gradient are well known, few unsteady flow results have been found. For several specific cases such as pressure varying sinusoidally, as a Heaviside unit step function or the Dirac-delta function, the velocity distribution has been calculated and relevant literature is cited in detail in Chapter 1. In this chapter, an exact solution is derived for the general case of pressure gradient varying arbitrarily with time. The same approach can be used to infer the instantaneous shear stress from instantaneous flow rate changes. These solutions relate the mean velocity to the instantaneous pressure gradient and past pressure gradient changes. This approach yields a practical approach for measuring unsteady flow rates instantaneously.

2.1.1 Navier-Stokes Equations for Fully Developed Pipe Flow, Simplifying Assumptions and Boundary Conditions.

It is convenient to use cylindrical coordinates whose x-axis is identified with the centerline of the pipe as shown in the Figure 2.1. Let r be the coordinate in the radial direction and let t denote time. The following simplifying assumptions are made:

i) The pipe contains an incompressible fluid and is rigid.

ii) The temperature variations are small enough that the fluid viscosity may be considered constant.

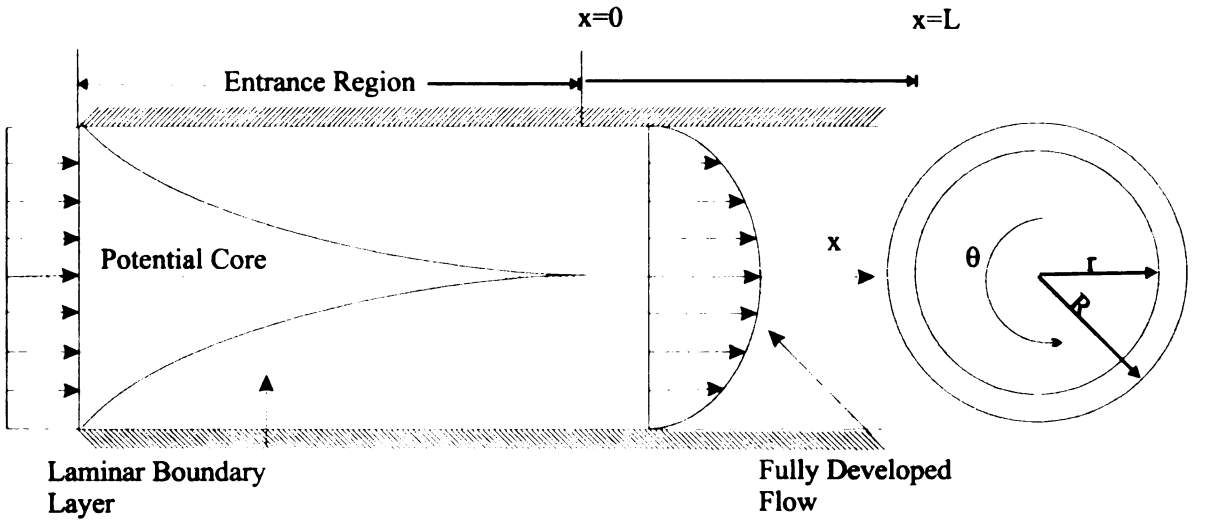

Figure 2.1: Laminar velocity profile in pipe flow

The incompressible, constant viscosity equation of motion in the x direction can be written as:

$$\rho\left(\frac{\partial v_x}{\partial t}+v_r\frac{\partial v_x}{\partial r}+\frac{v_\theta}{r}\frac{\partial v_x}{\partial \theta}+v_x\frac{\partial v_x}{\partial x}\right)=-\frac{\partial p}{\partial x}+\rho g_x+\mu\left[\frac{1}{r}\frac{\partial}{\partial r}\left(r\frac{\partial v_x}{\partial r}\right)+\frac{1}{r^2}\frac{\partial^2 v_x}{\partial \theta^2}+\frac{\partial^2 v_x}{\partial x^2}\right] \quad (2.1)$$

and the equation of motion in the r-direction as

$$\begin{aligned}&\rho\left(\frac{\partial v_r}{\partial t}+v_r\frac{\partial v_r}{\partial r}+\frac{v_\theta}{r}\frac{\partial v_r}{\partial \theta}-\frac{v_\theta}{r}+v_z\frac{\partial v_r}{\partial x}\right)\\&=-\frac{\partial p}{\partial r}+\rho g_r+\mu\left[\frac{1}{r}\frac{\partial}{\partial r}\left(r\frac{\partial v_r}{\partial r}\right)-\frac{v_r}{r^2}+\frac{1}{r^2}\frac{\partial^2 v_r}{\partial \theta^2}-\frac{2}{r^2}\frac{\partial v_\Theta}{\partial \theta}+\frac{\partial^2 v_x}{\partial x^2}\right]\end{aligned} \quad (2.2)$$

Similarly, the continuity equation in cylindrical coordinates is written as

$$\frac{1}{r}\frac{\partial(rv_r)}{\partial r}+\frac{1}{r}\frac{\partial(v_\theta)}{\partial \theta}+\frac{\partial(v_x)}{\partial x}=0 \quad (2.3)$$

The following further simplifying assumptions are made:

i) The velocity and the change of all dependent variables in the θ (circumferential) direction are negligible due to rotational symmetry i.e. $v_\theta=0$.

ii) The flow is laminar. This limits the applicability of the solution to Reynolds number of about 2100 or less.

iii) The flow is fully developed i.e. $\partial(v_x)/\partial x = 0$, so pressure is only a function of x and t.

iv) $v_r = 0$ at $r = R$ so from continuity $\partial v_r/\partial r = 0$, therefore $v_r = 0$ everywhere.

v) Equation (2.2) then reduces to the hydrostatic pressure equation $0 = -\partial p/\partial r + \rho g_r$

Therefore, for unsteady laminar, axisymmetric flows of Newtonian fluids that are fully developed in space, the continuity equation and the constant property Navier-Stokes equation for streamwise linear momentum may then be written as

$$\frac{\partial u}{\partial x} = 0 \tag{2.4}$$

$$\frac{\partial u}{\partial t} = -\frac{1}{\rho}\frac{\partial p}{\partial x} + \frac{\nu}{r}\frac{\partial}{\partial r}\left(r\frac{\partial u}{\partial r}\right) \tag{2.5}$$

where v_x is replaced by u, with the companion boundary conditions that $u = 0$ at $r = R$ and u is finite at or symmetric about $r = 0$. The most common use of these equations is for flows of Newtonians fluids of constant density and viscosity, or at least r- invariant viscosity. They are equally applicable to variable-density incompressible flows in which fluid particles maintain their density along their path so that $D\rho/Dt = 0$. The same approach can be extended to the ducts of different geometries.

2.1.2 Solution Procedure by Laplace Transformation

In transient flows it is convenient to decompose the velocity and pressure fields into the sum of their values at some initial time $t = 0$ and subsequent transient changes, i.e.

$$u(x,t) = u(x,0) + u'(x,t) \tag{2.6}$$

$$p(x,t) = p(x,0) + p'(x,t) \tag{2.7}$$

The linearity of the equation (2.5) then ensures that the initial flow field (u_0, p_0) and the transient component of change in the flow from its initial state are described by equations of the same form:

$$\frac{\partial u_0}{\partial t} = -\frac{1}{\rho}\frac{\partial p_0}{\partial x} + \frac{\nu}{r}\frac{\partial}{\partial r}\left(r\frac{\partial u_0}{\partial r}\right) \tag{2.8}$$

and

$$\frac{\partial u'}{\partial t} = -\frac{1}{\rho}\frac{\partial p'}{\partial x} + \frac{\nu}{r}\frac{\partial}{\partial r}\left(r\frac{\partial u'}{\partial r}\right) \tag{2.9}$$

with the same boundary conditions applied to u_0 and u' as to u.

Since, in fully developed flows, $\partial p/\partial x$ is only a function of t, it is convenient to re-express equation (2.5) as

$$\frac{\partial^2 u}{\partial r^2} + \frac{1}{r}\frac{\partial u}{\partial r} - \frac{1}{\nu}\frac{\partial u}{\partial t} = \frac{1}{\nu\rho}\frac{\partial p}{\partial x} = \frac{1}{\nu}F(t) \tag{2.10}$$

The linearity and constant coefficients of equation (2.10) permit Laplace transformation, which yields the transformed ordinary differential equation,

$$\frac{d^2\hat{u}}{dr^2} + \frac{1}{r}\frac{d\hat{u}}{dr} - \frac{s}{\nu}\hat{u} + \frac{u_0}{\nu} = \frac{1}{\nu}\hat{F}(s) \tag{2.11}$$

and equivalent equations for the initial and transient counterparts. In this equation, $\hat{u}$ is the one sided Laplace transform of u, $\hat{F}$ the transform of F, and $u_0(r)$ is the velocity field at

$t = 0$. The pressure gradient term $(1/\rho)\partial p/\partial x = F(t)$ is assumed continuous, or at least piecewise continuous, while s is a complex variable, the real part of which is positive. In the general theory of Laplace transforms, $F(t)$ can be at most of exponential order as $t \to \infty$, in which case there is range of values of the real part of s over which $\int_0^\infty F(t)\, e^{-st} dt$ is convergent. However since the behavior of the original function as $s \to \infty$ and $s \to 0$ is related to the character of the original function as $t \to 0$ and $t \to \infty$, respectively, and we anticipate solution to the physical problems to exist for $0 \le t < \infty$, we expect that $\int_0^\infty F(t)\, e^{-st} dt$ is convergent for all possible values of the real part of s.

The transformed boundary conditions are $\hat{u} = \hat{u}' = 0$ at $r = R$ and both $\hat{u}$ and $\hat{u}'$ are also finite at or symmetric about $r = 0$. For the case of the transient Laplace transformed velocity field $\hat{u}'(r,s)$, for which $u_0'(r) = 0$ as a consequence of equation (2.6), the ordinary differential equation (2.11), and its boundary conditions may be solved to give

$$\hat{u}'(r,s) = \frac{\hat{F}'}{s}\left(\frac{J_0\left(i\sqrt{(s/\nu)}r\right)}{J_0\left(i\sqrt{(s/\nu)}R\right)} - 1 \right) \tag{2.12}$$

where J_0 denotes the Bessel function of the first kind, of order zero. Once the Laplace transformed velocity has been found, expressions for changes in flow rate, changes in pressure gradients, and relationships between them may be found algebraically in the Laplace transformed domain, then inverse transformed back to the physical domain. Hence we can derive expressions for transient flow rates in pipes in terms of pressure gradients.

Changes in the mean velocity, and hence flow rate, in the Laplace transform domain may be found by integrating the transform of the momentary velocity field over the cross-sectional area of the duct. Using $\hat{U}'(s)$ to denote the transform of the transient part of the mean velocity $U'(t)$, we define $\hat{U}'(s)$ as

$$\hat{U}'(s) = \frac{2}{R^2} \int_0^R r\hat{u}' dr \tag{2.13}$$

Substitution of $\hat{u}'$ from equation (2.12) then leads to

$$\hat{U}'(s) = \frac{\hat{F}'}{s}\left(\frac{2}{\mathcal{J}_1\left(i\sqrt{(s/\nu)}R\right)} - 1 \right) \tag{2.14}$$

with $\mathcal{J}_1(z) = zJ_0(z)/J_1(z)$.

Unsteady pressure gradient to flow rate relationships may be formed using the expressions for changes in the flow rate, and pressure gradient, subject to a constraint on the existence of functions as Laplace transforms, and the corresponding existence of their inverse transforms. The constraint is the necessary property of Laplace transforms that the transformed functions $\hat{F}(s)$ must vanish when s tends through real values to $+\infty$ (Watson [45]).

The transformed pressure gradient term $\hat{F}'$ from (2.14) can be expressed in terms of $\hat{U}'$ as

$$\frac{1}{\rho}\frac{\partial \hat{p}}{\partial x}(s) = \hat{F}'(s) = \left(\frac{s}{\frac{2}{\mathcal{J}_1\left(i\sqrt{(s/\nu)}R\right)} - 1} \right) \hat{U}'(s) \tag{2.15}$$

or equation (2.14) can be rewritten as

$$\hat{U}'(s)=\left(\frac{\dfrac{2}{\mathcal{J}_1\left(i\sqrt{(s/\nu)}R\right)}-1}{s}\right)\hat{F}'(s) \tag{2.16}$$

so, using $\mathcal{L}^{-1}(\ )$ to denote inverse Laplace transformation,

$$U'(t)=\mathcal{L}^{-1}\left(\frac{\dfrac{2}{\mathcal{J}_1\left(i\sqrt{(s/\nu)}R\right)}-1}{s}\right)*F'(t) \tag{2.17}$$

With the symbol $*$ used to denote the convolution operation, the mean velocity is related to pressure gradient in convolution integral form as

$$U'(t)=k(t)*F'(t)=\int_0^t k(v)F'(t-v)\,dv \tag{2.18}$$

with

$$k(t)=\mathcal{L}^{-1}\left(\frac{1}{s}\left(\frac{2}{\mathcal{J}_1\left(i\sqrt{(s/\nu)}R\right)}-1\right)\right) \tag{2.19}$$

Thus the transient spatial mean velocity or flow rate can be expressed in terms of the time history of the transient pressure gradient, weighted by a convolution function that incorporates the effect of the Navier-Stokes equation and its boundary conditions. An equivalent reciprocal relationship for the transient pressure gradient as a convolution integral of the transient average velocity equation (2.15) can not be found because the response of the transient pressure gradient to unsteadiness always leads that of the velocity

field. Therefore in this unsteady wall bounded flow, one can represent mean flow as a functional of the pressure gradient, but not vice versa.

Although the transient pressure gradient cannot be expressed as a functional of transient flow rate history, it is interesting to consider how a realizable relationship for transient pressure gradient might be formed. The function given in equation (2.15) $s/\left(\left(2/J_1\left(i\sqrt{(s/\nu)}R\right)-1\right)\right)$ has no inverse Laplace transform, though it would if it were divided by s or some higher power of s. If equation (2.15) is rewritten as

$$\frac{1}{\rho}\frac{\partial p}{\partial x}(s)=\hat{F}'(s)=\left(\frac{1}{\frac{2}{J_1\left(i\sqrt{(s/\nu)}R\right)}-1}\right)s\hat{U}'(s) \tag{2.20}$$

then

$$\mathcal{L}^{-1}\left(\frac{1}{\frac{2}{J_1\left(i\sqrt{(s/\nu)}R\right)}-1}\right)$$

exists and

$$\mathcal{L}^{-1}\left[s\hat{U}'(s)\right]=\frac{dU'}{dt}+U_0'\delta(t),$$

where $\delta(\ )$ is the Dirac delta function, since the Laplace transform of the time derivative of the average velocity is $\mathcal{L}\left[\partial U/\partial t\right]=sU'(s)-U_0$. From equation (2.20) the transient pressure gradient is therefore related to the transient spatially averaged velocity (for which $U_0'=0$ in the earlier notation) as

$$F'(t) = h(t) * \frac{dU'}{dt}(t) = \int_0^t h(v) \frac{dU'}{dt}(t-v)\,dv \tag{2.21}$$

with

$$h(t) = \mathcal{L}^{-1}\left(\frac{1}{\frac{2}{\mathcal{J}_1\left(i\sqrt{(s/\nu)}R\right)} - 1} \right) \tag{2.22}$$

In this way, the transient pressure gradient is expressed as a functional of the mean flow acceleration dU/dt.

The extension of these results to form relationships involving time-integrated quantities is also straightforward. For example, the cumulative volume flow through a duct during a transient is $\int_0^t U'(t)\,dt$, multiplied by the duct area. From the Laplace transform theory,

$$\mathcal{L}\left(\int_0^t U'(v)\right) = \frac{1}{s}\mathcal{L}\{U'\} = \frac{\hat{U}'(s)}{s}$$

so dividing (2.14) by s,

$$\frac{\hat{U}'(s)}{s} = \frac{\hat{F}'}{s^2}\left(\frac{2}{\mathcal{J}_1\left(i\sqrt{(s/\nu)}R\right)} - 1 \right) \tag{2.23}$$

or, after inverse Laplace transformation,

$$\int_0^t U'(v)\,dv = K(t) * F'(t) = \int_0^t K(v) F'(t-v)\,dv$$

with

$$K(t)=\mathcal{L}^{-1}\left[\frac{1}{s^2}\left(\frac{2}{\mathcal{J}_1\left(i\sqrt{(s/\nu)}R\right)}-1\right)\right] \tag{2.24}$$

The results developed in the preceding paragraphs can be presented more completely by reintroducing absolute velocities and pressure gradients in favor of their transient components. From equation(2.12), the mean velocity to pressure gradient results for pipe flow can be derived and expressed as

$$U(t)=U(0)+\int_0^t\left(\frac{1}{\rho}\frac{\partial p}{\partial x}(t-t')-\frac{1}{\rho}\frac{\partial p}{\partial x}(0)\right)\mathcal{L}^{-1}\left[\frac{1}{s}\left(\frac{2}{\mathcal{J}_1\left(i\sqrt{s/\nu}R\right)}-1\right)\right]dt' \tag{2.25}$$

or

$$U(t)=U(0)+\int_0^t\left(\frac{1}{\rho}\frac{\partial^2 p}{\partial x\partial t}(t-t')-\frac{1}{\rho}\frac{\partial^2 p}{\partial x\partial t}(0)\right)\mathcal{L}^{-1}\left[\frac{1}{s^2}\left(\frac{2}{\mathcal{J}_1\left(i\sqrt{s/\nu}R\right)}-1\right)\right]dt' \tag{2.26}$$

We can re express equation (2.26) as

$$\int_0^t U(t)dt'=\int_0^t U(0)dt'+\int_0^t\left(\frac{1}{\rho}\frac{\partial p}{\partial x}(t-t')-\frac{1}{\rho}\frac{\partial p}{\partial x}(0)\right)\mathcal{L}^{-1}\left[\frac{1}{s^2}\left(\frac{2}{\mathcal{J}_1\left(i\sqrt{s/\nu}R\right)}-1\right)\right]dt' \tag{2.27}$$

or in terms of pressure gradient to flow rate relationship

$$\frac{1}{\rho}\frac{\partial p}{\partial x}(t)=\frac{1}{\rho}\frac{\partial p}{\partial x}(0)+\int_0^t\left(\frac{\partial U}{\partial t}(t-t')-\frac{\partial U}{\partial t}(0)\right)\mathcal{L}^{-1}\left[\frac{1}{\frac{2}{\mathcal{J}_1\left(i\sqrt{(s/\nu)}R\right)}-1}\right]dt' \tag{2.28}$$

2.1.3 Pressure Gradient to Flow Rate Results.

The pressure gradient to flow rate relationships can be related more readily to well known steady flow results if expressed as the sum of a steady state and a transient contribution. The long time or quasi-steady and transient components can be separated by splitting the inverse Laplace transform as $\mathcal{L}^{-1}[\ ]=\mathcal{L}^{-1}[\ ]_{t\to\infty}+\left(\mathcal{L}^{-1}[\ ]-\mathcal{L}^{-1}[\ ]_{t\to\infty}\right)$.

Noting that, as $t\to\infty$

$$\mathcal{L}^{-1}\left(\frac{1}{\dfrac{2}{\mathcal{J}_1\left(i\sqrt{(s/\nu)}R\right)}-1}\right)=-\frac{8\nu}{R^2} \tag{2.29}$$

We can re-express equation (2.28) as

$$\frac{1}{\rho}\frac{\partial p}{\partial x}(t)=\frac{1}{\rho}\frac{\partial p}{\partial x}(0)-\frac{8\nu}{R^2}\left(U(t)-U(0)-t\frac{dU}{dt}(0)\right)+\frac{\nu}{R^2}\int_0^t\left(\frac{dU}{dt}(t-t')-\frac{dU}{dt}(0)\right)h(t')dt' \tag{2.30}$$

and

$$h(t)=\mathcal{L}^{-1}\left(\frac{R^2/\nu}{\dfrac{2}{\mathcal{J}_1\left(i\sqrt{(s/\nu)}R\right)}-1}\right)+8 \tag{2.31}$$

When flow is steady prior to a transient, these results simplify to

$$\frac{1}{\rho}\frac{\partial p}{\partial x}(t)=-\frac{8\nu U(t)}{R^2}+\frac{\nu}{R^2}\int_0^t\frac{dU}{dt}(t-t')h(t')dt' \tag{2.32}$$

These results illustrate how the unsteady pressure gradient to flow rate expressions departs from the quasi-steady Hagen-Poiseuille relationship $-(1/\rho)\partial p/\partial x = 8\nu U/R^2$ for pipe flow. By expanding the argument of the inverse Laplace transform for large s, it can be shown that the functions tend to minus infinity as $t^{-1/2}$ as the time origin approaches zero.

2.1.4 Flow Rate to Pressure Gradient Results

The relationship reciprocal to the previous equations, i.e. expressing flow rates in terms of pressure gradient history, can now be devised. The relationships thus found would be the unsteady counterparts to the Hagen-Poiseuille one. Noting that

$$\mathcal{L}^{-1}\left[\frac{1}{s^2}\left(\frac{2}{\mathcal{J}_1\left(i\sqrt{(s/\nu)}R\right)}-1\right)\right]=-\frac{R^2}{8\nu} \tag{2.33}$$

as $t \to \infty$, equation (2.26) can be re-written as

$$\begin{aligned} U(t) = U(0) &- \frac{R^2}{8\nu}\left(\frac{1}{\rho}\frac{\partial p}{\partial x}(t) - \frac{1}{\rho}\frac{\partial p}{\partial x}(0) - t\frac{1}{\rho}\frac{\partial^2 p}{\partial x \partial t}(0)\right) \\ &+ \frac{R^2}{\nu}\int_0^t\left(\frac{1}{\rho}\frac{\partial^2 p}{\partial x \partial t}(t-t') - \frac{1}{\rho}\frac{\partial^2 p}{\partial x \partial t}(0)\right)K(t')\,dt' \end{aligned} \tag{2.34}$$

where

$$K(t)=\mathcal{L}^{-1}\left[\frac{\nu}{R^2 s^2}\left(\frac{2}{\mathcal{J}_1\left(i\sqrt{(s/\nu)}R\right)}-1\right)\right]+\frac{1}{8} \tag{2.35}$$

For the case of steady flow prior to transient, this expression simplifies to

$$U(t)=-\frac{R^2}{8\rho\nu}\frac{\partial p}{\partial x}(t)+\frac{R^2}{\nu}\int_0^t\frac{\partial^2 p}{\partial x \partial t}(t-t')K(t')\,dt' \tag{2.36}$$

These results express the departure of the unsteady mean velocity from its steady state value of $U = -\left(R^2/8\rho\nu\right)\partial p/\partial x$ for pipe flow, providing a technique to deduce the momentary flow rate from the pressure gradient history. They are entirely consistent with equation (2.25), but can be deduced more conveniently from equation (2.26). The inverse Laplace transform that determines the weighting function K is shown as a function of dimensionless time $\nu t/R^2$ in Figure 2.1.

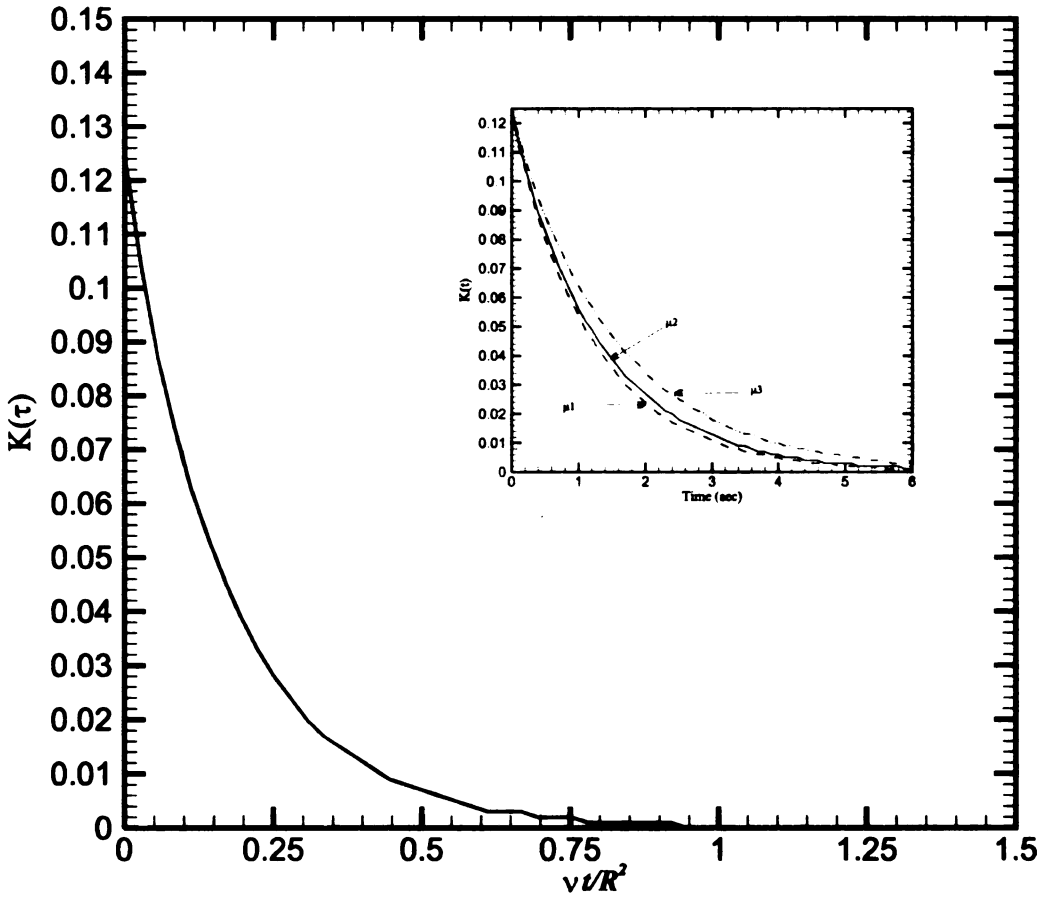

Figure 2.2: Weighting function plotted against dimensionless time; $\mu_1 = 3.34\text{E-}3$ N-sec/m^2; $\mu_2 = 2.52\text{E-}3$ N-sec/m^2; $\mu_3 = 3.09\text{E-}3$ N-sec/m^2; $\tau = \nu t/R^2$

The cumulative through flow may be found by manipulating equation (2.27) in the same way to yield

$$\int_0^t U(t)\,dt' = \int_0^t U(0)\,dt' - \frac{R^2}{8\nu}\int_0^t \left(\frac{1}{\rho}\frac{\partial p}{\partial x}(t') - \frac{1}{\rho}\frac{\partial p}{\partial x}(0)\right) dt' + \frac{R^2}{\nu}\int_0^t \left(\frac{1}{\rho}\frac{\partial p}{\partial x}(t-t') - \frac{1}{\rho}\frac{\partial p}{\partial x}(0)\right) K(t')\,dt' \tag{2.37}$$

or for an initially steady flow,

$$\int_0^t U(t)\,dt' = -\frac{R^2}{8\nu}\int_0^t \frac{1}{\rho}\frac{\partial p}{\partial x}(t')\,dt' + \frac{R^2}{\nu}\int_0^t \left(\frac{1}{\rho}\frac{\partial p}{\partial x}(t-t') - \frac{1}{\rho}\frac{\partial p}{\partial x}(0)\right) K(t')\,dt' \tag{2.38}$$

This relation also takes the form of a quasi-steady term supplemented by a term describing departure from quasi-steady behavior on account of unsteady effects, with weighting function K the same function given earlier in (2.35). The cumulative through flow in ducts in which pressure gradient became more adverse over time will exceed that anticipated using quasi-steady estimates.

In equation (2.38), the quasi-steady term, the first term on the right hand side, is supplemented by an additional integral, which describes the departure from quasi-steady behavior on account of the unsteady effects. We can re-express equation (2.38), by replacing $-\partial p/\partial x$ by $\Delta p/L$, as

$$\int_0^t U(t)\,dt' = \underbrace{\frac{R^2}{8\nu}\int_0^t \frac{1}{\rho}\frac{\Delta p}{L}(t')\,dt'}_{A} - \frac{R^2}{\nu}\int_0^t \left(\underbrace{\frac{1}{\rho}\frac{\Delta p}{L}(t-t')}_{B1} - \underbrace{\frac{1}{\rho}\frac{\Delta p}{L}(0)}_{B2}\right) K(t')\,dt' \tag{2.39}$$

In general, there are three different kinds of flow according to the relative magnitudes of terms B1 and B2 in (2.39):

$B_1=B_2$: This case corresponds to steady flow. In this case the pressure gradient remains unchanged during all times resulting in term B_1 canceling term B_2. Hence there is no unsteady correction in the accumulated mass. Equation 2.39 would then yield the same results as the Hagen-Poseuille equation $U=-\left(R^2/8\rho\nu\right)\partial p/\partial x$.

B1>B2: This case corresponds to accelerating flow since the instantaneous pressure gradient given by B_1 would be greater than the pressure gradient at the start of the transient, B_2. If used without an unsteady term, the quasi-steady term A, would overestimate the pressure gradient. This overestimation by term A is therefore compensated for in unsteady flow by a negative correction term (B_1+ B_2).

B1<B2: This case corresponds to decelerating flow since the transient pressure gradient would be smaller than that at its start. The quasi-steady term would therefore, underestimate the accumulated mass, which would then be compensated for by a positive unsteady correction term (B_1+ B_2).

The departure from the quasi-steady term at any instant can be estimated by comparing the following two terms(Brereton [15])

$$\left|\frac{1}{u(t)}\frac{du}{dt}(t)\right| \geq \frac{\nu}{R^2} \tag{2.40}$$

This expression requires that the time scale for changes in bulk velocity i.e. $u/(du/dt)$ is shorter than the viscous time scale R^2/ν. This "unsteadiness factor" therefore defines the relative importance of the unsteady effects to the quasi-steady ones. Unsteady effects can be expected to be important when

$$\frac{1}{u(t)}\frac{du}{dt}(t)\frac{R^2}{\nu} \geq 1 \tag{2.41}$$

It can be inferred from (2.41) that for a given diameter of the pipe and fluid properties, higher acceleration would give a higher unsteadiness factor. From (2.41), it can also be seen that the fluid properties play an important role in determining the size of the unsteadiness factor. For highly viscous fluids, which would reduce the viscous time scale R^2/ν, much faster transients are required to achieve appreciable unsteadiness factors.

The viscous time scale R^2/ν also plays an important role in the weighting function $K(t)$ used in (2.39). For fluids of different viscosities, the weighting function is effectively rescaled. These weighting functions, shown in Figure 2.2, decay monotonically to zero as exp (-constant t) at long times, as a consequence of the inverse Laplace transform's approximation as a single exponentially decaying term for small s, which can be shown from Cauchy's residue theorem. The weighting function always leads to positive weighting to prior values of bulk flow acceleration. It is clear that the pressure gradient generally exceeds its momentary quasi-steady value during and after the recent bulk flow acceleration. Conversely, the pressure gradient is reduced below its quasi-steady value during and after the recent bulk flow deceleration.

Zielke [11], using a similar approach calculated the wall shear stress based on the instantaneous velocity and change in velocity history. In assessing the utility of the mathematical expression (1.1), he found good agreement with the experimental results of Holmboe and Rouleau [10]. In a similar manner, the utility of the expressions for unsteady flow rates as a functional of wall-shear stress or pressure gradient derived here can be assessed by building a simple pressure gradient meter to measure the momentary mass flow rate in forced unsteady pipe flows undergoing controlled transients. It will be described in the following chapter. Since the convolution integral between pressure gradient history and

weighting functions, can, in principle, accurately predict the instantaneous flow rate in the laminar flow regime, this suggests that a laminar unsteady flow-metering device can be implemented in real world problems.

2.1.5 Extension of Fully Developed Pipe Flow Relationships to Other Geometries

Pressure pulses traveling through a tapered pipe are subject to distortions, which depend upon the geometry of the pipe and viscous shear forces. The treatment ducts of arbitrary cross-section is possible if the taper is not so great that it effects the velocity distribution. Thus the transient analyses of the previous sections can also be applied to tapered ducts when their motion can be approximated by linear forms of the Navier-Stokes equations. The one-dimensional form of the linear momentum equation (2.5) then becomes (Streeter and Wylie [46]),

$$\frac{\partial u}{\partial t}+u\frac{\partial u}{\partial x}=-\frac{1}{\rho}\frac{\partial p}{\partial x}+\frac{1}{\rho r^{n}}\frac{\partial}{\partial r}\left(\mu r^{n}\frac{\partial u}{\partial r}\right)+\frac{1}{\rho}\frac{\partial}{\partial x}\left(\mu\frac{\partial u}{\partial x}\right) \tag{2.42}$$

The parameter n is set to 0 or 1 to signify a Cartesian (channel flow with walls at $r=\pm R$) or axisymmetric (pipe flow) coordinate system. The companion continuity equation can be written as

$$\frac{\partial}{\partial t}(\rho A)+\frac{\partial}{\partial x}(\rho UA)=0 \tag{2.43}$$

where $A(x)$ is the local duct cross-sectional area and U the mean velocity. Using the simplifying assumptions of section 2.1.1, relations between pressure gradients, friction, and flow rate in one-dimensional liquid transients in tapered pipes can also be described locally by the equations (2.36) and (2.38), accompanied by the continuity equation (2.43), relating density and mean velocity changes to area changes.

Chapter 3 Experimental Apparatus

3.1 Flow Circuit Design

In order to test the applicability of expression (2.38) derived in Chapter 2, a simple pressure gradient meter was build to measure unsteady flow of liquid as a function of pressure gradient and pressure gradient history. An experiment was therefore designed in which a transient flow could be generated and measured. This facility consisted of 2.5 meters long and 9.5 millimeters diameter pipe fed by a header tank, an upstream unsteady flow-generating valve, a load cell to measure the true accumulated liquid mass and a pressure sensor to measure the instantaneous pressure gradient along the pipe as shown in Figure 3.1. The momentary pressure gradients measured by pressure sensor could then be utilized to deduce the momentary accumulated mass of the liquid from equation (2.38), which could then be compared with load cell measurements of the time dependent mass of the liquid collected. During the design process of the flow circuit design, the following aspects were considered:

i) The ability to vary flow rates without causing excessive vibrations to the apparatus.

ii) The ability to use the same apparatus for both laminar and turbulent flow regimes without any major changes.

iii) A sufficient length of the pipe to ensure fully developed flow.

iv) The pipe material and sensor should be unaffected by the choice of the liquid.

v) The pressure sensor should be sensitive enough to detect small pressure changes with high signal to noise ratio and small enough to be flush mounted with pipe walls so as not to interfere with the main flow.

vi) Data acquisition should incorporate multiple channel sampling at reasonably fast rates and with sufficient gain to enable the adequate resolution of sensor outputs.

vii) The load cell should be highly sensitive with minimum signal drift to ensure repeatability and accurate indication of the momentary mass of the liquid collected.

After careful consideration of the above points an experimental facility was designed and fabricated. Initially different experimental configurations were used in order to achieve optimal results; these configurations are listed in Appendix A. The final design of the experiment is shown in Figure 3.1. As shown in Figure 3.1, a header tank was installed on a vertical tower, which could be hoisted or lowered over a range of 3.3 meters elevations. Unsteadiness in the flow was generated by manually opening and closing a valve controlling flow from the tank to the pipe test section that housed the pressure sensor.

The experiments were conducted using a computer with a dedicated Data Acquisition and Control (DAC) card. This computer was used for energizing the pressure sensor, timing signal generation and sampling through the DAC card, and post processing of the acquired data. The pressure sensor was energized using an analog output from the DAC card. The data were acquired simultaneously from the load cell and pressure sensor. The output from pressure sensor was first amplified using an external high gain amplifier and then passed on to the DAC card for acquisition and streaming of binary data to the hard drive for later use. Similarly the voltage output from the load cell was amplified and

smoothed in a strain gauge signal conditioner before being fed to the DAC card. The software package LabVIEW was used for the sensor control, data acquisition and data post processing.

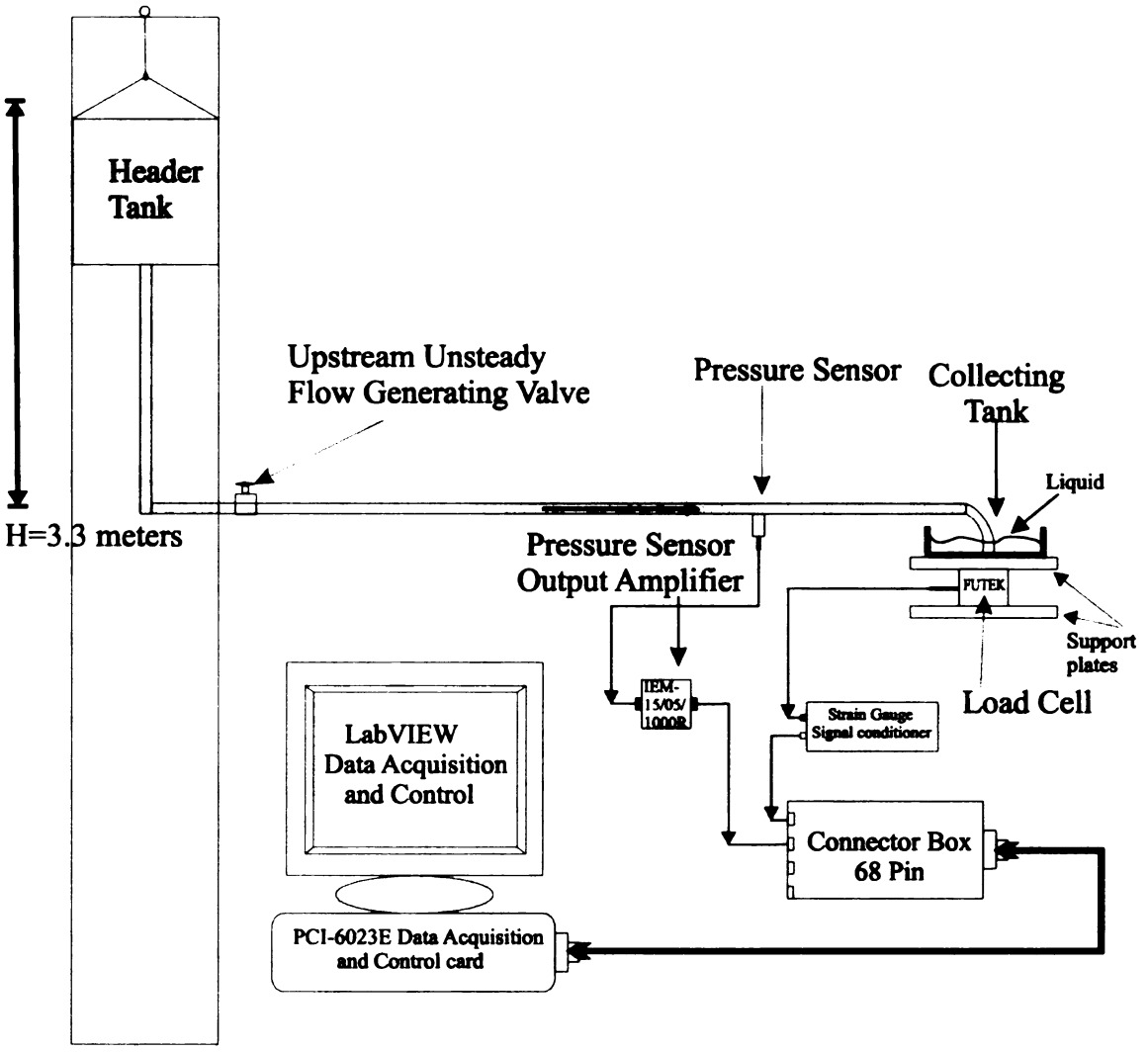

Figure 3.1: Experimental apparatus

3.2 Pressure Sensor

A pressure sensor was configured to provide a differential voltage output to the DAC card and was installed 165 diameters downstream of the unsteady flow-generating valve, at which point the flow should be fully developed. The pressure drop was measured along the pipe between the sensor location and the open end of the pipe, where

the pressure was considered to be atmospheric pressure. The pressure sensor used in these experiments was acquired from Entran Devices Inc. and is classified as an EPE "Low Pressure" sensor model EPE-541. This sensor was 2.36 mm in diameter and was designed for use in air, with a typical gauge pressure voltage output in milli-Volts. The choice of a small sensor allowed it to be almost perfectly flush-mounted in a narrow pipe, and allowed good spatial resolution in pressure measurements. The pressure sensor was coated with Paralyne-C to enable its use in water and other fluids. Due to the piezoresistive nature of this sensor, it was susceptible to zero offset, thermal zero shift and thermal sensitivity shift effects. A detailed description of the working principle of the pressure sensor, its parameters, and an explanation of the aforementioned effects are given in Appendix B. Figure 3.2 illustrate the flush mounting of the sensor in the pipe wall.

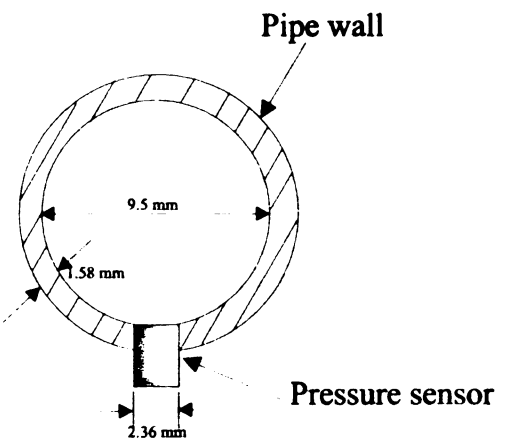

Figure 3.2: Sensor mounted in a pipe wall

In order to avoid thermal zero shift and zero offset effects, a custom data acquisition procedure was designed. To avoid zero offset, the sensor was energized for at least 30 minutes prior to data acquisition, thus giving it sufficient warm up time. The sensor was also kept in contact with the working fluid during warm up.

The highly miniaturized strain sensitive element of the EPE sensor dissipates heat when energized and the rate at which this heat is transferred is a function of the thermal conductivity of the surrounding media. The zero offset of the sensor can be related to this energy dissipation. Therefore reducing the heat generation would reduce the zero thermal drift of the sensor. The heat generated by the sensor is given by the relation $Q = \left(E^2/\mathbb{R}\right) \times t$, where Q is the heat generated in Joules, E is the excitation voltage in volts provided by the DAC card, t is time in seconds and $\mathbb{R}$ is sensor impedance in Ohms. Reduction of the excitation voltage by 50% for an input impedance of 1000 Ohms would reduce the heat generation by 75%, i.e. if the excitation voltage is reduced from 10 volts to 5 volts, it would reduce heat generation from 0.1 Joules to 0.025 Joules in 1 second. In order to reduce heat generation further, the sensor was excited for only 8% of the duty cycle using the DAC card, further reducing the heat generation by 92%. This reduction in excitation voltage resulted in a lower voltage output signal from the sensor, which was then amplified externally by using the dedicated sensor output amplifier.

3.3 Load Cells

Two types of load cells were used to measure cumulative liquid mass during the experiments: one for the small masses collected in laminar flow experiments (Interface Inc. Model SMT1-2.2) and the other for the larger masses in turbulent flow experiments (Futek model L2357). Each load cell was installed between two support plates thus enabling the liquid collecting container to be placed on top as shown in Figure 3.1. The load-measurement errors, which include loading out of plane, lateral loads, and moment loads were avoided by ensuring the alignment of top and bottom plates with each other and with the primary axis of the load cells. Care was also taken to apply the load only

along the primary axis of the load cells. The technical data and working principle of these load cells is given at Appendix C.

3.4 Viscometer

Different combinations of ethylene glycol and water solutions were used as the working fluids. Cannon-Fenske viscometers suspended in a Temp-Trol viscosity bath was

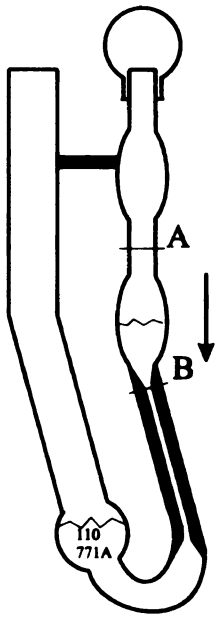

Figure 3.3: Cannon-Fenske viscometer for liquids

used to measure the viscosities of these different solutions. A range of 0.3 to 20000 centistokes could be covered with these types of viscometers. The particular viscometer used for these experiment was viscometer number 100-771A, with a calibration constant of 0.01489 centistokes/second, which required a charge of approximately 6 milliliters during the tests. After filling the charge in the viscometer, the viscometer was placed in a holder, and inserted in the constant temperature viscosity bath. Approximately ten minutes were allowed for temperature equilibrium to be reached between the viscosity bath and the test sample prior to making any viscosity measurements. Then the time was

recorded for the liquid meniscus to pass between the prescribed marks at A and B as shown in the Figure 3.3. The density of the fluid was measured using a graduated cylinder and a Sentra electronic weight scale.

3.5 Data Acquisition and Control Card

The data acquisition and control card used was a PCI-6023E, with 16 channels of analog input and eight lines of digital I/O. This card uses a DAQ-STC System Timing Controller (STC) for time related functions. The DAQ-STC enables buffered pulse generation, equivalent time sampling, and seamless changing of the sampling rate. Due to the use of a Real-Time System Integration (RTSI) bus, several measurement functions could be synchronized to a common trigger or timing event. The DAC card was configured for input of differential voltages with the Programmable Gain Instrumentation Amplifier (PGIA) as shown in Figure 3.4.

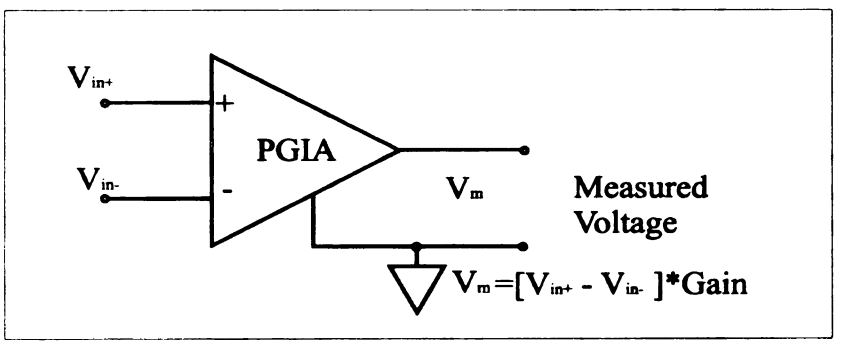

Figure 3.4: Programmable Gain Instrument Amplifier (PGIA)

3.5.1 Data Acquisition and Control

The data was acquired from two analog input channels at 10 Hz after the acquisition was triggered by one of the two counters. Acquisition timing was controlled by a hardware clock for fast and accurate sampling. Data was stored in an intermediate memory buffer after it was acquired from the analog input channels. The data from the

memory buffer was then retrieved while the acquisition was in progress, allowing the data to be processed and displayed as it was being acquired.

This data was stored in the form of a two-dimensional array; the first dimension being the scan number, the second being the channel. The buffer size was kept at 4000 samples. During the acquisition, data was saved to a binary file to minimize the storage requirement. This acquisition could be stopped either manually at any time, or after a predetermined number of scans.

For the purpose of timing sensor excitation voltages and data sampling, pulses were generated using dual synchronized continuous pulse trains as shown in Figure 3.5. The frequency was set as number of scans required per second. Duty cycle control and frequency control were used to generate the continuous pulse train from counter "0" output pin and a second pulse train of the same frequency from a second counter "1"

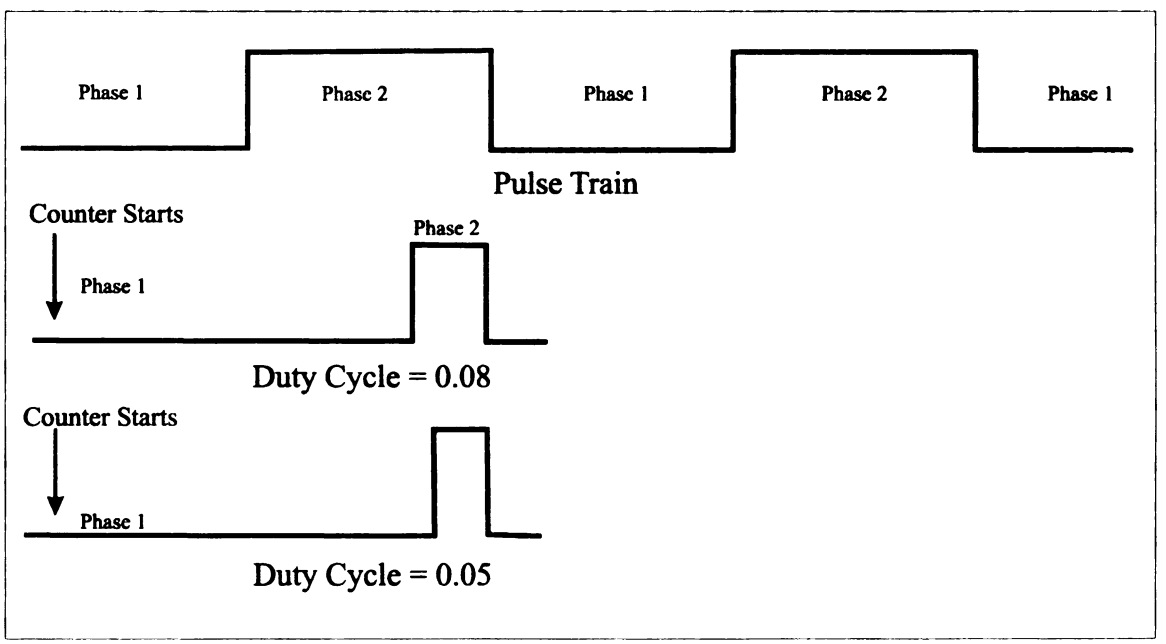

Figure 3.5: Pulse train and pulse duty cycles

output pin, on the data acquisition and control card. The second pulse train had a shorter duty cycle to ensure the excitation of the pressure sensor prior to the triggering of data acquisition. The pulse train was stopped at the same time as the acquisition. In order to avoid any thermal zero shift of the pressure sensor, the sensor was excited for only 8% of the duty cycle, and the data acquisition was carried out for 5% of the remaining duty cycle as shown in Figure 3.5.

3.6 Calibration of Sensors

The pressure sensor requirements for the experimental apparatus were that it should be small compared to the radius of the pipe, with high frequency response. The smallest suitable commercially available sensor was therefore procured. The limitations with this sensor were that it was factory calibrated for use in air and could not be used without recalibration in these experiments with liquids. In addition due to the miniature sensor design, there is no extra structural support around the sensor. Hence the sensor was highly sensitive to mounting stress. In order to overcome these limitations, the sensor was coated with Paralyne-C for use with liquids and isolated from the mounting stresses during installation with the use of low durometer RTV type materials. This necessitated its calibration in place with the working fluid to compensate for any effect of mounting stress on its output.

3.6.1 Pressure Sensor Laminar Flow Calibration

The pressure sensor in the laminar flow regime was calibrated using the following exact solution to the Navier-Stokes equations for steady, laminar, fully developed flow of Newtonian fluids:

$$\dot{m} = \frac{\pi R^4 \rho}{8 \mu L} \Delta P \tag{3.1}$$

With the maximum header tank height set to ensure laminar flow (Reynolds number < 2000), the header tank was raised at equal height increments and mass of liquid accumulated in the collecting container was recorded at each height for a fixed time interval. This procedure gave values of $\Delta P = P_s - P_{atm}$ for a range of different flow rates with the corresponding pressure sensor output recorded in milli-Volts. Here P_s and P_{atm} are

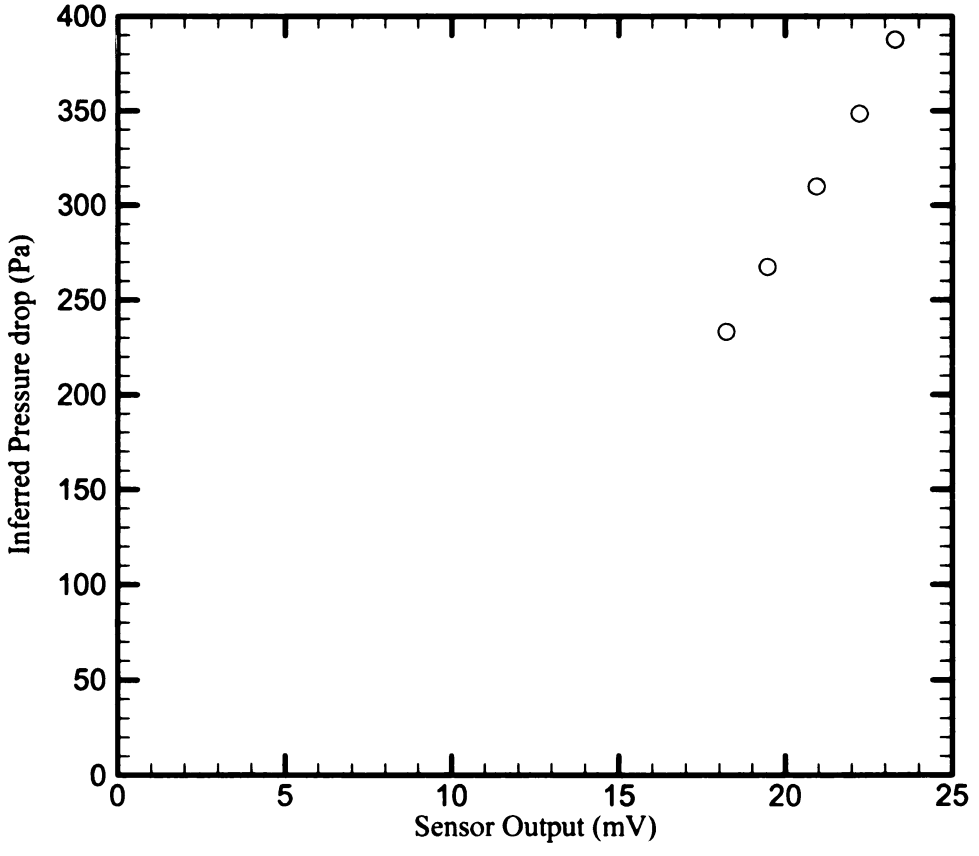

Figure 3.6: Pressure sensor calibration in the laminar flow regime with a 35/65% ethylene glycol and water mixture in a 9.5mm diameter pipe

the pressures at the sensor location and the open end of the pipe. The pressure drop values were then plotted against the values of the pressure sensor output in milli-Volts as shown in Figure 3.6, thus calibrating the pressure sensor in laminar flow regime.

3.6.2 Pressure Sensor Turbulent Flow Calibration

In order to conduct the turbulent flow experiments, the pressure sensor was recalibrated for use in the turbulent flow regime. In contrast to the laminar flow, no such

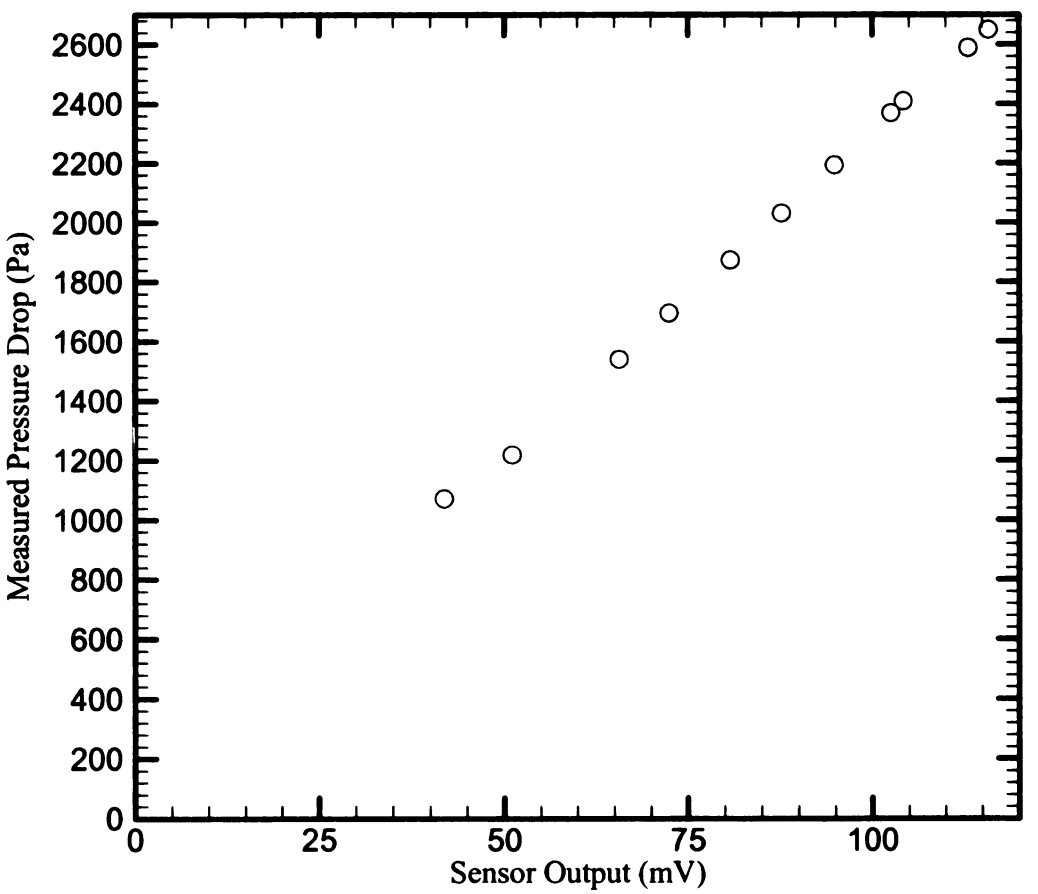

Figure 3.7: Pressure sensor turbulent calibration curve with 35/65 ethylene glycol and water solution, in a 9.5mm diameter pipe

exact relationship between pressure drop and flow rate is known which could be used for the turbulent flow calibration of this sensor. The pressure sensor calibration was therefore carried out by comparing the sensor output with pressure drop measured by manometer over a range of steady flow conditions. The pressure taps used to connect the pipe with the manometer could not be located exactly at the location of the pressure sensor due to the small diameter of the pipe and fragile nature of the sensor. In order to overcome this shortcoming, an identical test section was made to measure the pressure drop data from manometer and this data was then compared with the corresponding sensor output under the identical flow conditions. This gave a calibration for the pressure sensor in the range of pressures encountered in turbulent flow in *Pa/mV*. The resulting turbulent flow pressure sensor calibration curve is shown in Figure 3.7.

3.6.3 Low Reynolds Number Turbulent Friction Factor Relationship

During the calibration of the pressure sensor in the turbulent flow regime, data obtained from the manometer was also used to determine the friction factor in the low Reynolds number range. This served two purposes: i) it provided a comparison with the existing data on friction factors since few empirical relationships exists in the literature for the turbulent friction factor in the Reynolds number range of 2,300 to 10,000; ii) if consistent with other friction factor relationships in fully developed flows, it could indicate this one has a standard fully developed flow too. Using the relationship for friction factor and pressure drop

$$\frac{\Delta P}{\rho g} = \lambda \left(\frac{L}{D} \right) \left(\frac{U^2}{2g} \right) \tag{3.2}$$

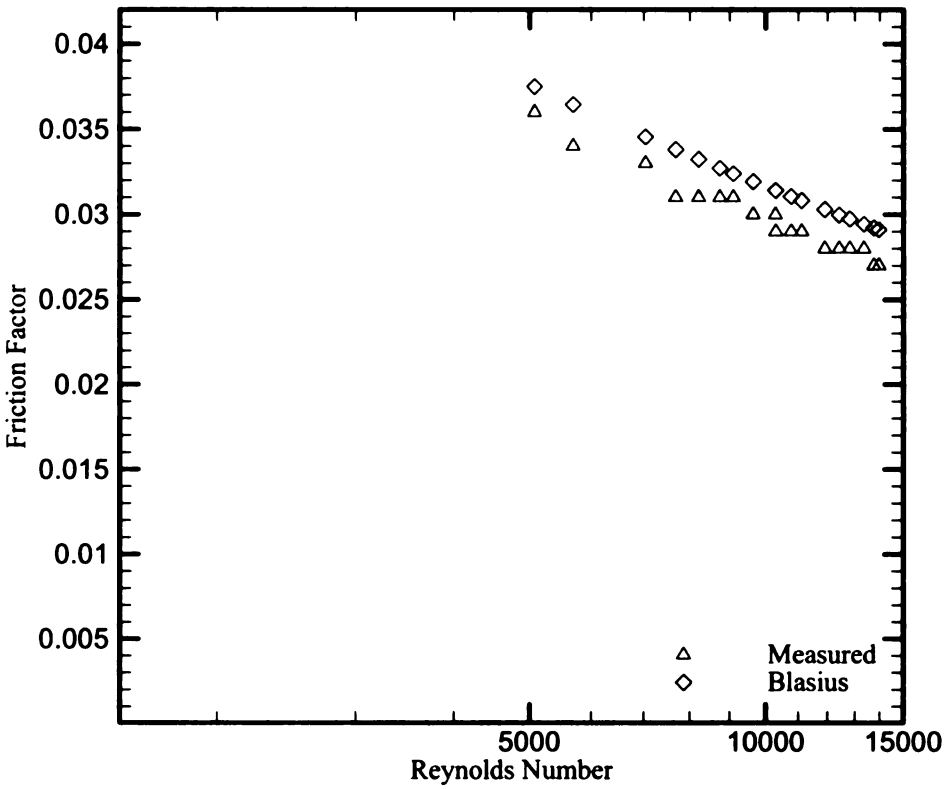

Figure 3.8: Friction factor comparison

and substituting $\Delta P = \rho g h$ and $U = \dot{m}/\rho A$, in equation (3.2) and rearranging, we find

$$\lambda = \frac{2ghd}{LU^2} \tag{3.3}$$

where λ is the friction factor, h is the change in the water column height and $\dot{m}$ is calculated from the load cell data. Different values of the friction factor for different flow rates were then plotted against the corresponding Reynolds number, which could be fitted to the empirical relationship:

$$\lambda = 0.0649 - 6\times10^{-6} Re \tag{3.4}$$

This friction factor relationship was then compared with the Blasius friction factor i.e. $\lambda = 0.3164(Re)^{-0.25}$ (White [45]). The resulting comparison is shown in Figure 3.8.

3.6.4 Load Cell Calibration

Load cell calibration was carried out by placing standard masses ranging from 5 grams to one kilogram on the load cell platform and plotting the load cell output against mass, as shown in Figure 3.9. Under the present setup, the SMT1-2.2 and Futek load cells were calibrated to give 3.2198 mV and 1.6399 mV output for one-gram change in the mass.

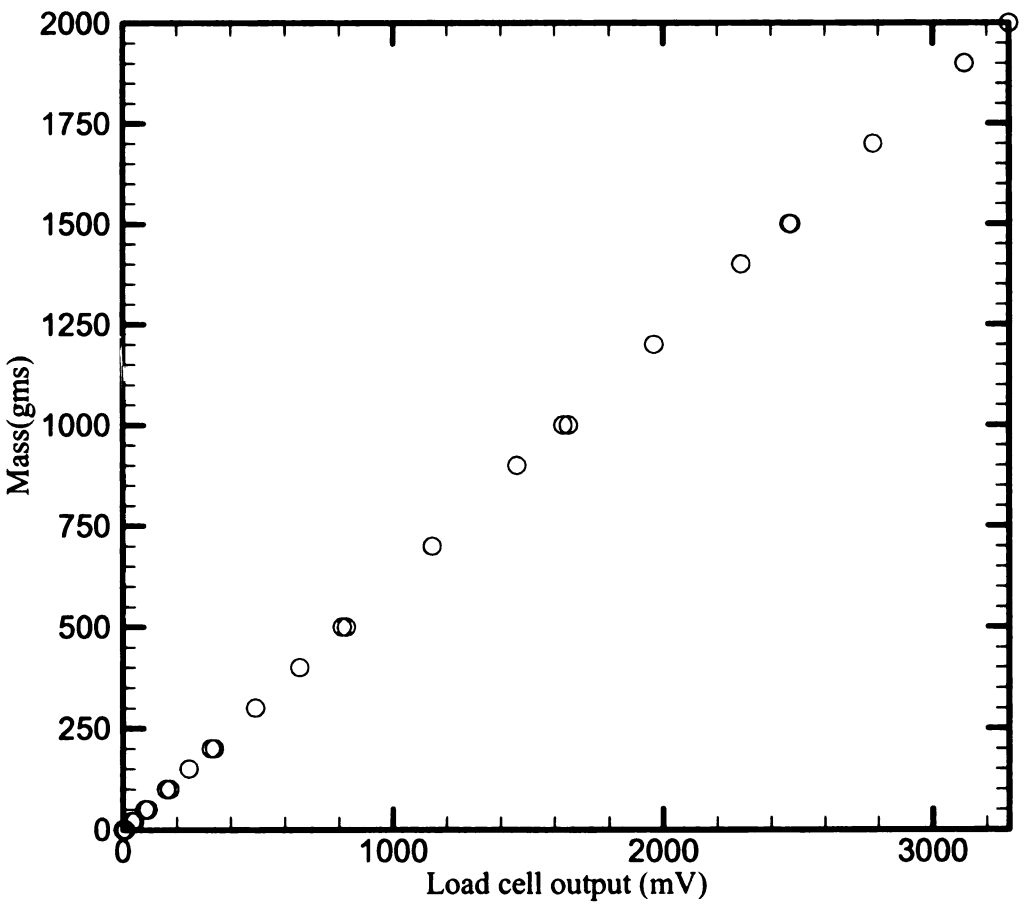

Figure 3.9: Load cell calibration curve

Since the DAC card had a resolution of 2.5 mV with no gain, a mass change of 1.0 and 1.5 grams could easily be detected using this setup.

3.7 Critical Experiment Requirements

There were two major requirements which influenced the experimental procedure and had a substantial effect on the results. These requirements were to achieve high pressure-sensor signal to noise ratios for low-pressure signals and that the pressure drops to be sufficiently high to allow accurate measurements, even at low flow rates.

3.7.1 High Signal to Noise Ratio

The low level signal from the pressure sensor was amplified using an external high performance amplifier with an adjustable gain of 1000 as shown in Figure 3.10. This amplifier had a variable gain of 10 to 1000 and the ability to adjust zero offset using a null control. The use of this amplifier allowed data acquisition at relatively low flow rates with high signal to noise ratio. The level of the input signal to the data acquisition and control card was restricted to below ± 50 mV so that a gain of 100 could also be applied

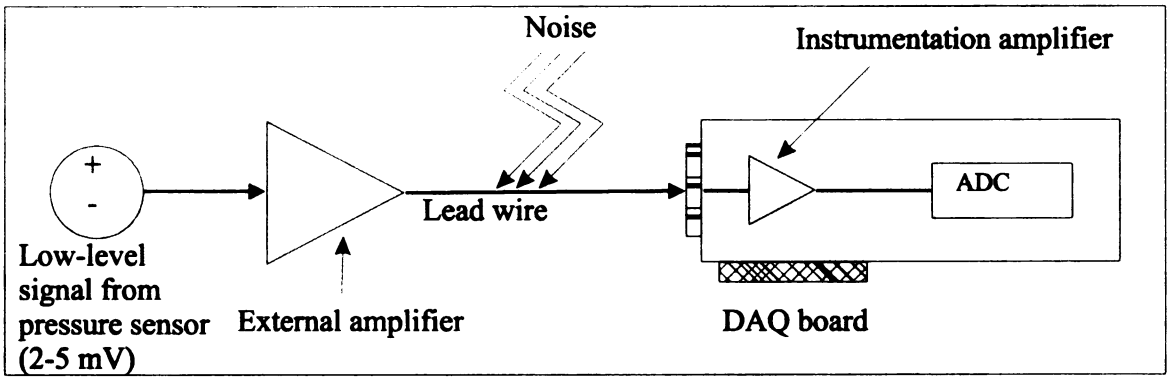

Figure 3.10: External amplifier to increase signal to noise ratio

to the incoming signal for better resolution. This not only gave the ability to detect weak signals but also increased the signal to noise ratio.

3.7.2 Working fluids

Different concentrations of ethylene glycol and water solutions were used as the working fluid. With these solutions, changes in fluid properties could be made easily by changing the relative concentration of ethylene glycol and water. In addition, a higher output signal in mV was possible on account of the higher pressure drops caused by greater viscosities of these fluids. A simple analysis was therefore carried out to estimate the dependence of pressure drop on the changes in the viscosity of the fluid. From the definition of the Reynolds number

$$Re = \frac{2\rho UR}{\mu} \tag{3.5}$$

and from the laminar mass flow rate to pressure drop relationship

$$\dot{m} = \rho \bar{U} \pi R^2 = \frac{\pi R^4 \rho}{8\mu L} \Delta p \tag{3.6}$$

$\bar{U}$ can be eliminated to yield

$$\Delta p = \frac{4L}{\rho R^3} Re\mu^2 \tag{3.7}$$

From (3.7), it is clear that for the fixed geometry and Reynolds number, pressure drop has a quadratic dependence on the viscosity of the fluid.

Initially, distilled water was used as a working fluid since it was readily available with non-corrosive properties. However, extensive drift in the pressure sensor signal was observed during the calibration of the pressure sensor. This was initially attributed to the higher thermal conductivity of the water and corresponding heat loss to the working fluid

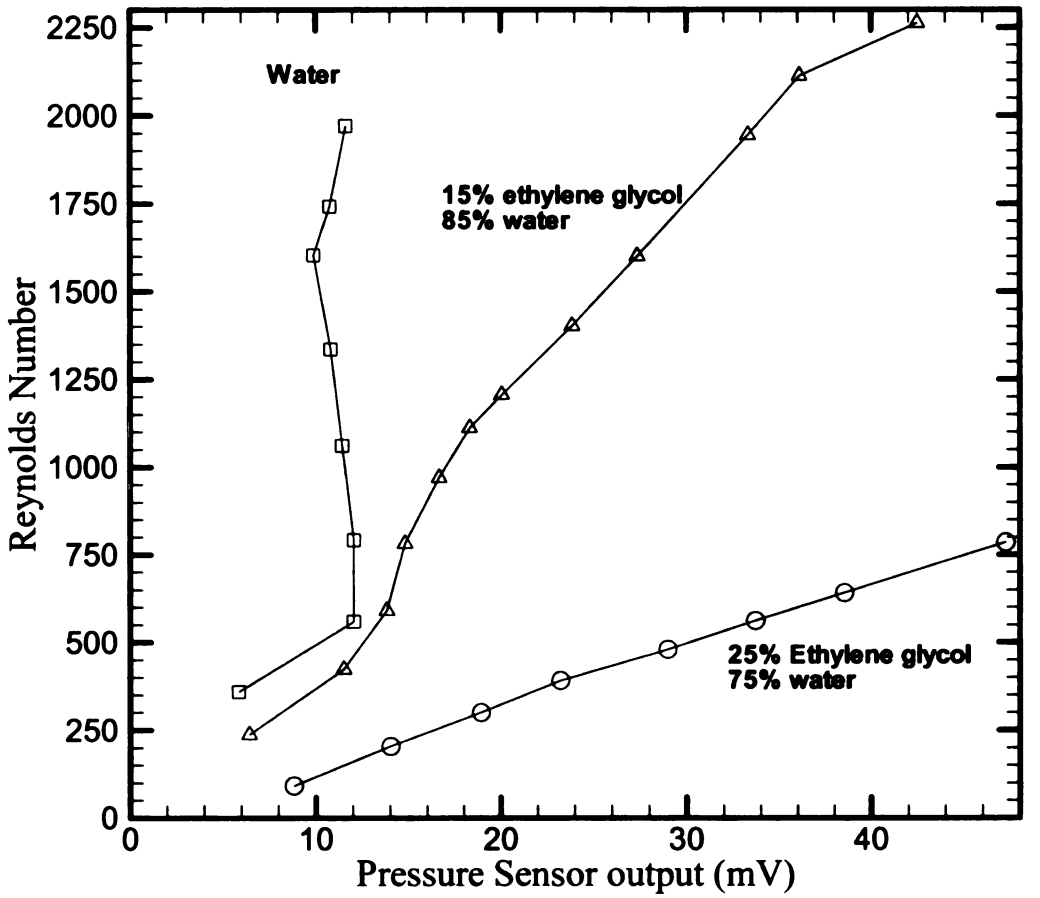

Figure 3.11: Effect of different viscosity fluids on pressure sensor output

through convective heat transfer from the sensor. Analyses were carried out to estimate the heat loss due to the temperature gradient between the sensor surface and water, which was found to be negligible as shown in Appendix D. Typical pressure sensor responses with water, and two different concentrations of ethylene glycol and water solution (μ =2.35E-3 N-sec/m^2; μ =2.52E-3 N-sec/m^2) are shown in Figure 3.11. It can be inferred that the voltage output of this sensor is linearly proportional to pressure for fluids of higher viscosity μ =2.52E-3 N-sec/m^2, but not with fluids of lower viscosity μ =

2.35E-3 N-sec/m^2 in the same Reynolds number range. The reason for this difficulty in sensing pressure in low-viscosity fluids was not fully determined. Therefore all subsequent unsteady flow experiments were carried out using ethylene glycol-water solution with viscosities greater than 2.35E-3 N-sec/m^2.

3.8 Experimental Plan

In all experimental studies of transient flows, steady flow calibrations were checked first. Once both the accumulated mass indicated by the load cell and deduced from equation (2.38) were confirmed to be in agreement in steady laminar flow, further experiments were conducted in transient flow conditions. From time to time these sensors drifted and behaved erratically and the following observations were made with regard to their performance.

i) The sensor calibration should be checked in every experiment and should first satisfy the steady flow comparison of the inferred and measured cumulative mass data, since only then would transient flow experiments yield trustworthy results. Questionable calibration curves caused by drift in the sensor indicate that the experiment should not be continued since the sensor's performance would be untrustworthy.

ii) Only pressure signals within the calibration range of the pressure sensor can be considered trustworthy. Therefore transient flow experiments must be selected carefully to fall within the calibration range.

iii) The initial value of the steady pressure gradient $\partial P(0)/\partial x$ is an important parameter in the overall comparison of the measured and inferred accumulated mass data. It should be evaluated carefully as it plays an important role in the unsteady flow-to-pressure gradient relation, as can be observed from the expression

$$\int_0^t U(t)\,dt' = -\frac{R^2}{8\nu}\int_0^t \frac{1}{\rho}\frac{\partial p}{\partial x}(t')\,dt' + \frac{R^2}{\nu}\int_0^t \left(\frac{1}{\rho}\frac{\partial p}{\partial x}(t-t') - \frac{1}{\rho}\frac{\partial p}{\partial x}(0)\right) K(t')\,dt'$$

iv) The steady flow check for calibration may be repeated more frequently to minimize the effects of pressure sensor signal drift.

3.8.1 Laminar Flow Experiments

After analyzing the behavior of the pressure sensor under steady flow conditions, the following set of experiments was carried out in the laminar flow regime:

i). Initially steady, accelerating flows, Reynolds number range 620 to 1440.

ii). Initially steady, decelerating flow, Reynolds number range 1520 to 340.

iii). Initially steady, fast accelerating ($\Delta \mathrm{Re}/\Delta t > 70/\mathrm{sec}$), slowly decelerating flows ($\Delta \mathrm{Re}/\Delta t < 70/\mathrm{sec}$), Reynolds number range 550 to 1140.

iv). Initially steady, fast decelerating ($\Delta \mathrm{Re}/\Delta t > 70/\mathrm{sec}$), slowly accelerating flows ($\Delta \mathrm{Re}/\Delta t < 70/\mathrm{sec}$), Reynolds number range 1300 to 120.

v). Initially steady, slowly accelerating ($\Delta \mathrm{Re}/\Delta t < 70/\mathrm{sec}$), fast decelerating flows ($\Delta \mathrm{Re}/\Delta t > 70/\mathrm{sec}$), Reynolds number range 1950 to 520.

vi). Initially steady, slowly decelerating ($\Delta \mathrm{Re}/\Delta t < 70/\mathrm{sec}$), fast accelerating flows ($\Delta \mathrm{Re}/\Delta t > 70/\mathrm{sec}$), Reynolds number range 500 to 1800.

A similar series of experiments were carried out in the turbulent flow regime with Reynolds number range of 3800 to 5500. In all the cases, the cumulative mass of liquid was measured together with the pressure drop along the pipe, so that theoretical

expressions relating unsteady flow rate to pressure drop could be evaluated. The results of these experiments and evaluations are given in Chapters 4 and Chapter 6.

Chapter 4 Laminar Flow Experimental Results and Discussion

4.1 Laminar Flow

A series of experiments was carried out in the laminar flow regime for both steady and unsteady flows through pipes. In steady flow experiments, data from a pressure sensor and a load cell were taken without making any changes to the flow. These steady flow experiments were then followed by unsteady flow experiments under varying flow conditions, where unsteadiness was created in the flow by manually operating an upstream valve. The working fluids were different concentrations of aqueous ethylene glycol solutions. In total, three solutions were used for laminar flow experiments to demonstrate the applicability of expression (2.38) to different incompressible fluids. The properties of these ethylene glycol solutions are tabulated below:

Properties	***Solution 1***	***Solution 2***	***Solution 3***
Density (kg/m^3)	1060	1030	1049
Kinematic viscosity (m^2/s)	3.1592 E-6	2.447 E-6	2.95 E-6
Viscous timescale (R^2/v) s	7.18	9.269	7.689

Table 4.1: Properties of ethylene glycol and water solutions

The plots shown in the following experimental results section are of the accumulated mass against time. The accumulated masses are those measured by the load cell, as well as those inferred from pressure drop measurements using (2.39). The inferred

masses are also decomposed into quasi-steady part and an unsteady correction to demonstrate the difference between various components of accumulated masses. Every fourth data point has been plotted for clarity. The quasi-steady accumulated mass data indicate the mass accumulated based only on the momentary pressure gradient along the pipe length, and is given by the term 'A' in equation (2.39). The unsteady flow correction is calculated from the convolution integral term based on the pressure gradient history and weighting function for that particular fluid (term B in equation (2.39)). The inferred or completely unsteady accumulated mass refers to the combined values of term A and B in equation (2.39) and is the sum of the quasi-steady accumulated mass and the unsteady correction.

4.2 Experimental Results

In these sections, selective results from experiments are presented which include steady, accelerating, decelerating, and accelerating-decelerating flow experiments. In all of these experiments, the flow was initially kept steady prior to inducing any transients. In the case of fluid 1, results from each type of flow are presented whereas, for fluid 2 and fluid 3, only a few representative experimental results are presented for the purposes of completeness and brevity.

4.2.1 Steady Flow Results for Fluid 1

Figure 4.1 shows the comparison of quasi-steady, unsteady correction, inferred or completely unsteady, and true cumulative mass in a steady flow experiment. In this experiment, the $\partial p/\partial x$ term remains unchanged. Therefore the cumulative mass for quasi-steady, reference and inferred terms should all indicate the same value if the load cell and pressure transducer calibration are correct and experimental noise is minimum.

Moreover the unsteady correction to accumulated mass should show no unsteady correction. The Reynolds number is based on the time average Reynolds number given by DU/v. In Figure 4.1, the time range of 0 to 8 seconds corresponds to $\frac{t}{R/u_0}$ of 0 to 665. From Figure 4.1, it is clear that these requirements are all well met.

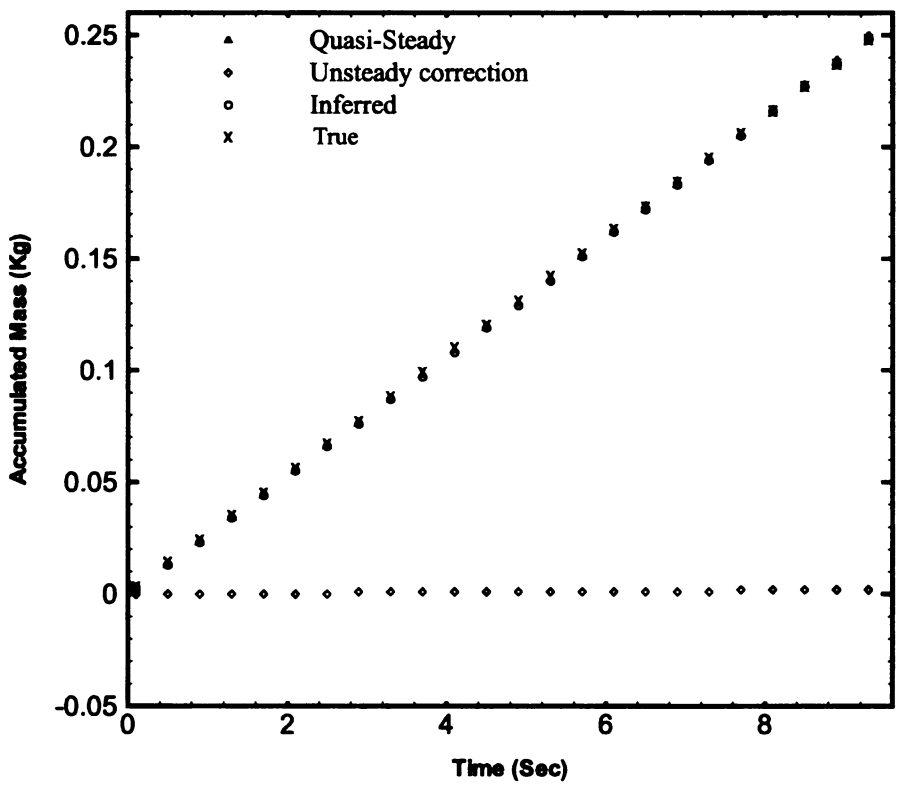

Figure 4.1: Steady laminar flow at Reynolds number 1060

4.2.2 Accelerating Flow Results for Fluid 1

Figures 4.2 and 4.3 show comparisons of quasi-steady, unsteady correction, inferred unsteady and true cumulative mass in an accelerating flow experiment. For the experiment plotted in Figure 4.2, the flow was steady for 1.5 seconds and then was

gradually accelerated. During the acceleration phase the quasi-steady value over-estimates the accumulated mass, whereas the unsteady correction counteracts this overestimation of the cumulative mass resulting in a overall good agreement between the true and inferred cumulative masses.

In Figure 4.3, the same trend is evident during a more rapidly accelerating flow, as evidenced by the greater value of the maximum unsteadiness parameter: $\gamma = \frac{1}{u(t)}\frac{du}{dt}(t)\frac{R^2}{\nu} = 6.85$.

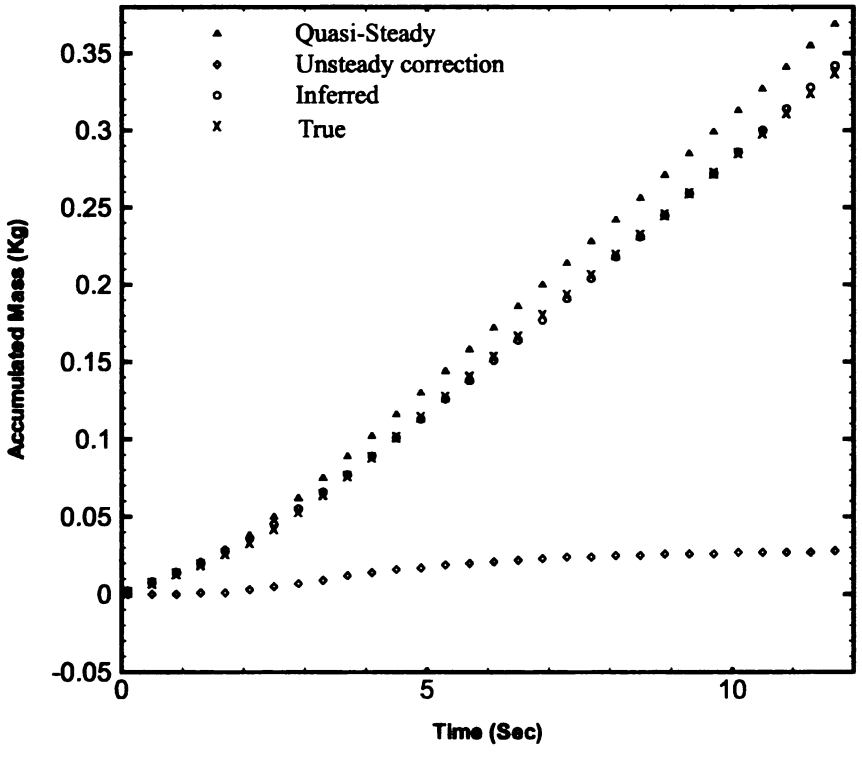

Figure 4.2: Laminar accelerating flow; Reynolds number ranging from 578 at $t = 0$ secs to 1321at $t = 12$ secs with a maximum unsteadiness factor of 1.77

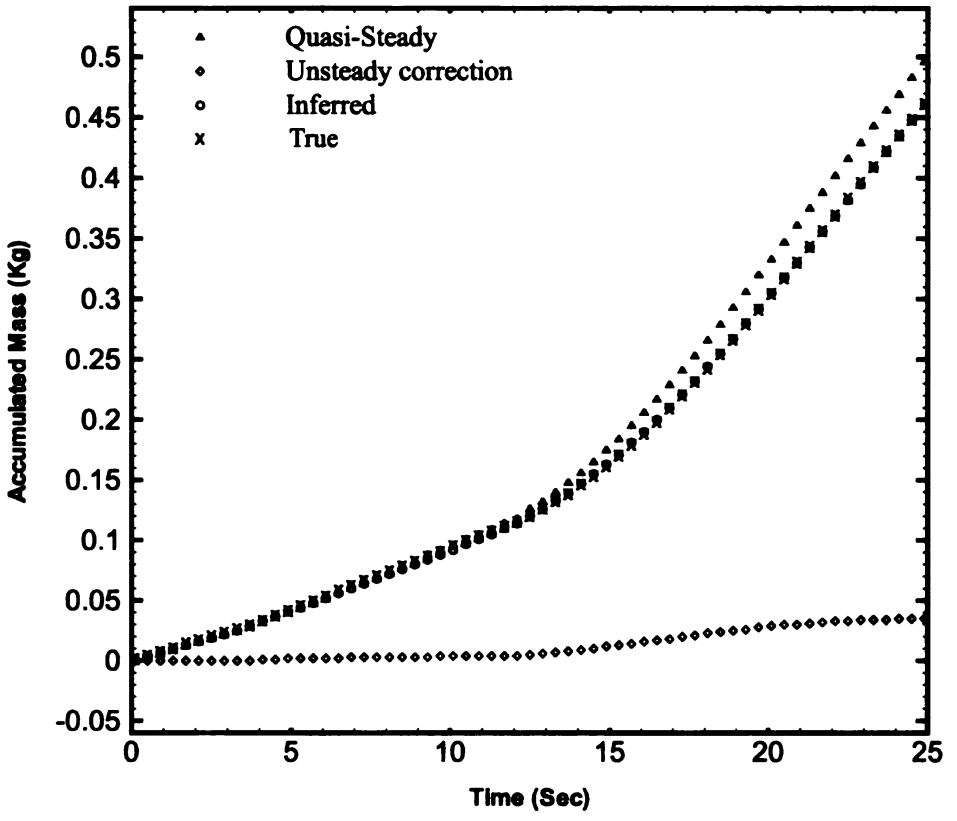

Figure 4.3: Accelerating flow: Reynolds number increases from 740 at $t = 12$ to 1517 at $t = 25$ sec; with a maximum of unsteadiness factor of 6.85

In case of the gradual acceleration, the unsteadiness factor is 1.77 (Fig 4.2), compared to 6.85 for fast acceleration (Fig 4.3). In these accelerating flows, the unsteady inferred flow equation (2.39) matches the experimental data almost perfectly.

4.2.3 Decelerating Flow Results for Fluid 1

Figure 4.4 and 4.5 show comparisons of quasi-steady, unsteady correction, unsteady and true cumulative mass in decelerating flow experiments. In Figure 4.4 the

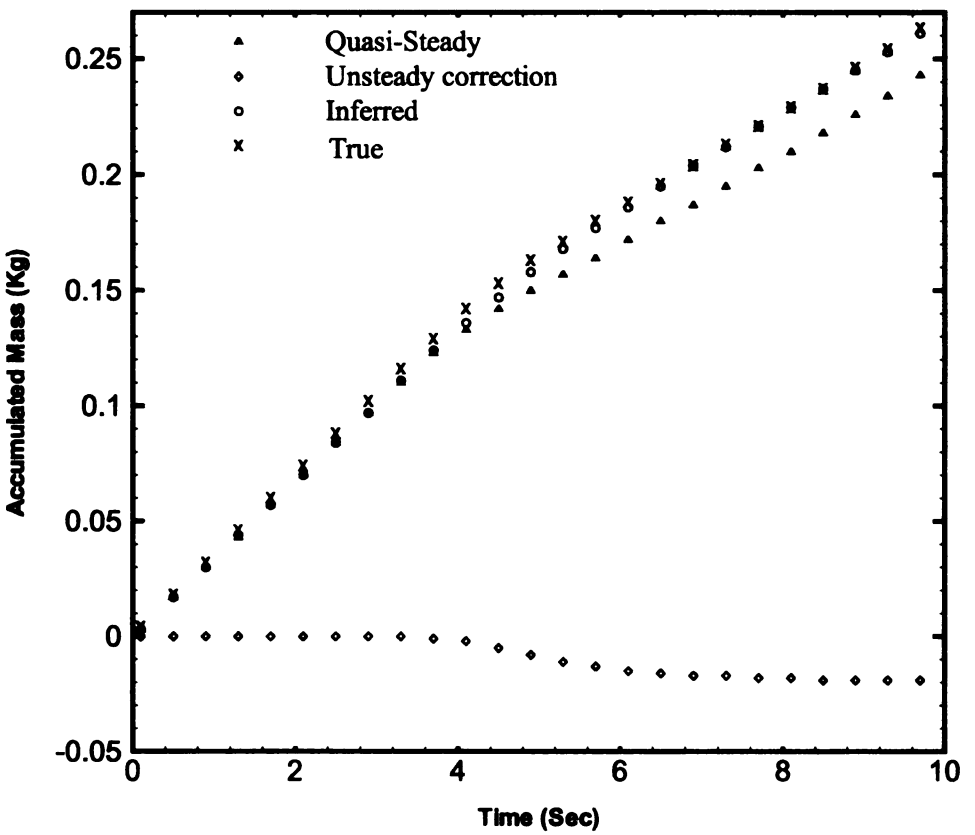

Figure 4.4: Decelerating flow; Reynolds number varies from 1405 at $t = 0$ to 1055 $t = 10$ sec ; with a maximum of unsteadiness factor of –2.07

flow was initially kept steady for 2 seconds, and then decelerated gradually. During the deceleration phase, the quasi-steady term underestimates the accumulated mass compared to the true cumulative mass. This underestimation is corrected by the unsteady correction term, which results in accurate agreement between inferred and true cumulative mass values. In figure 4.5 the deceleration phase is more adverse as is evident from the relative values of the unsteadiness factor i.e. -2.07 to -37.8. In these flows, the unsteady inferred-flow equation (2.39) also appears to be matched by experimental data very closely.

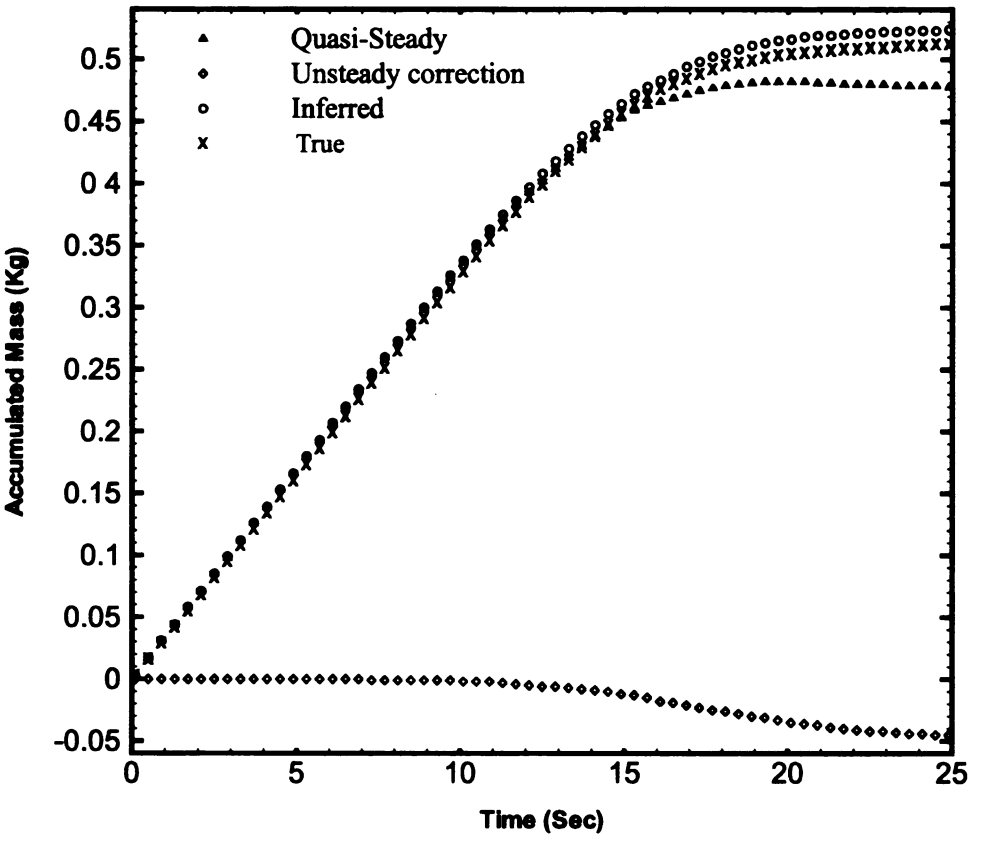

Figure 4.5: Decelerating flow; Reynolds number decreases from 1311 at $t = 13$ to 818 at $t = 25$ sec; maximum unsteadiness factor 37.8

4.2.4 Oscillating Flow Results for Fluid 1

After completion of experiments in steady, accelerating and decelerating flow cases, further experiments were conducted in combined accelerating and decelerating flows. Figure 4.6 indicates the results from one such experiment in which flow was initially kept steady for one second, and then was rapidly decelerated and accelerated.

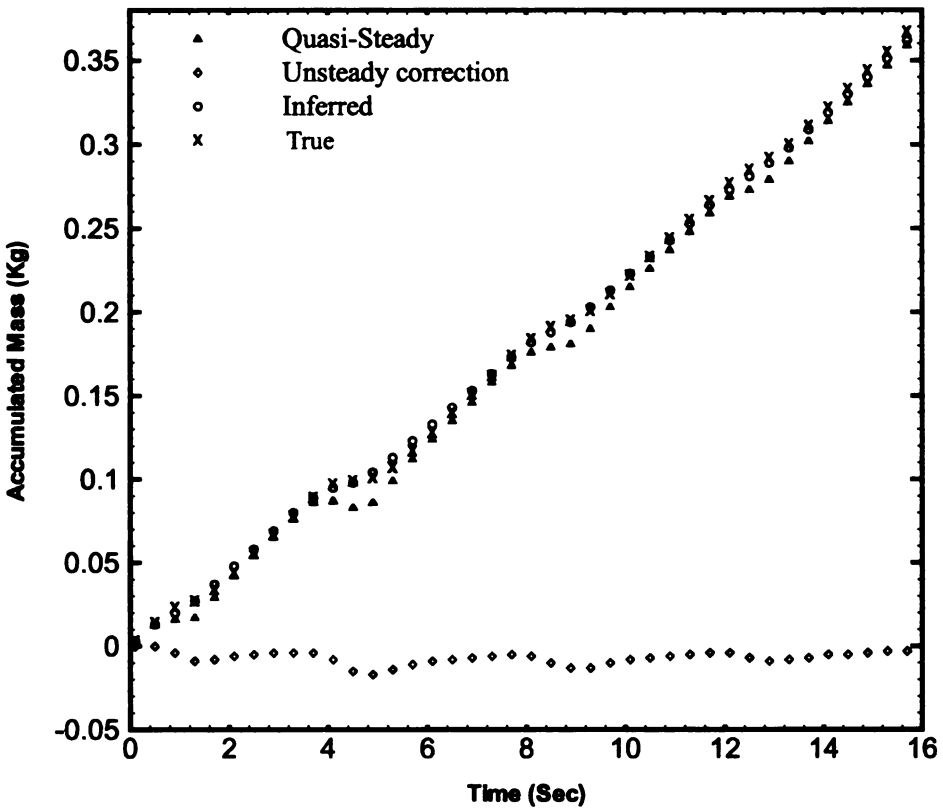

Figure 4.6: Initially steady, fast decelerating and slow accelerating laminar flow; Reynolds number 550 to 1133; maximum unsteadiness factor –58 to 40

This rapid deceleration and slow acceleration was achieved by partially opening and closing of the unsteady flow-generating valve. It is evident from the figure that the quasi-steady term underestimates accumulated mass during deceleration phases and overestimates it during acceleration phases. As the accelerations and decelerations are not of the same levels, a trend towards an overall deceleration dominated flow is observed. The levels of accelerations and decelerations were estimated as maximum unsteadiness factors of 40 and –58 respectively. Figure 4.7 also shows the comparison of accelerated

and decelerated cumulative mass for two complete cycle of oscillation. In this case, the same trend is observed i.e. quasi-steady overestimation of the accumulated mass during acceleration phase and underestimation during deceleration phase. In contrast to the above two cases, Figure 4.8, shows the comparison of quasi-steady, unsteady and true accumulated mass for accelerating and decelerating flow below the mean value of flow. In this case, the acceleration and decelerations were more severe as can be inferred by the

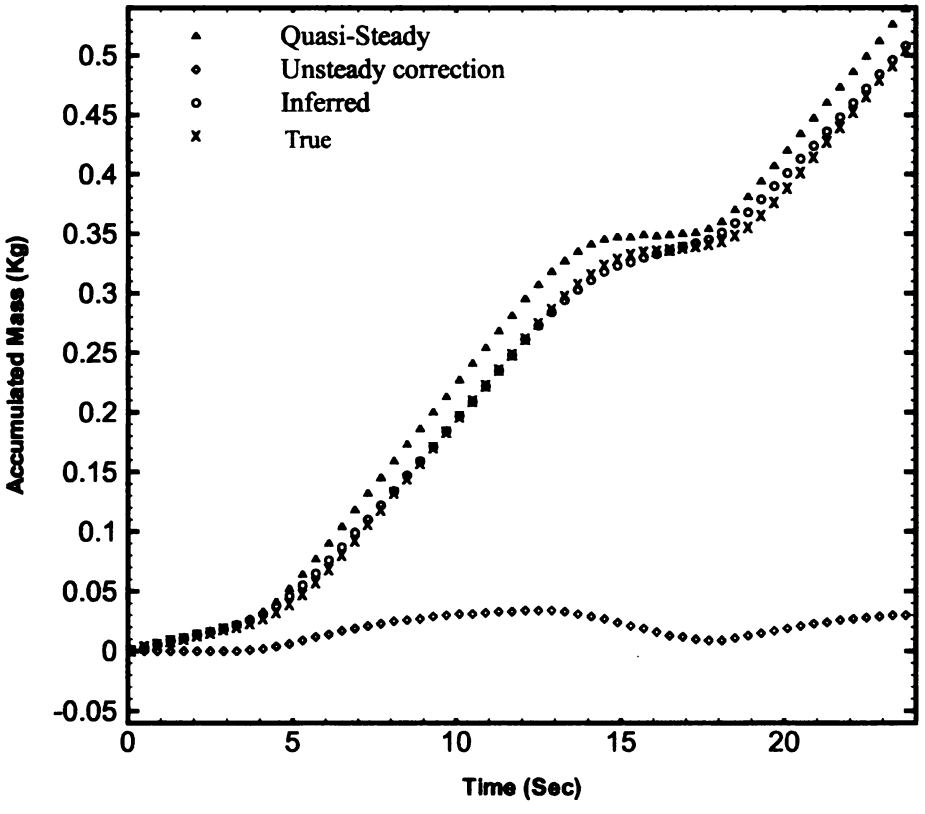

Figure 4.7: Initially steady then accelerated, decelerated rapidly above its mean value; Reynolds number 1307 at $t = 0$ to 123 at $t = 25$; unsteadiness factors range from 10.35 to – 25.7

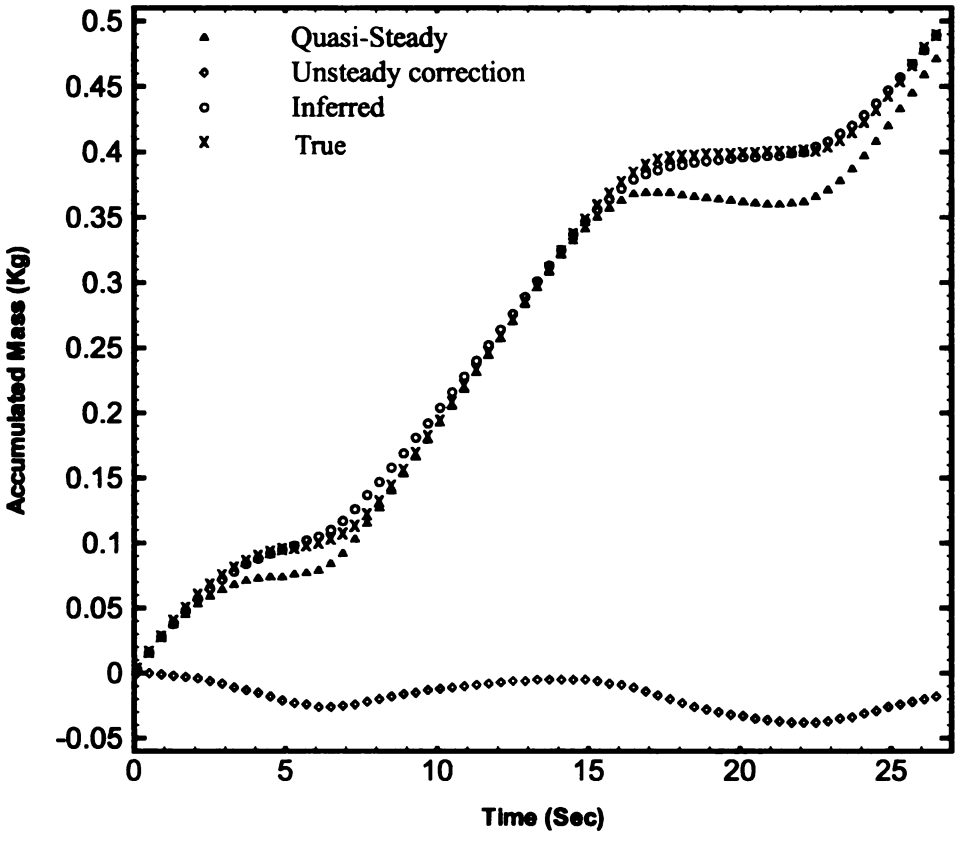

Figure 4.8: Initially steady, accelerated and decelerated flow; Reynolds number varied between 1309 to 30; unsteadiness factor varied between 86 and –88

unsteadiness factors of 86 and –88 for the acceleration and deceleration phases. Again, the agreement between the theoretical result of (2.39) and the experimental data are very good.

4.2.5 Accelerating Flow Results for Fluid 2

Figure 4.9 shows the comparison of quasi-steady, unsteady correction, inferred and true cumulative mass values in an accelerating flow experiment for a fluid of 23% lower viscosity than fluid-1. The flow is initially steady for 6 seconds and then it is accelerated. The same trend as fluid 1 is observed in this case i.e. quasi-steady

overestimation of the accumulated mass with the unsteady correction term compensating for this overestimation. There is a small discrepancy between the true and inferred accumulated mass, which is present from the start and continues to grow with time. This discrepancy is partially attributed to the less viscous fluid causing a smaller change in the sensor output, and possibly affecting the thermal zero shift of the sensor during the experiment. In this case the flow was accelerated from a Reynolds number of 1430 to 1911 with a maximum unsteadiness factor of 2.07.

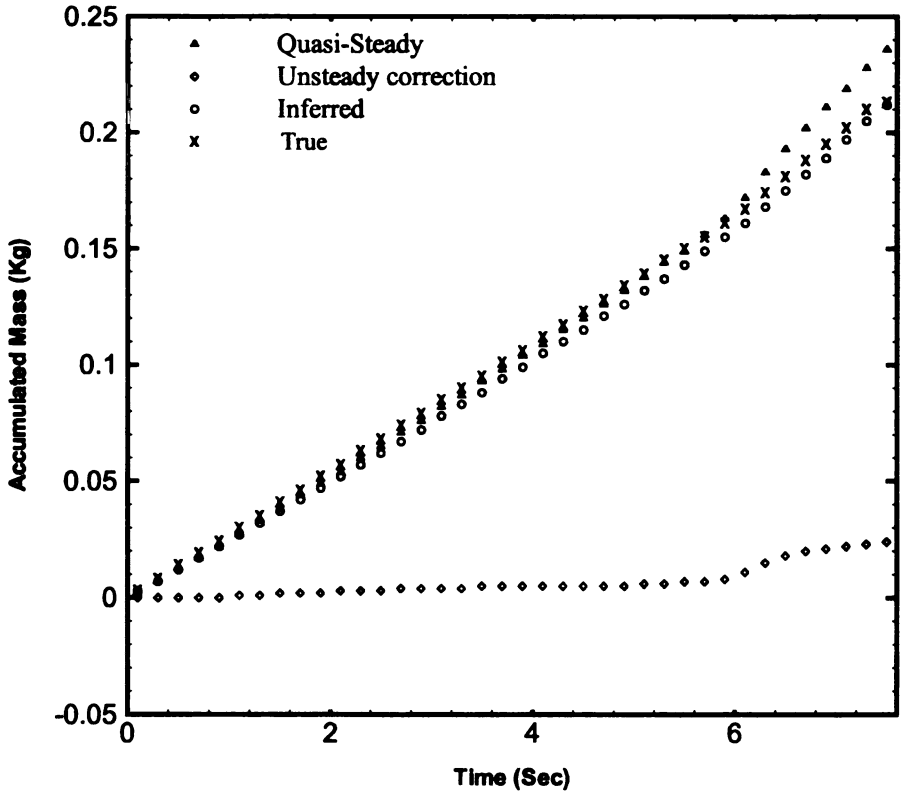

Figure 4.9: Initially steady then accelerated flow, Reynolds number changed from 1430 at $t = 2$ to 1911 at $t = 7$; maximum unsteadiness factor 2.07

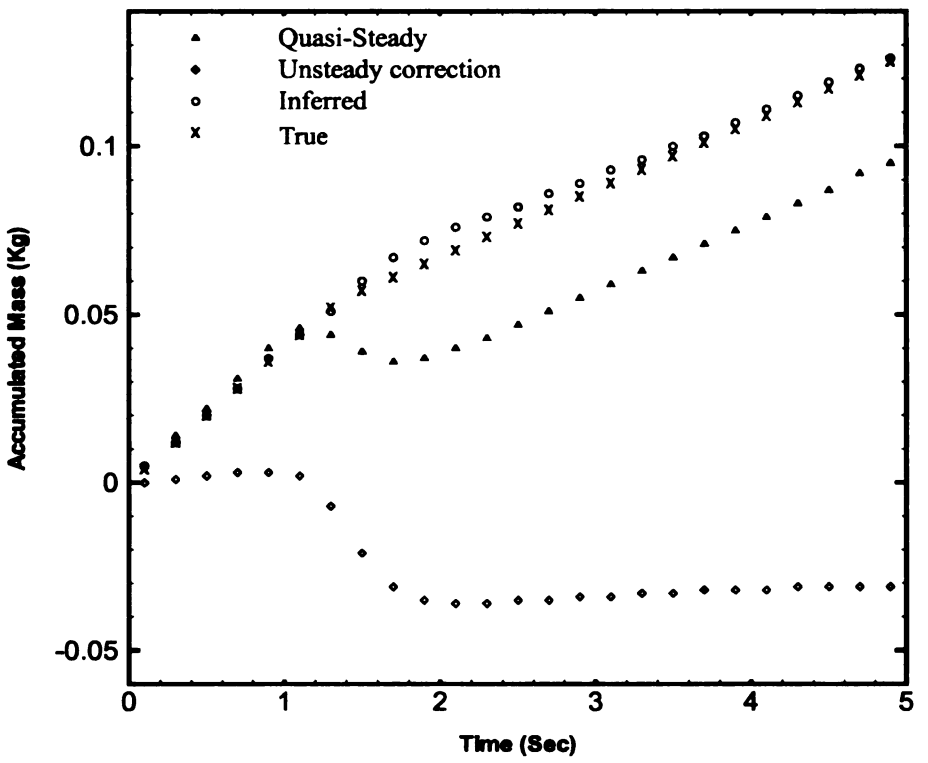

Figure 4.10: Initially steady flow then suddenly decelerated flow, Reynolds number reduced from 1900 at $t = 0$ to 500 $t = 5$, maximum unsteadiness factor –25

4.2.6 Decelerating Flow Results for Fluid 2

Figure 4.10 above shows the comparison of quasi-steady, unsteady correction, inferred and true cumulative mass during a decelerating flow experiment. Flow is initially steady for the first second and then rapidly decelerated from a Reynolds number of 1900 to 500. As shown, even in the case of such an extreme transient, the unsteadiness correction term was able to compensate and predict the correct accumulated mass. The discrepancy between the inferred and true masses is comparable to the accelerating-flow results observed with this lower-viscosity fluid.

4.2.7 Oscillating Flow Results for Fluid 2

Figure 4.11 shows the comparison of quasi-steady, unsteady correction, inferred and true cumulative mass in a decelerating/accelerating flow experiment. As expected, we see quasi-steady underestimation of the accumulated mass during deceleration phase and overestimation during acceleration phase of the flow, with the unsteadiness correction compensating for this overestimation and underestimation effects. In this case flow could be varied between Reynolds numbers of 1950 to 521 with maximum unsteadiness

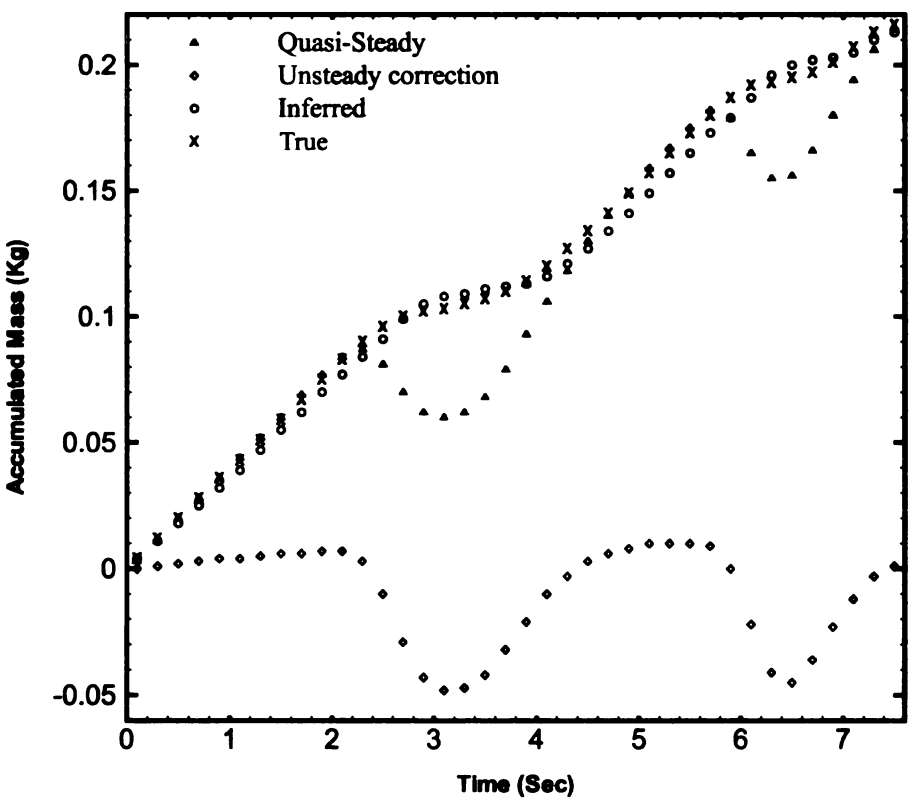

Figure 4.11: Decelerated and accelerated randomly (fluid-2); Reynolds number varied from 2050 to 521, unsteadiness factor range 15.22 to –28.18

factors of 15.22 and –28.18. The large excursions in this case are due to the fact that the fluid 2 is less viscous than the other two fluids and can be made to undergo more extreme transients in simple valve opening experiments.

4.2.8 Accelerating and Decelerating Flow Results for Fluid 3

A final series of acceleration and deceleration experiments was carried out with a third fluid with a viscosity intermediate to that of fluid 1 and 2. The acceleration flow experiment

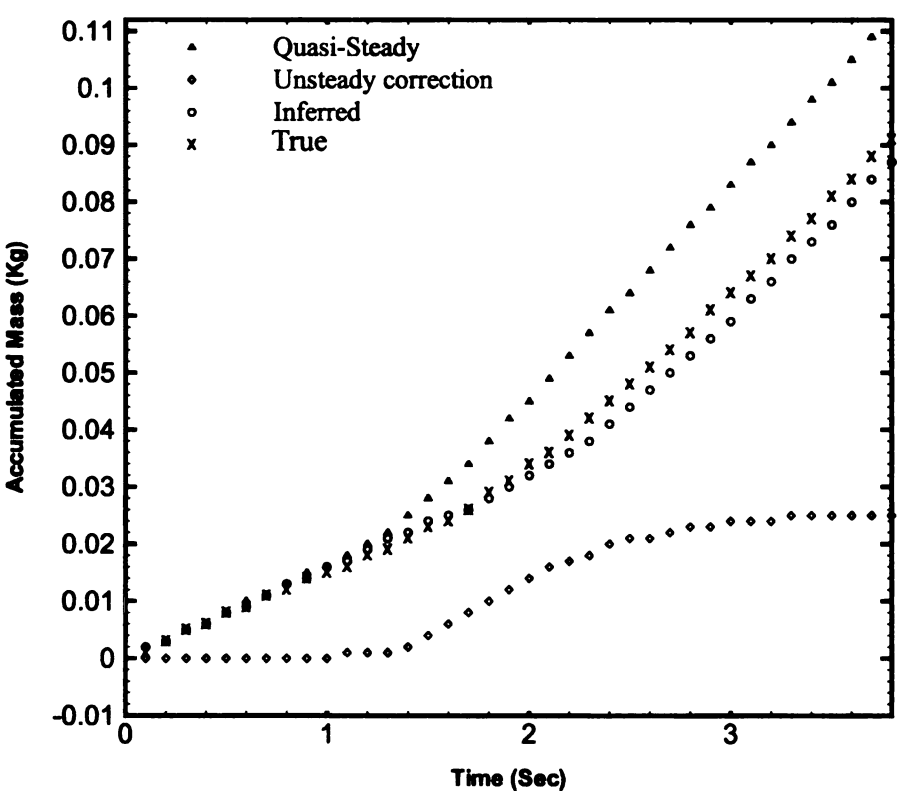

Figure 4.12: Initially steady then suddenly accelerated flow (fluid 3); Reynolds number increased from 620 at $t = 1$ to 1440 at $t = 4$; maximum unsteadiness factor 4.56

is shown in Figure 4.12 and illustrates reasonable agreement between inferred and true accumulated mass, as was found in fluids 1 and 2. The reason for larger discrepancies between the two results is not known though it is possibly attributable to sensor drift or imperfect calibration in the higher part of the pressure range. Figure 4.13 below shows the results of the corresponding decelerating flow experiment. As we might expect, the effectiveness of the unsteady correction in inferring the accumulated mass is similar to that observed in previous two cases of decelerating flow for fluid 1 and fluid 2.

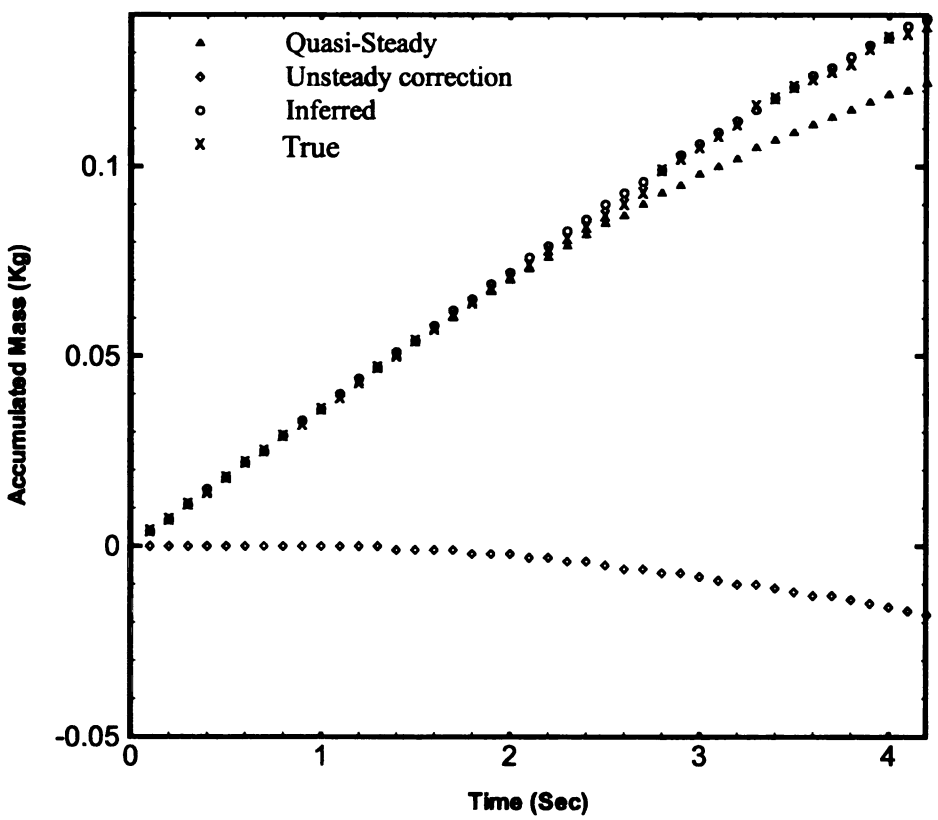

Figure 4.13: Initially steady followed by deceleration flow (fluid 3); Reynolds number reduced from 1520 at $t = 1$ to 340 at $t = 4$; minimum unsteadiness factor –3.90.

4.3 Feasibility of Unsteady Pressure Measurement for Flow Metering

The results presented in the previous section (4.2) validate the unsteady laminar flow metering theory presented earlier within experimental uncertainty. However exact matches between true accumulated mass and inferred accumulated mass can only be achieved under certain restrictive conditions as explained in section 3.8. These restrictions are partly attributed to the pressure sensor behavior. In terms of the uncertainty in the experimental data, the main sources of uncertainty are the systematic and random errors in the pressure sensor data as tabulated in Appendix E. The systematic and random uncertainties in the inferred accumulated mass are found to be 2.7% and 2.0% respectively with an overall uncertainty of about 3.4% for the steady flow results. This level is comparable to discrepancies between data and theory in the figures of this chapter. It is thought that these uncertainties could be reduced by custom design of the pressure sensor for unsteady flow metering purposes.

As mentioned in section 3.7.2, this pressure sensor responds differently to the different pressure changes experienced in different fluids, with a more linear response observed for the higher viscosity fluids. It would seem that low viscosity fluids, like pure water, would require extremely detailed, non linear calibrations over small intervals of the pressure range over which they would be used, for this kind of pressure sensor to be reliable. On the other hand, higher-viscosity fluids used over small pressure ranges might allow linear calibrations of this kind of pressure sensor.

Chapter 5 Turbulent Flow Modeling

5.1 Background

Modeling of turbulent flows poses a closure problem because of the lack of any reliable constitutive model for terms in momentum equations known as turbulent shear stresses. There have been many studies of single point closures such as $k-\varepsilon$, $k-\omega$, and $\overline{u_i'u_j'}$ models. These single point models can be complicated and hard to calibrate, and have rarely been constructed for use with unsteady problems. In unsteady flow problems these single point closure models do not account for the dynamics of the Reynolds stresses. In general, closures as complicated as systems of integro-differential equations have been proposed for accurate modeling of unsteady flows, though very few have ever been implemented or tested.

5.2 Objective

The main objective of this part of the study is to develop a predictive model for $\dot{m}(t)$ as a function of $dp/dx(t)$ for turbulent unsteady incompressible duct flows. These relationships are the counterparts to the exact laminar flow relations developed in Chapter 2. It is intended to form such relationships by seeking solutions of the Reynolds averaged equations, in forms such that the property of linearity enables the Laplace transform to be formed resulting in a convolution form of turbulent flow model, similar to the exact laminar flow relations derived earlier. As a simple first approach, a linear eddy viscosity model with a memory effect is proposed to close the unsteady momentum equation. Solutions of the resulting equations relating $\dot{m}(t)$ to $\frac{\partial p(t)}{\partial x}$ can then be formed and used

to explore the extent to which this kind of modeling can be applied to prediction of unsteady flows.

5.3 Reynolds Averaged Turbulent Momentum Equation

The Reynolds averaged turbulent momentum equation for fully-developed spatially averaged pipe flow in cylindrical coordinates can be written as

$$\frac{\partial \bar{u}}{\partial t} = -\frac{1}{\rho}\frac{\partial \bar{p}}{\partial x} + \frac{\nu}{r}\frac{\partial}{\partial r}\left(r\frac{\partial \bar{u}}{\partial r}\right) - \frac{1}{r}\frac{\partial}{\partial r}\left(r\overline{u'v'}\right) \tag{5.1}$$

Equation (5.1) is similar to its counterpart in laminar flow equation (2.5), with an additional term $\frac{1}{r}\frac{\partial}{\partial r}\left(r\overline{u'v'}\right)$, where $\overline{u'v'}$ is defined as the apparent turbulent shear stress. In unsteady flows, the Reynolds averaging is carried out over multiple repetitions of the same event, at the same phase. This turbulent shear stress is often negatively correlated with $\frac{\partial \bar{u}}{\partial r}$ in shear flows. The problem of modeling it accurately in terms of $\bar{u}$ and other variables is called the closure problem. This turbulent stress can, in general, be predicted only with a detailed knowledge of the turbulent structure and is related to the local flow conditions such as velocity, geometry, surface roughness and upstream history.

For the purpose of this thesis, turbulent shear stress needs to be modeled to predict both steady and unsteady flow through ducts. We denote u_0, p_0, $u'v'_0$ as the fluid quantities representing mean velocity, pressure and turbulent shear stress at some initial time. If we substitute these initial values into equation (5.1) and subtract it from the general, time-dependent form of equation (5.1), we can write the transient part of the equation (5.1) as

$$\frac{\partial(\bar{u}-\bar{u}_0)}{\partial t}=-\frac{1}{\rho}\frac{\partial(\bar{p}-\bar{p}_0)}{\partial x}+\frac{\nu}{r}\left(r\frac{\partial(\bar{u}-\bar{u}_0)}{\partial r}\right)-\frac{1}{r}\frac{\partial}{\partial r}\left(r\left(\overline{u'v'}-\overline{u'v'}_0\right)\right) \tag{5.2}$$

Setting $\tilde{u}=\bar{u}-\bar{u}_0$, $\tilde{p}=\bar{p}-\bar{p}_0$ and $\widetilde{u'v'}=\overline{u'v'}-\overline{u'v'}_0$ as the transient components of u, p and $u'v'$, we have

$$\frac{\partial\tilde{u}}{\partial t}=-\frac{1}{\rho}\frac{\partial\tilde{p}}{\partial x}+\frac{\nu}{r}\frac{\partial}{\partial r}\left(r\frac{\partial\tilde{u}}{\partial r}\right)-\frac{1}{r}\frac{\partial}{\partial r}\left(r\widetilde{u'v'}\right) \tag{5.3}$$

which is the streamwise momentum equation for the transient part of the fully developed pipe flow.

5.4 Turbulent Shear Stress Model

The modeling approach we attempt is based on a simple algebraic model of eddy viscosity accounting for the flow transients through a memory effect. Turbulent shear stress is usually modeled in terms of eddy viscosity as

$$-\overline{u'v'}=\nu_t\frac{\partial\bar{u}}{\partial r} \tag{5.4}$$

because $-\overline{u'v'}$ is generally correlated with $\partial\bar{u}/\partial r$ in experiments on steady flow. To incorporate the effect of memory in a $-\overline{u'v'}$ to $\partial\bar{u}/\partial r$ relation, we model $-\overline{u'v'}$ as $W(t)$ convolved with $\frac{\partial^2\bar{u}}{\partial r\partial t}$ or

$$-\overline{u'v'}=W(t)*\frac{\partial^2\bar{u}}{\partial r\partial t} \tag{5.5}$$

Setting $W(t)=\nu_t,\nu_t=\nu_t(y)$; recovers the relation: $-\overline{u'v'}=\nu_t\,\partial\bar{u}/\partial r$ in steady flow, and setting *W(t)* to some function of time allows an effect of memory to be introduced in a

simple way. Since we expect the effect of changes in the shear, $\partial\overline{u}/\partial r$, to lead to a delayed change in the turbulence as observed by Jackson and He [24], we might expect *W(t)* to be a function sketched like

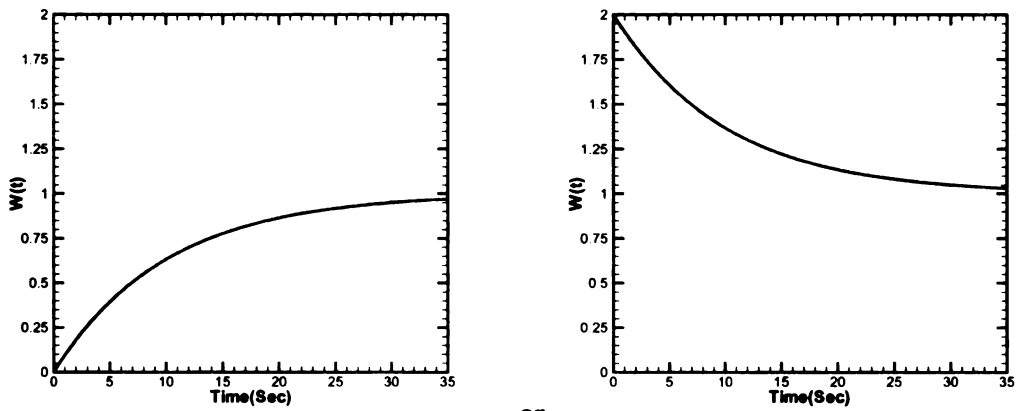

or

Figure 5.1: Expected forms of weighting functions in turbulent flow

It is convenient to model the adjustment of *W(t)* to its long time value, or $W(t)-W(\infty)$ as scaling on $e^{-t/T}$, where T is a turbulent timescale like $\frac{R}{u_\tau}$ or $\frac{R}{u_{CL}}$. The long time value of *W(t)* after effects of a transient have died out should be the steady state value of ν_t consistent with the equilibrium basis for eddy viscosity theories. Therefore *W(t)* is modeled as the sum of an immediate or quasi-steady part and a delayed response, as $W(t)=a\left[H(t)+\alpha e^{-\beta t}\right]$. In this case, the transient part of the turbulent shear stress is modeled as

$$-\widetilde{u'v'}=\left[H(t)+\alpha e^{-\beta t}\right]a*\frac{\partial^2\tilde{u}}{\partial r\partial t} \tag{5.6}$$

where a has the units of eddy viscosity, and H is the Heaviside step function, and ~ denotes the transient component. Equation (5.6) can be expressed as the changes in $-\overline{u'v'}$ from some initial value as

$$-\overline{u'v'}(t)-\left(-\overline{u'v'}(0)\right)=aH(t)\left(\frac{\partial\overline{u}(t)}{\partial r}-\frac{\partial\overline{u}(0)}{\partial r}\right)+a\alpha e^{-\beta t}*\left(\frac{\partial^2\overline{u}(t)}{\partial r\partial t}-\frac{\partial^2\overline{u}(0)}{\partial r\partial t}\right) \tag{5.7}$$

The first part of the RHS of the equation (5.7) represents an instantaneous or quasi steady response of the turbulence, whereas the second part represents a time delayed or history response to the turbulence. The relative initial magnitude of the overall turbulence response depends on the values of the parameter α and a, with parameter β controlling the rate at which transients in shear stress reach a steady state value. For any initial time $t=0$, the value of α would signify the quasi-steady change in the $-\overline{u'v'}$ for any change in $\partial\overline{u}/\partial r$. Depending on the values of α and β, there can be an immediate or delayed response of turbulent shear stress which would only approach to its steady state value at long times. The contribution of α is to determine the immediate offset in the initial steady turbulent shear value, whereas β determines how fast this offset relaxes to its steady state value. The higher the value of β, the faster it would approach the steady state value.

5.5 Calibration of the Model Parameters a, β and α

5.5.1 Calibration of *a*

The parameter a has the units of kinematic viscosity and, because, for simplicity, it is set to a single value for all r-values, it represents the average value of the apparent

eddy viscosity across the duct. Its value is chosen such that it provides a match with steady flow rate to pressure drop data in ducts. In equation (5.7) a can be expressed in terms of Laplace-transformed variables as

$$a = \frac{\nu_t}{\mathcal{L}^{-1}\left[\hat{w}(s)\right]_{t\to\infty}} \tag{5.8}$$

where $\widehat{W}(s) = \mathcal{L}\{W(t)\} = \mathcal{L}\{H(t) + \alpha e^{-\beta t}\} = 1/s + (\alpha/s + \beta)$. For flows at different initial Reynolds numbers, it is expected that a might change, just as ν_t does in measurements made in steady flows. ν_t (apparent eddy viscosity) is then modeled as

$$\frac{\nu_t}{\nu} = \kappa Re_\tau \tag{5.9}$$

where κ is a calibration constant dependent upon the Reynolds number. Arpaci and Larsen [42] have found a similar expression for turbulent flow through tubes at Reynolds number of as high as 50,000, as $\nu_t/\nu = Re_\tau/15$, where $Re_\tau = u_\tau R/\nu$. Here u_τ is the friction velocity of the flow and is defined as $\sqrt{\tau_w/\rho}$ and R is the radius of the pipe. It follows that setting κ to 1/15 times the molecular kinematic viscosity allows a to be calibrated as $a = \dfrac{Re_t}{\mathcal{L}^{-1}\left[\dfrac{1}{s} + \dfrac{\alpha}{s} + \beta\right]}$.

5.5.2 Calibration of β

The parameter β is a time constant which causes the delay as the instantaneous shear stress relaxes to its steady state shear stress value. This is chosen to scale on the characteristic velocity and characteristic length scale of the flow, i.e. u_τ/R or

$u_0(t)/R$, based on dimensional reasoning. Its value, as a multiple of u_τ/R or $u(t)/R$, must be found empirically from transient flow experiments.

5.5.3 Calibration of α

The parameter α determines the magnitude of the unsteadiness response of the turbulent shear stress to the changes in $\frac{\partial u}{\partial r}$, as a part of the memory effect. Prior to assessing model performance against experimental data, it is not clear if α may be calibrated as a constant along with the value of a depending on the initial flow conditions or if it must be represented as a measure of turbulence response to imposed transients time scale such as $\alpha = \left(u_\tau/(dU_{CL}/dt)\right)(u_\tau/R)$. This calibration must also be carried out empirically, using data from unsteady flow experiments.

In order to check the reasonableness of the proposed shear stress model in equation (5.7), the model was compared with the ramp up transient experimental data of Jackson and He [24]. The parameters of equation (5.7) were calculated from the experimental data as $a = 4.5$ α was taken as -8, since this value seems to give a comparable delay in the response to shear transients of $u'v'$ as can be seen from Figure 5.1. This value was used subsequently to test the model against the experimental data of this study. Parameter $\beta = \frac{u_\tau}{R}$ was calculated from the initial flow conditions of Jackson and He [24]. Two data series were selected from their experimental data to indicate the variation of Reynolds shear stresses at $y = 1.9\,\text{mm}$ ($y^+ = 17.1$) and $y = 12\,\text{mm}$ ($y^+ = 120$) in a 50.4 mm diameter pipe during a ramp up transient in flow rate. These data series for measured values of $-u'v'(t) - \left(-u'v'(0)\right)$ are plotted in Figure 5.1 for the first 5 seconds

of this constant acceleration experiment together with the model prediction for the *span-averaged* value of $-u'v'(t)$ (5.7). The shear stress model of (5.7) shows a reasonable agreement with the experimental data insofar as it represents an average eddy viscosity behavior across the pipe quite well. It is evident from the Figure 5.1 that 'average' $u'v'$ predicted by the model shows the same order of magnitude and history as that of the experimental data of Jackson and He [24] for a ramp up acceleration.

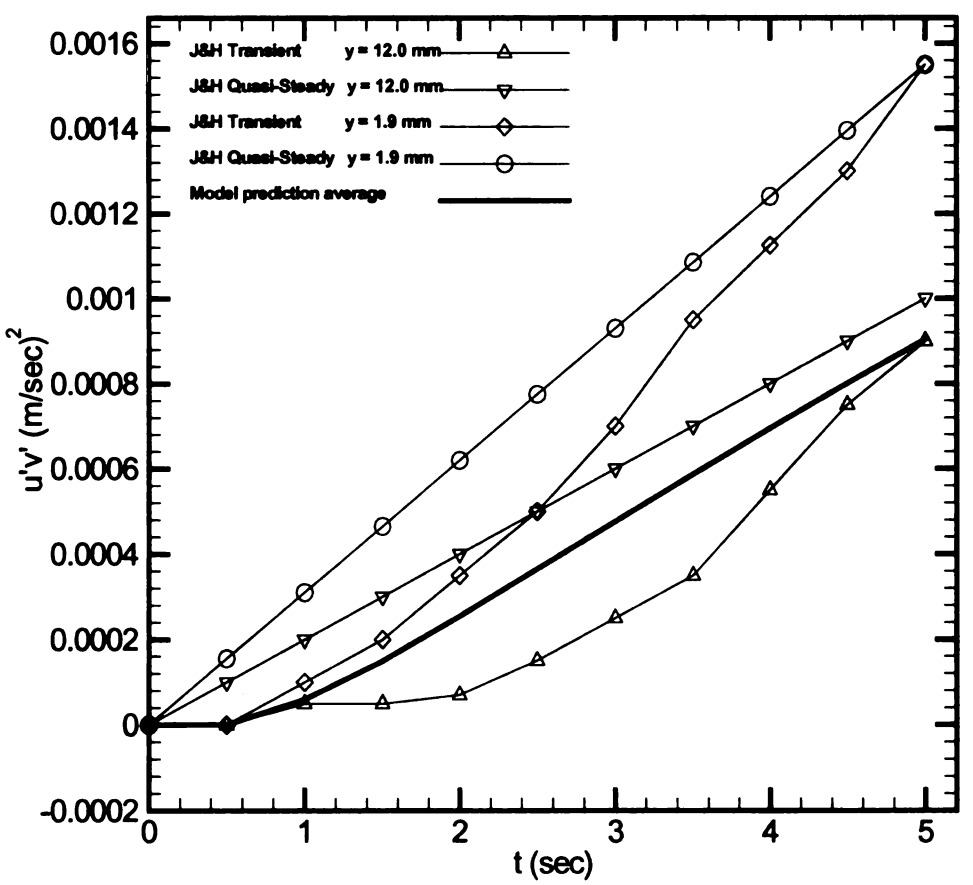

Figure 5.2: Comparison of development of Reynolds shear stress for a linear ramp acceleration transient for 5 seconds from Reynolds number of 7000 to 42500 in a 50.4 mm diameter pipe.

5.6 Laplace Transformation and Solutions

The Laplace transform technique elegantly transforms the PDE in equation (5.3) to a linear ODE, for which a solution relating $\dot{m}(t)$ to $\partial p/\partial x$ can be found in convolution integral form, as was done in the unsteady laminar flow case. Laplace transforming equation (5.3) with $\mathcal{L}[\partial\tilde{u}/\partial t] = s\hat{u} - u_0$ and rearranging,

$$\nu\frac{d^2\hat{u}}{dr^2} + \frac{\nu}{r}\frac{d\hat{u}}{dr} - \frac{1}{r}\widehat{uv} - \frac{\partial\widehat{(uv)}}{\partial r} - s\hat{u} = \frac{1}{\rho}\frac{\partial\hat{p}}{\partial x} \tag{5.10}$$

The model proposed in equation (5.6) can be rewritten as

$$-\widehat{u'v'}(t) = W(t) * \frac{\partial\tilde{f}(r,t)}{\partial t} \tag{5.11}$$

where $\tilde{f}(r,t) = a\,\partial\tilde{u}/\partial r$. In the Laplace transformed domain, equation (5.11) can be rewritten as

$$-\widehat{u'v'} = \widehat{W}(s)s\hat{f}(r,s) \tag{5.12}$$

Here $\widehat{W}(s)$ is a function of s only i.e. turbulence is assumed to be well mixed with the same average turbulent memory across the entire flow. Similarly

$$\frac{d}{dr}\left[-\widehat{u'v'}\right] = \frac{d}{dr}\left[\widehat{W}(s)sf(s)\right] = s\widehat{W}(s)\frac{d\hat{f}(s,r)}{dr} \tag{5.13}$$

Thus we have

$$-\widehat{u'v'} = s\widehat{W}(s)\left(a\frac{d\hat{u}}{dr}\right) \tag{5.14}$$

and

$$\frac{-d\left(\widehat{u'v'}\right)}{dr} = s\widehat{W}(s)\left(a\frac{d^2\hat{u}}{dr^2}\right) \tag{5.15}$$

Substituting $\widehat{W}(s)$, equation (5.14) and equation (5.15) into equation (5.10), we have

$$\begin{aligned} &\nu\frac{d^2\hat{u}}{dr^2}+\frac{\nu}{r}\frac{d\hat{u}}{dr}+\frac{1}{r}\left(\frac{s+\beta+\alpha s}{s+\beta}\right)\left(a\frac{d\hat{u}}{dr}\right) \\ &+\left(\frac{s+\beta+\alpha s}{s+\beta}\right)\left(a\frac{d^2u}{dr^2}\right)-s\hat{u}=\frac{1}{\rho}\frac{\partial\hat{p}}{\partial x} \end{aligned} \tag{5.16}$$

Substituting $\hat{F}=(1/\rho)(\partial\hat{p}/\partial x)$ in equation (5.16) and rearranging

$$\frac{d^2\hat{u}}{dr^2}+\frac{1}{r}\frac{d\hat{u}}{dr}-\frac{s}{\nu\left(1+\dfrac{(s+\beta+\alpha s)a}{\nu(s+\beta)}\right)}\hat{u}=\frac{\hat{F}}{\nu\left(1+\dfrac{(s+\beta+\alpha s)a}{\nu(s+\beta)}\right)} \tag{5.17}$$

The ordinary differential equation (5.17) is then solved with the same boundary conditions as for the laminar case and yields the following results:

$$\hat{u}(r,s)=\frac{\hat{F}}{s}\left[\frac{J_0\left[-ir\sqrt{\dfrac{s}{X\nu}}\right]}{J_0\left[-iR\sqrt{\dfrac{s}{X\nu}}\right]}-1\right] \tag{5.18}$$

where

$$X=1+\frac{a}{\nu}\left(1+\frac{\alpha s}{s+\beta}\right) \tag{5.19}$$

Changes in the mean velocity, and hence flow rate, in the Laplace transform domain may be found by integrating the transform of the momentary velocity field over

the cross sectional area of the pipe. Using equation (2.13) and substituting (5.18) into (2.13) and simplifying,

$$\hat{U}(s)=\hat{F}\frac{1}{s}\left[\frac{2I_1\left[R\sqrt{\frac{s}{\left(1+\frac{a}{\nu}\left(1+\frac{\alpha s}{s+\beta}\right)\right)\nu}}\right]}{R\sqrt{\frac{s}{\left(1+\frac{a}{\nu}\left(1+\frac{\alpha s}{s+\beta}\right)\right)\nu}}J_0\left[-iR\sqrt{\frac{s}{\left(1+\frac{a}{\nu}\left(1+\frac{\alpha s}{s+\beta}\right)\right)\nu}}\right]}-1\right] \tag{5.20}$$

where I_1 is a modified Bessel function of first kind of order one and J_o is the Bessel function of first kind of order zero. Multiplying and dividing by s to allow inverse Laplace transformation, equation (5.20) becomes

$$\hat{U}(s)=s\hat{F}\frac{1}{s^2}\left[\frac{2I_1\left[R\sqrt{\frac{s}{\left(1+\frac{a}{\nu}\left(1+\frac{\alpha s}{s+\beta}\right)\right)\nu}}\right]}{R\sqrt{\frac{s}{\left(1+\frac{a}{\nu}\left(1+\frac{\alpha s}{s+\beta}\right)\right)\nu}}J_0\left[-iR\sqrt{\frac{s}{\left(1+\frac{a}{\nu}\left(1+\frac{\alpha s}{s+\beta}\right)\right)\nu}}\right]}-1\right] \tag{5.21}$$

Here $s\hat{F}=\partial\hat{F}/\partial t+\hat{F}_0\delta(t)$. Taking the inverse Laplace transform of the equation (5.21)

$$U(t)=\frac{\partial F}{\partial t}*\mathcal{L}^{-1}\left[\frac{1}{s^2}\left[\frac{2I_1\left[R\sqrt{\frac{s}{\left(1+\frac{a}{\nu}\left(1+\frac{\alpha s}{s+\beta}\right)\right)\nu}}\right]}{R\sqrt{\frac{s}{\left(1+\frac{a}{\nu}\left(1+\frac{\alpha s}{s+\beta}\right)\right)\nu}}J_0\left[-iR\sqrt{\frac{s}{\left(1+\frac{a}{\nu}\left(1+\frac{\alpha s}{s+\beta}\right)\right)\nu}}\right]}-1\right]\right] \tag{5.22}$$

with the symbol * denoting the convolution operation. We can rewrite this equation as

$$U(t)=\frac{\partial F}{\partial t}*\mathcal{H}(t) \tag{5.23}$$

where $\mathcal{H}(t)=\mathcal{L}^{-1}\left[\widehat{\mathcal{H}}(s)\right]$ and $\widehat{\mathcal{H}}(s)$ is given by

$$\widehat{\mathcal{H}}(s)=\frac{1}{s^2}\left[\frac{2I_1\left[R\sqrt{\frac{s}{\left(1+\frac{a}{\nu}\left(1+\frac{\alpha s}{s+\beta}\right)\right)\nu}}\right]}{R\sqrt{\frac{s}{\left(1+\frac{a}{\nu}\left(1+\frac{\alpha s}{s+\beta}\right)\right)\nu}}J_0\left[-iR\sqrt{\frac{s}{\left(1+\frac{a}{\nu}\left(1+\frac{\alpha s}{s+\beta}\right)\right)\nu}}\right]}-1\right] \tag{5.24}$$

The mean velocity to pressure gradient results can be derived from equation (5.22) as

$$U(t)=U(0)+\int_0^t\left(\frac{1}{\rho}\frac{\partial^2 p}{\partial x\partial t}(t-t')-\frac{1}{\rho}\frac{\partial^2 p}{\partial x\partial t}(0)\right)\mathcal{L}^{-1}\left[\widehat{\mathcal{H}}(s)\right]dt' \tag{5.25}$$

Cumulative through-flow may be found by integrating equation (5.25) as

$$\int_0^t U(t)\,dt=\int_0^t U(0)\,dt+\int_0^t\left(\frac{1}{\rho}\frac{\partial p}{\partial x}(t-t')-\frac{1}{\rho}\frac{\partial p}{\partial x}(0)\right)\mathcal{L}^{-1}\left[\widehat{\mathcal{H}}(s)\right]dt' \tag{5.26}$$

The flow rate to pressure gradient relationship can be expressed as the sum of a steady state and a transient contribution by rewriting

$$\mathcal{L}^{-1}[\ ]=\mathcal{L}^{-1}[\ ]_{t\to\infty}+\left(\mathcal{L}^{-1}[\ ]-\mathcal{L}^{-1}[\ ]_{t\to\infty}\right)$$

Then equation (5.26) can be expressed as

$$\int_0^t U(t)\,dt=\int_0^t U(0)\,dt+\int_0^t\left(\frac{1}{\rho}\frac{\partial p}{\partial x}(t-t')-\frac{1}{\rho}\frac{\partial p}{\partial x}(0)\right)\mathcal{L}^{-1}\left[\widehat{\mathcal{H}}(s)\right]_{t\to\infty}dt'$$
$$+\int_0^t\left(\frac{1}{\rho}\frac{\partial p}{\partial x}(t-t')-\frac{1}{\rho}\frac{\partial p}{\partial x}(0)\right)\left(\mathcal{L}^{-1}\left[\widehat{\mathcal{H}}(s)\right]-\mathcal{L}^{-1}\left[\widehat{\mathcal{H}}(s)\right]_{t\to\infty}\right)dt' \tag{5.27}$$

Using the residue theorem, at $s=0$ or at $t=\infty$, we have

$$\mathcal{L}^{-1}\left[\widehat{\mathcal{H}}(s)\right]_{t\to\infty}=-\frac{R^2}{8(a+\nu)} \tag{5.28}$$

Now for steady flow,

$$\int_0^t U(0)\,dt=\int_0^t\frac{1}{\rho}\frac{\partial p(0)}{\partial x}\mathcal{L}^{-1}\left[\widehat{\mathcal{H}}(s)\right]_{t\to\infty}=\frac{-R^2}{8\rho(a+\nu)}\int_0^t\frac{\partial p(0)}{\partial x}dt \tag{5.29}$$

For initially steady flow, equation (5.27) becomes

$$\int_0^t U(t)\,dt=\frac{-R^2}{8\rho(a+\nu)}\int_0^t\frac{\partial p(t')}{\partial x}dt'$$
$$+\int_0^t\left(\frac{1}{\rho}\frac{\partial p}{\partial x}(t-t')-\frac{1}{\rho}\frac{\partial p}{\partial x}(0)\right)\left(\mathcal{L}^{-1}\left[\widehat{\mathcal{H}}(s)\right]-\mathcal{L}^{-1}\left[\widehat{\mathcal{H}}(s)\right]_{t\to\infty}\right)dt' \tag{5.30}$$

where $\mathcal{L}^{-1}\left[\widehat{\mathcal{H}}(s)\right]-\mathcal{L}^{-1}\left[\widehat{\mathcal{H}}(s)\right]_{t\to\infty}$ is a weighting function and $\mathcal{L}^{-1}\left[\widehat{\mathcal{H}}(s)\right]$ is given by

$$\mathcal{L}^{-1}\left[\widehat{\mathcal{H}}(s)\right]=\frac{-R^2}{8(a+\nu)}+\sum_{j=1}^{j=\infty}\left[\begin{array}{l}\dfrac{2e^{s_j^+t}}{\left(\dfrac{m^{+^2}s^+R^2}{2\nu}-\dfrac{m^{+^4}s^{+^2}R^2a}{2\nu^2}\left(\dfrac{\alpha}{(s^++\beta)}-\dfrac{\alpha s^+}{(s^++\beta)^2}\right)\right)s_j^+} \\ +\dfrac{2e^{s_j^-t}}{\left(\dfrac{m^{-^2}s^-R^2}{2\nu}-\dfrac{m^{-^4}s^{-^2}R^2as}{2\nu^2}\left(\dfrac{\alpha}{(s^-+\beta)}-\dfrac{\alpha s^-}{(s^-+\beta)^2}\right)\right)s_j^-}\end{array}\right] \tag{5.31}$$

with

$$s_j^+=\frac{\nu}{2R^2}\left(-\left(\frac{\beta R^2}{\nu}+\eta_j^2\left(1+\frac{a}{\nu}(1+\alpha)\right)\right)\right)+\sqrt{\left(\frac{\beta R^2}{\nu}+\eta_j^2\left(1+\frac{a}{\nu}(1+\alpha)\right)\right)^2-4\eta_j^2\frac{\beta R^2}{\nu}\left(1+\frac{a}{\nu}\right)}$$

$$s_j^-=\frac{\nu}{2R^2}\left(-\left(\frac{\beta R^2}{\nu}+\eta_j^2\left(1+\frac{a}{\nu}(1+\alpha)\right)\right)\right)-\sqrt{\left(\frac{\beta R^2}{\nu}+\eta_j^2\left(1+\frac{a}{\nu}(1+\alpha)\right)\right)^2-4\eta_j^2\frac{\beta R^2}{\nu}\left(1+\frac{a}{\nu}\right)}$$

$$m^+=\left(\frac{1}{1+\frac{a}{\nu}\left(1+\frac{\alpha s^+}{s^++\beta}\right)}\right)^{1/2}$$

and

$$m^{-} = \left(\frac{1}{1 + \frac{a}{\nu}\left(1 + \frac{\alpha s^{-}}{s^{-} + \beta}\right)} \right)^{1/2}$$

The behavior of the weighting function $\mathcal{L}^{-1}\left[\widehat{\mathcal{H}}(s)\right] - \mathcal{L}^{-1}\left[\widehat{\mathcal{H}}(s)\right]_{t\to\infty}$ is controlled by the three parameters: a, β and α. The parameter a represents the overall eddy viscosity and governs the initial magnitude of the weighting function. As explained in 5.5.1, it should scale in proportion to Reynolds number. The effect of the magnitude of β is not very significant during the initial stage of the weighting function because of its $e^{-\beta t}$ dependence. The initial response remains the same for short times and then it starts to relax to zero at faster rates with increasing β. In comparison to the effect of parameter β, the effect of α is more pronounced. It is more significant during the initial phase of the weighting function, for fixed values of a and β. In this phase, the weighting function decays faster for lower values of α, and decays slower for higher values of α. In essence, for higher Reynolds numbers and values of β, the lower values of α will cause transient turbulent shear stress to reach their quasi-steady turbulent shear stress values faster.

Equation (5.30) is similar to equation (2.43) and offers a similar solution to the unsteady pipe flow problem in the turbulent regime. This equation represents a quasi-steady term supplemented by an unsteady correction term to account for the flow memory during transients. As can be inferred from equation (5.30), the quasi-steady term underestimates the flow rate during deceleration and overestimates it during acceleration, as was the case for laminar flow.

Chapter 6 Turbulent Flow Experimental Results and Discussion

6.1 Turbulent Flow Experiments

The main objective of the turbulent flow experiments was to determine the applicability of the turbulent shear stress model developed in Chapter 5 in unsteady turbulent duct flows. In this series of turbulent flow experiments, the methodology used in laminar flow experiments was followed. However, due to limitations of the experimental setup for turbulent flows, only steady, accelerating and decelerating turbulent flows with varying accelerating and decelerating flow rates were studied. In these experiments two working fluids were used. One fluid had a kinematic viscosity υ of 1.414×10^{-6} m^2/s and a density ρ of 1040 kg/m^3 and the second had a kinematic viscosity υ of 1.515×10^{-6} m^2/s and a density ρ of 1030 kg/m^3.

In accelerating flow experiments, the acceleration was varied from 0.04 to 0.26 m/s^2 and, in decelerating flow experiments, the deceleration was varied from 0.11 to 0.325 m/s^2. All transient turbulent experiments were designed to ensure that Reynolds numbers remained above 3500, thereby avoiding relaminarization and the transition region during acceleration and deceleration transients. The departure from the quasi-steady state was ascertained using the turbulent unsteadiness parameter, a turbulent counter part to the laminar unsteadiness parameter, defined as

$$\frac{1}{u(t)}\frac{du}{dt}(t)\frac{R^2}{\nu\left(\frac{a}{\nu}+1\right)} \tag{6.1}$$

which is large during very severe transients.

6.2 Model Calibration

The parameters a, α and β given in the turbulent shear stress model $-\widetilde{u'v'} = \left[H(t) + \alpha e^{-\beta t}\right] a * \frac{\partial^2 \tilde{u}}{\partial r \partial t}$ must be calibrated from unsteady flow experiments if they are to be used to determine the accumulated mass according to the unsteady turbulence model developed in Chapter 5, which is

$$\int_0^t U(t)\,dt = -\frac{R^2}{8\rho(a+\nu)} \int_0^t \frac{\partial p(t')}{\partial x} dt' + \int_0^t \left(\frac{1}{\rho}\frac{\partial p}{\partial x}(t-t') - \frac{1}{\rho}\frac{\partial p}{\partial x}(0) \right) \left(\mathcal{L}^{-1}\left[\widehat{\mathcal{H}}(s)\right] - \mathcal{L}^{-1}\left[\widehat{\mathcal{H}}(s)\right]_{t\to\infty} \right) dt' \tag{5.30}$$

where

$$\widehat{\mathcal{H}}(s) = \frac{1}{s^2}\left[\frac{2I_1\left[R\sqrt{\frac{s}{\left(1+\frac{a}{\nu}\left(1+\frac{\alpha s}{s+\beta}\right)\right)\nu}} \right]}{R\sqrt{\frac{s}{\left(1+\frac{a}{\nu}\left(1+\frac{\alpha s}{s+\beta}\right)\right)\nu}}\, J_0\left[-iR\sqrt{\frac{s}{\left(1+\frac{a}{\nu}\left(1+\frac{\alpha s}{s+\beta}\right)\right)\nu}} \right]} - 1 \right] \tag{5.24}$$

Initially a rough range of parameters was explored by keeping one parameter fixed and changing the other two. This gave us an insight into how parameters such as α and β affect the magnitude and decay rate of the weighting function, thereby controlling the final values of the accumulated mass inferred from pressure drop measurements in the turbulent flow experiments. These parameters should ideally be modeled in terms of the flow properties. The dimensionless parameter α was initially modeled

as $(u_\tau/(dU_{CL}/dt))(u_\tau/R)$, as a scaling of the degree of unsteadiness, but this dependence was not consistent with experimental results. When tested against Jackson and He's [24] experimental data, a value of α = 8.0 yielded a comparable delay in the adjustment of the Reynolds shear stresses after imposing transients in their pipe flows. α was then tentatively modeled as if a constant for all types of turbulent transient pipe flows, including the ones measured experimentally in this study.

The reciprocal time scale β was initially scaled on u_{CL}/R. The relatively large values of u_{CL} and small pipe radius made changes in this parameter too extreme to match the data of this study so this was later rescaled on u_τ/R where u_τ is the friction velocity at the start of the transient. It was also noticed that values of β of 30 or above do not affect the weighting function significantly and the decay rate remained almost unchanged at higher values. The data of this study could be matched more closely by setting β equal to a multiple of u_τ/R with u_τ calculated from initial flow conditions. For the turbulent flow experiments of this study, $u_\tau(0)/R$ varied from 9 to about 19 $\sec^{-1}$. The data could be matched by setting $\beta = 1.0\frac{u_\tau(0)}{R}$, where the 1.0 is the calibration factor, $u_\tau = \sqrt{\tau_w/\rho}$, $\tau_w = 0.0395\rho^{0.75}\mu^{0.25}d^{-0.25}u^{1.75}$ and $\mathrm{Re}_\tau = u_\tau d/\nu$.

Parameter *a,* which has the units of eddy viscosity and represent the average eddy viscosity across the pipe, was also calibrated against the steady flow. For each transient flow, the initial Reynolds number during steady flow was used to determine the value of a i.e. $a = \frac{\kappa\nu Re_\tau}{\mathcal{L}^{-1}\left[\frac{1}{s}+\frac{\alpha}{s}+\beta\right]}$ for that particular experiment, which is also consistent with the

expression $\nu_t/\nu = \kappa Re_\tau$ given by (Arpaci and Larsen [42]). It was noticed that calibration of a during steady flow i.e. *a(0)* has a vital effect during the transients and it needs to be calibrated precisely. Ideally, the value of *a(t)* should be based on the momentary value of $u_\tau(t)$ at each time step in a transient flow to model the quasi-steady eddy viscosity accurately. A more convenient way of including the dependence of eddy viscosity on $u_\tau(t)$ is to note that $u_\tau \sim \sqrt{\partial p/\partial x}$ in steady flows (White [47]), so we can write $a(t) = a(0)\left[\frac{dp(t)/dx}{dp(0)/dx}\right]^{1/2}$, where $dp(t)/dx$ is the pressure gradient during transients and $dp(0)/dx$ is the pressure gradient before the start of transients. In this way, we can scale the eddy viscosity only at the start of the transients and on the measured instantaneous pressure gradient. In summary, calibration against experimental data led to the following values for the model coefficients: α = 8.0; $\beta = 1.0\frac{u_\tau(0)}{R}, a(0) = 0.0145\ \nu Re_\tau(0)$ which depends only on initial flow conditions. These values of calibration coefficients are used in all predictions given in the following sections.

6.3 Experimental Results

In the subsequent sections, selective results from a range of experiments are presented, with slow, moderate, and severe acceleration and deceleration rates. In all experiments transients were imposed on an initially steady flow, as was done in the laminar case, to allow calibration of *a(0)*. The pressure sensors were calibrated prior to these experiments against a manometer over a range of steady flow rates that bounded the pressures experienced in the transient flow experiments.

6.3.1 Steady Flow Results

Before conducting the accelerating and decelerating flow experiments, the applicability of equation (5.30) was checked against steady turbulent flow experimental data.

$$\int_0^t U(t)\,dt = -\frac{R^2}{8\rho(a+\nu)}\int_0^t \frac{\partial p(t')}{\partial x}dt' + \int_0^t \left(\frac{1}{\rho}\frac{\partial p}{\partial x}(t-t') - \frac{1}{\rho}\frac{\partial p}{\partial x}(0)\right)\left(\mathcal{L}^{-1}\left[\widehat{\mathcal{H}}(s)\right] - \mathcal{L}^{-1}\left[\widehat{\mathcal{H}}(s)\right]_{t\to\infty}\right)dt' \tag{5.30}$$

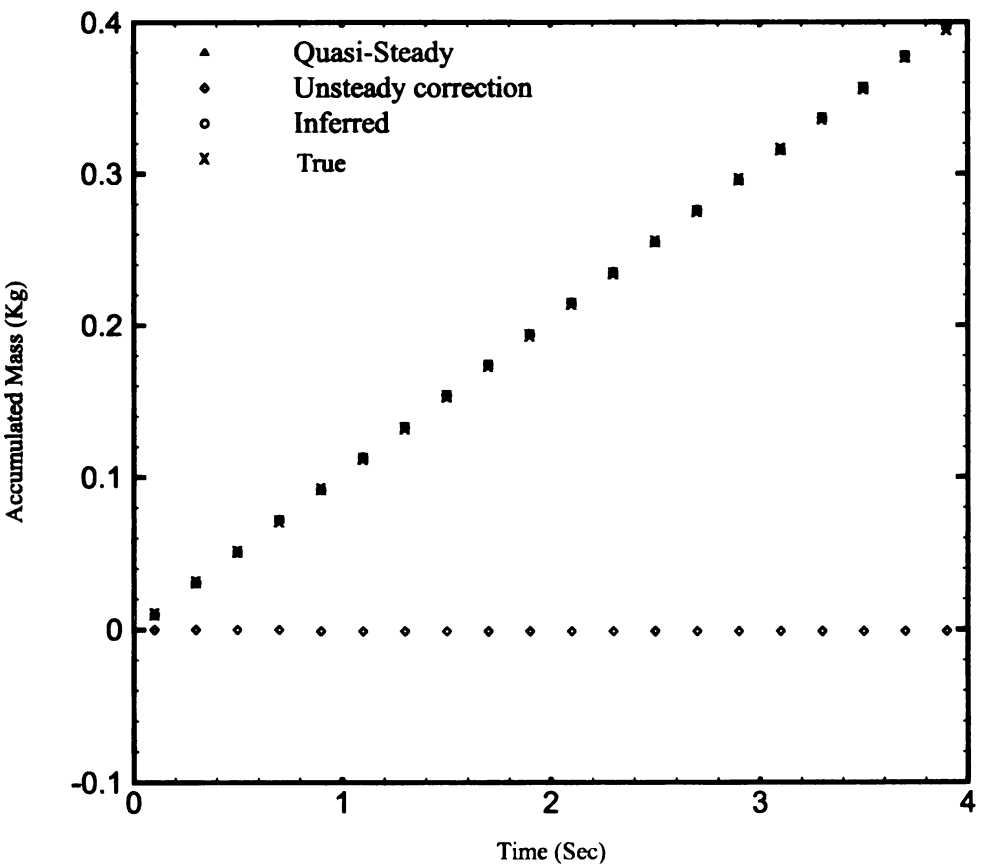

Figure 6.1: Steady flow at a Reynolds number of 5250

In the steady flow experiments, the $\partial p/\partial x$ term remains unchanged so that $(\partial p(t-t')/\partial x)-(\partial p(0)/\partial x)=0$. Obviously there is no unsteady correction value so the accumulated mass predicted by the pressure gradient data, and measured by the load cell data can be compared directly. Figure 6.1 shows the cumulative liquid mass in this turbulent steady flow case with quasi-steady, inferred and true accumulated masses yielding exactly the same results. The significance of this agreement between the data is that the eddy viscosity ν_t and the pressure transducers are correctly calibrated at this flow rate, and that the unsteady correction algorithm performs correctly. In this figure, the time range of 0 to 4 seconds corresponds to $\frac{t}{R/u_0}$ of 0 to 1050.

6.3.2 Accelerating Flow Experiments

The accelerating flow experiments can be characterized by the unsteadiness factor (6.1) imposed during the transients with varying magnitudes of acceleration ranging from 0.25 to 0.9. In this series of experiments, the flow rate was controlled manually by opening and closing the valve, as in the laminar flow experiments. The initial Reynolds number at the start of the transient was chosen to be around 3900 and it was increased to about 5300 over different time periods. Ideally a much broader range of minimum and maximum Reynolds numbers would be desired, but these experiments were restricted to this Reynolds number range because of the limited elevation of the header tank and the corresponding maximum flow rate through pipe of this length and diameter.

In the slow acceleration experiment shown in Figure 6.2, the flow was initially kept steady for about one second and then was gradually accelerated. In this figure, the cumulative mass is plotted as a function of time, together with the quasi-steady, unsteady

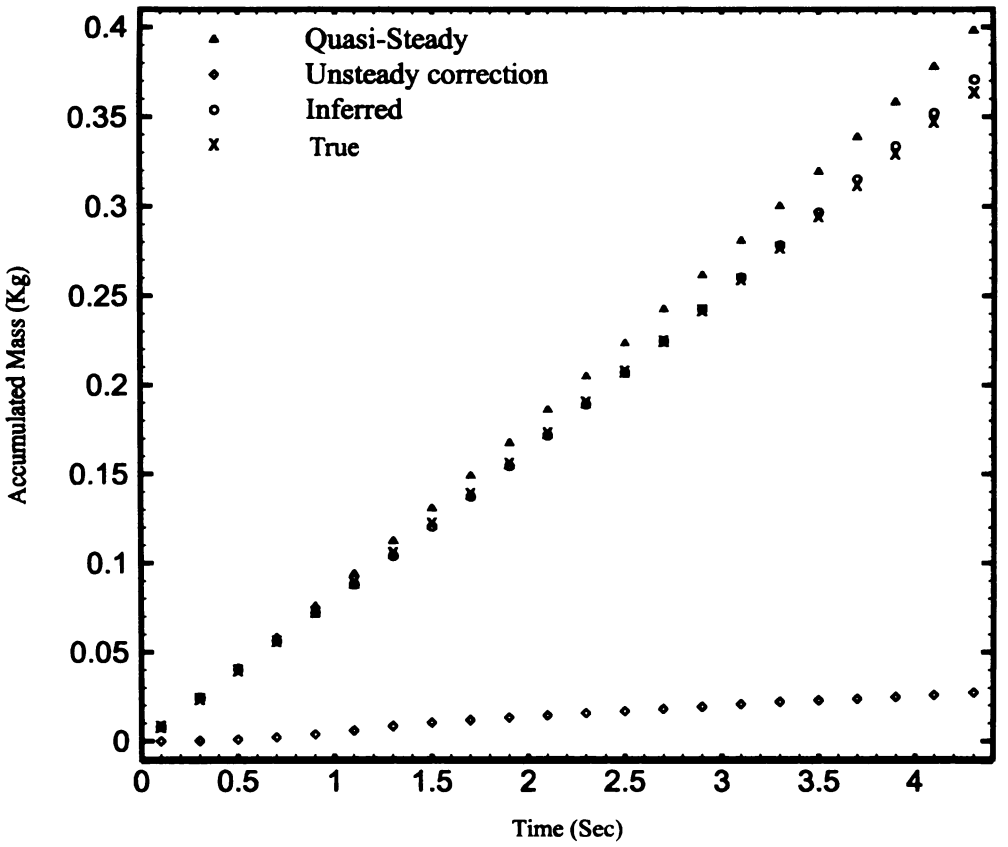

Figure 6.2: Initially steady flow that is then gradually accelerated, Reynolds number increased from 4176 to 5128, maximum unsteadiness factor 0.25, $Re_\tau(0) = 293$

correction, and unsteady inferred cumulative masses determined using the model and calibration coefficients presented in 6.2. It is evident from this figure that the quasi-steady term overestimates the accumulated mass during acceleration and that this overestimation is corrected almost perfectly by the unsteady correction data, resulting in a good agreement with the true accumulated liquid mass measured by the load cell data. A similar trend is found in the moderate acceleration experiment, the results of which are shown in Figure 6.3. We observe a significant deviation between the quasi-steady accumulated mass and the true accumulated mass. This over-prediction by the quasi- steady

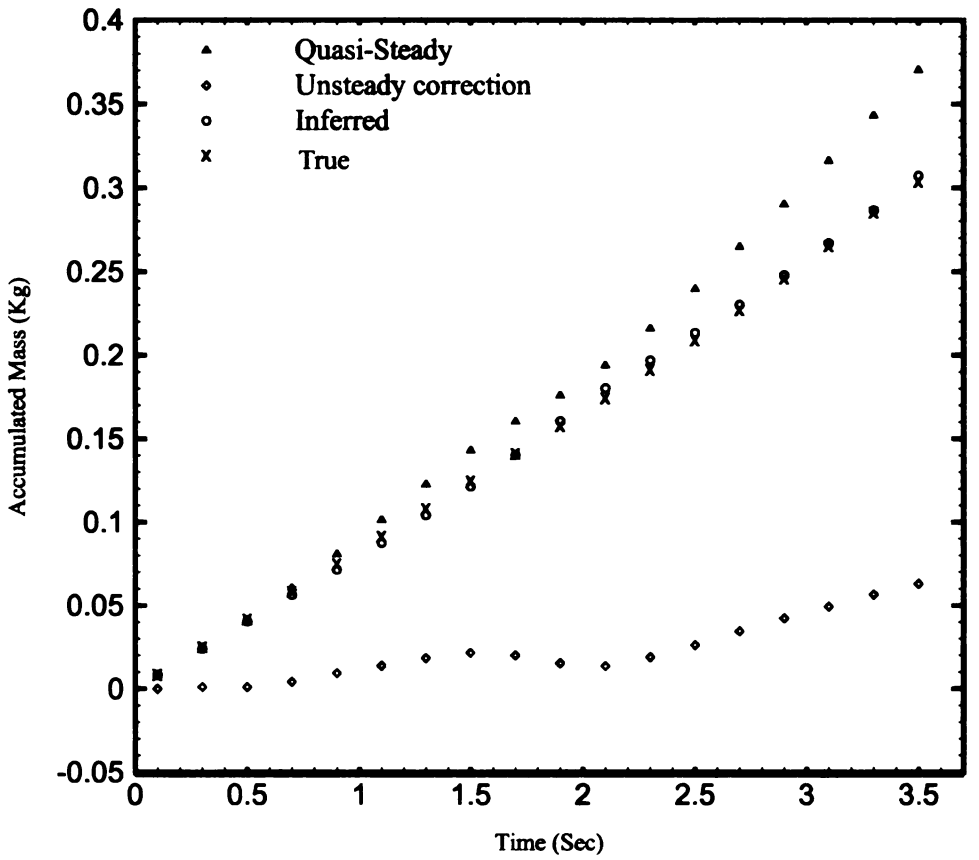

Figure 6.3:- Initially steady flow that is moderately accelerated; Reynolds number increased from 3800 to 4700, maximum unsteadiness factor 0.53, $Re_\tau(0) = 160$

measurement is compensated for by the unsteady correction term resulting in a good agreement between the predicted and true accumulated mass data.

Figure 6.4 shows the results of a severe acceleration case, in which a larger spread in accumulated mass data between quasi-steady, and true accumulated mass data is observed. This deviation from the quasi-steady value is completely compensated for by the unsteady correction term, resulting in good agreement between the true and inferred accumulated mass data.

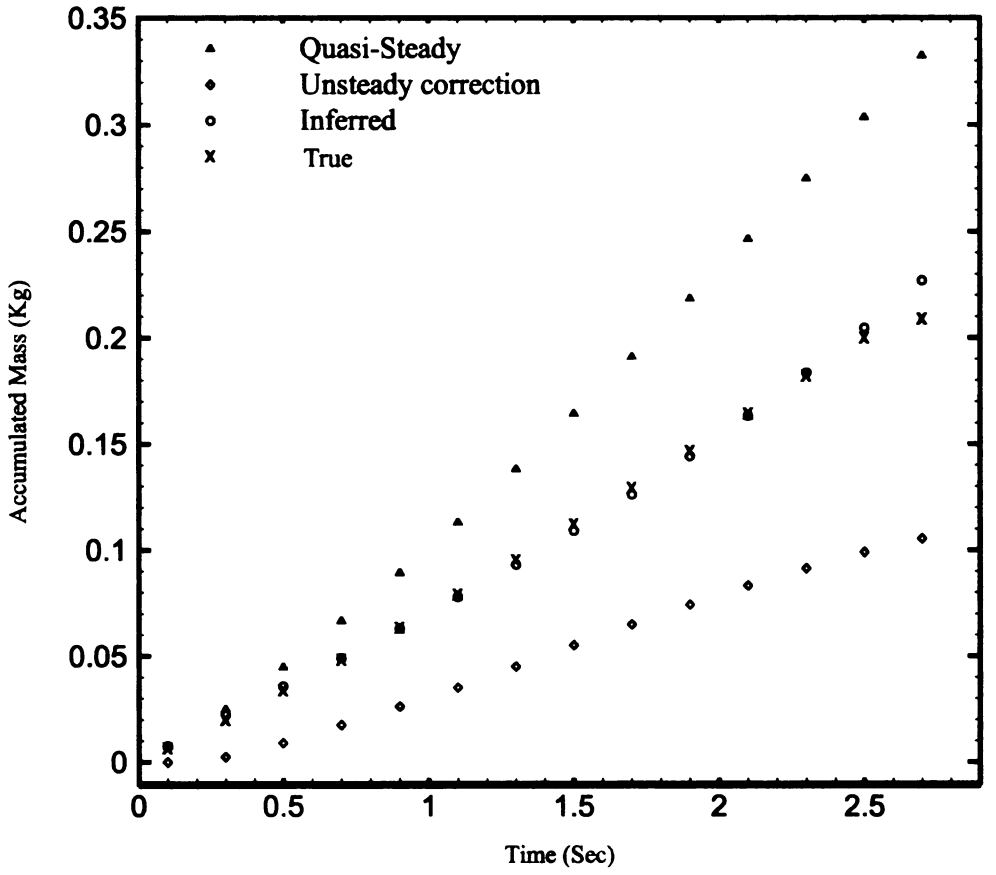

Figure 6.4:- Initially steady then suddenly accelerated flow, with Reynolds number increased from 3750 to 5200, maximum unsteadiness factor 0.90, $Re_\tau(0) = 192$

6.3.3 Decelerating Flow Experiments

The decelerating flow experiments were conducted in a similar manner to the laminar decelerating flow experiments. The flow was initially kept steady before decelerating from a higher Reynolds number to lower Reynolds number by partially closing the valve. In this case again varying magnitude of deceleration rate were imposed characterized by the unsteadiness factor ranging from 0.25 to 0.72. Figure 6.5 shows experimental data for a slow deceleration case, in which flow is initially kept steady for 3

seconds and then gradually decelerated. During steady flow there is no deviation among the quasi-steady, inferred, and reference accumulated mass since the unsteady correction is zero. After this phase, the quasi-steady term underestimates the accumulated mass which is in turn compensated for by the unsteady correction term. The resulting agreement between the inferred and true accumulated mass is within a few percent and is very good.

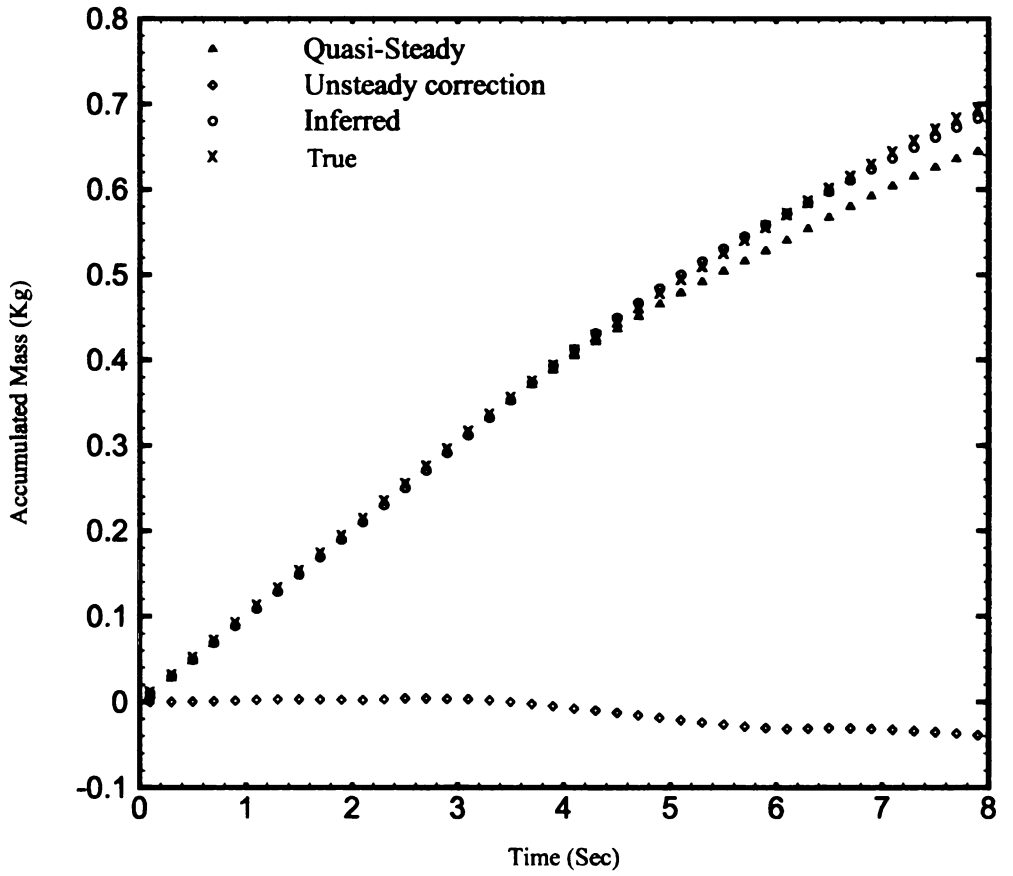

Figure 6.5:- Initially steady flow which is then slowly decelerated, with the Reynolds number reduced from 5255 to 3900, maximum unsteadiness factor 0.25, $Re_\tau(0) = 324$

Figure 6.6 shows experimental data from a moderate deceleration case with initially steady flow. In this case, a fairly good agreement is observed between the inferred and

true accumulated mass with the quasi-steady term underestimating the accumulated mass. Figure 6.7 shows data from a more severe deceleration case, as can be seen from the larger departure of quasi-steady accumulated mass data from the true accumulated mass data. The same trend of underestimation of accumulated mass is seen for the quasi-steady data, with the unsteady correction yielding a good agreement between the true and inferred accumulated masses.

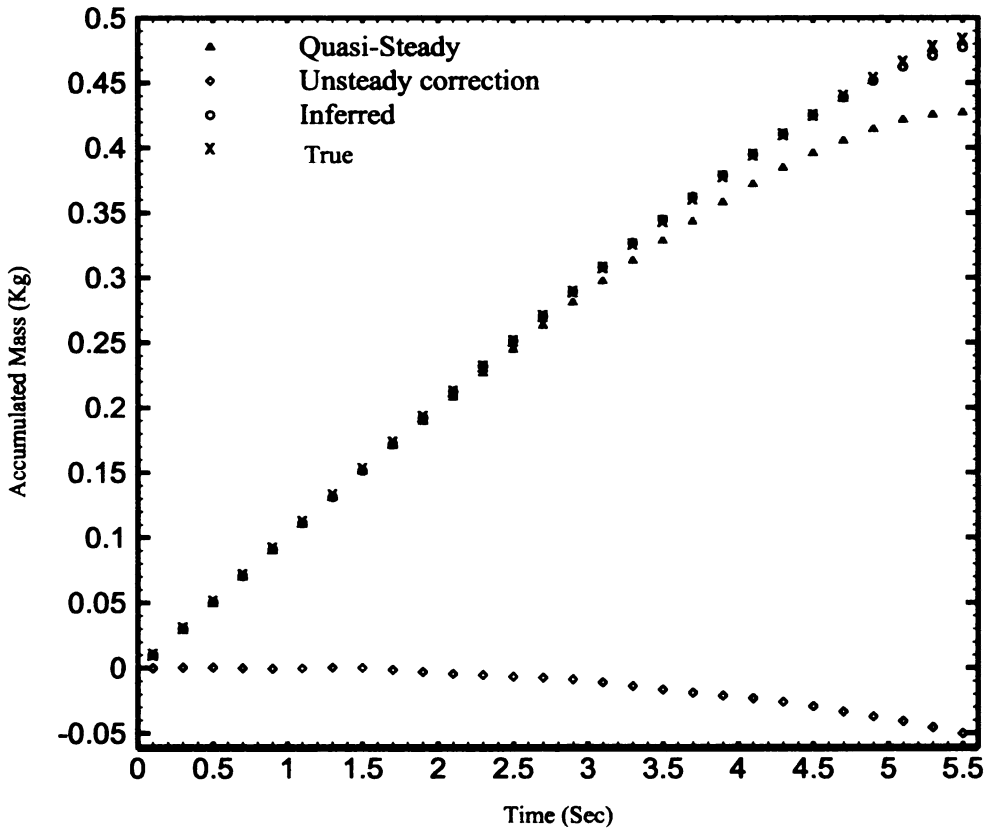

Figure 6.6:- Initially steady flow which is then moderately decelerated, with its Reynolds number reduced from 5196 to 3900, maximum unsteadiness factor 0.509, $Re_\tau(0) = 314$

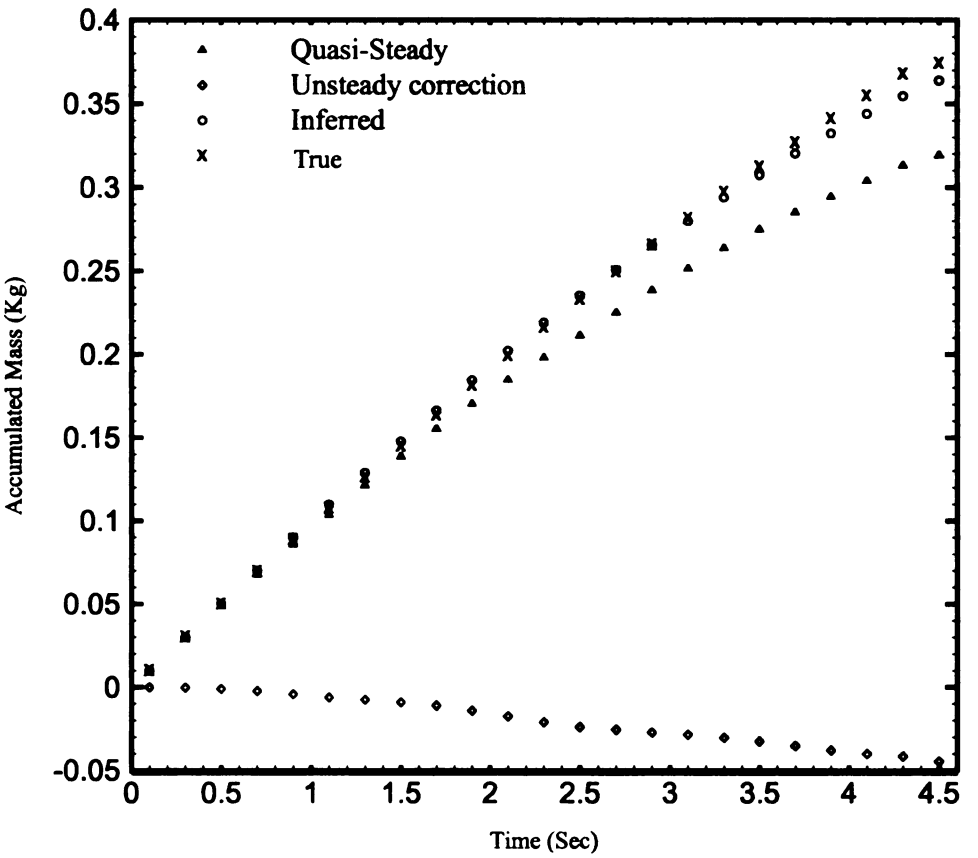

Figure 6.7:- Initially steady flow which is then rapidly decelerated, with its Reynolds number reduced from 5210 to 3500, maximum unsteadiness factor 0.72, $Re_\tau(0) = 318$

Based on the excellent agreement between experimental and modeled cumulative mass in accelerating and decelerating turbulent flows, it appears that the time-dependent model for the effect of Reynolds shear stress on flow rate shows promise for prediction of fully developed flows of arbitrary unsteadiness. For a simple linear model of a non linear effect like turbulence, it is significant that it is equally applicable to both accelerating and decelerating flows, without requiring further modeling or calibration. This finding is

interesting as some decelerating flows have also been observed to be de-stabilizing and the model can not account for such behavior.

The model requires three calibration constants, one of which is for the average eddy viscosity of the equivalent steady flow at the same pressure gradient/flow rate, and the other two are concerned with the unsteady response. The calibration constant α determines the delay in the development of turbulent shear stresses after imposing the transients and β effectively determines the short time response of the average Reynolds stresses. According to this calibration, the turbulent 'memory' time scale is $\sim 1.0\, R/u_\tau$ compared with the memory time scale of laminar flow of $\sim 0.7\, R^2/\nu$ (Brereton [15]).

Chapter 7 Conclusions and Recommendations

In this dissertation, a new approach for estimating unsteady flow rates in real time is proposed and experimentally investigated. We first presented an exact analytical solution to the unsteady laminar Navier-Stokes equations for incompressible fluids in ducts. The applicability of these solutions was then assessed in an experimental test facility mimicking an unsteady flow metering device. Using a time-history turbulence model, these laminar flow solutions were then extended to turbulent flows in ducts.

In the development of turbulent flow solutions, Reynolds shear stresses were first modeled in terms of eddy viscosity with memory effects. This model was then compared with the other researchers experimental data for validation. The Reynolds averaged momentum equation for duct flows was then solved analytically using the inverse Laplace transform technique. This turbulent flow solution was then calibrated and applied in the same experimental facility to test its applicability in real flow problems. The results show that reliable instantaneous unsteady flow metering is possible for laminar flows and that a simple time-dependent turbulence model appears to extend the technique to unsteady turbulent flows.

The main findings of the present study are summarized as follows:

- Unsteady flow metering in ducts, based on pressure drop measurements and an exact solution of the laminar, fully developed unsteady Navier Stokes equations, appears to be practical in pipe flows.

- The metering technique was demonstrated in a range of laminar unsteady pipe flows, in which it predicted almost perfectly the cumulative mass of liquid in a range of different transients.

- The successful implementation of this metering technique requires design/selection of pressure sensors with high sensitivity, high frequency response, high signal to noise ratio, and minimal zero drift, that can be flush-mounted in the pipe wall. There may be better choices than miniaturized piezo-resistive sensors.

- A simple turbulence model for unsteady bulk flow as a function of pressure gradient, which essentially replaces a laminar/molecular viscosity with eddy viscosity in the 'flow-memory' term, appears to provide a comparable way of predicting unsteady flow rates in turbulent duct flows.

- A three-coefficient model for unsteady turbulent bulk flow was calibrated and used to predict cumulative mass as a functional of pressure gradient in a range of accelerating and decelerating flows, using a single set of coefficients, with good accuracy.

- Unsteady turbulent flow rates under- and over-shoot the quasi-steady flow rates during decelerating and accelerating flow in the same way that laminar flows do.

- The success of a simple time history model for the average eddy viscosity in transient pipe flows suggests that this modeling approach might be useful in other turbulence modeling explorations.

The following recommendations are made for future work:

- Miniature pressure transducers (with good spatial resolution) that do not drift over time should be selected for unsteady flows over longer time periods.

- The applicability of the turbulence model should be tested against other unsteady flows like pulsatile or oscillatory flow.

- Similar metering approaches could be developed using $\dot{m} \sim \tau$ functional results derived in a similar manner.

Appendices

Appendix A

Experimental Configurations

In order to achieve the objectives of this research, a number of variations in the experimental instrumentations and setup were implemented before reaching the final configuration. These configurations are listed below in order of implementation.

Configuration 1 Initially an ACL 8112 HG data acquisition card was used for the purpose of data acquisition from the pressure sensors and Sentra electronic weigh scale. This card was discarded since it was not straightforward to program for continuous data acquisition.

Configuration 2 The data acquisition card was replaced with PCI-6023E card from National Instruments. This card enabled us to acquire buffered, continuous data and could be fully configured with the operating software of LabVIEW 4.0. However, a Sentra electronic weigh scale, which was connected to the serial port through an RS 233 cable, had a much slower data rate than the pressure drop data from pressure sensors, which was unsuitable for simultaneous mass and pressure-drop measurement.

Configuration 3 The Sentra electronic weigh scale was replaced with load cell of 10 lbs capacity, which enabled faster acquisition rate. It was noticed that the two pressure sensors had different thermal zero shift and zero offset characteristics under the same flow conditions. This resulted in different pressure sensor readings for the same flow rates.

Configuration 4 The two pressure sensors were replaced with one sensor. The pressure drop was then recorded with the single pressure sensor upstream with ambient

atmospheric pressure at the exit of the flow. The 10 lbs load cell also had a lower sensitivity. Therefore it was replaced with a load cell with a range of 2 lbs giving higher sensitivity.

Configuration 5 In configuration 4, the pressure sensor was excited with 10 volts DC continuously, which resulted in the thermal zero drift in its output. The data acquisition was then modified to excite the pressure sensor at 10 volts for a 5% of the duty cycle, at the end of which data was acquired. The excitation voltage was later on reduced to 5 volts DC with the output of the sensor amplified using Entran's IEM-15/05/1000R-WW amplifier. In turbulent flow, the same configuration was kept except for using a load cell with a capacity of 5 lbs to accommodate larger accumulated masses.

Appendix B Pressure Sensors

B.1 Strain Gauge Pressure Sensors

Strain gauge pressure sensors originally used a metal diaphragm with strain gauges bonded to it. A strain gauge measures the strain in a material subjected to applied stress. Metallic strain gauges depend only on dimensional change in resistance. A stress applied to the strip causes it to become slightly longer, narrower and thinner, thereby increasing its resistance.

Semiconductor strain gauges are widely used, both bonded and integrated into silicon diaphragms, because the response to applied stress is an order of magnitude larger than for metallic strain gauges. When the crystal lattice structure of silicon is deformed under applied stress, the resistance changes. This is called a piezoresistive effect. The most commonly strain gauges used in pressure sensors are: deposited strain gauges, bonded semiconductor strain gauges and piezoresistive integrated semiconductor strain gauges. The layout of the Entran EPE low pressure piezoresistive sensor is shown in Figure B.1.

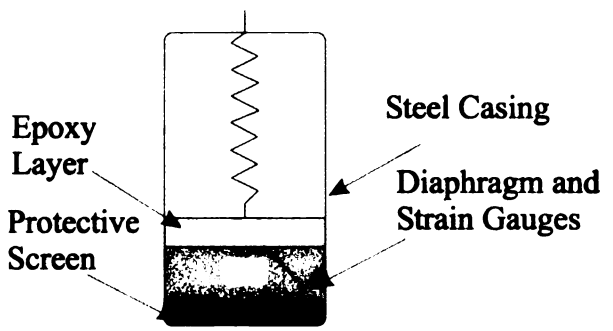

Figure B.1: Typical layout of the pressure sensor

B.2 Piezoresistive Integrated Semiconductor

Integrated circuitry (IC) processing is used to form the piezoresistors on the surface of a silicon wafer. There are four piezoresistors within the diaphragm area on the sensor. Two are subjected to tangential stress and two are subjected to radial stress when the diaphragm is deflected. They are connected in a four element bridge configuration as shown in Figure B.2 and provide the following output:

$$V_{out}/V_{cc} = \Delta R/R \tag{B.1}$$

where: V_{cc} is supply voltage; R is base resistance of the piezoresistor and ΔR is change in R with applied pressure and is at least 2.5 % of the full R.

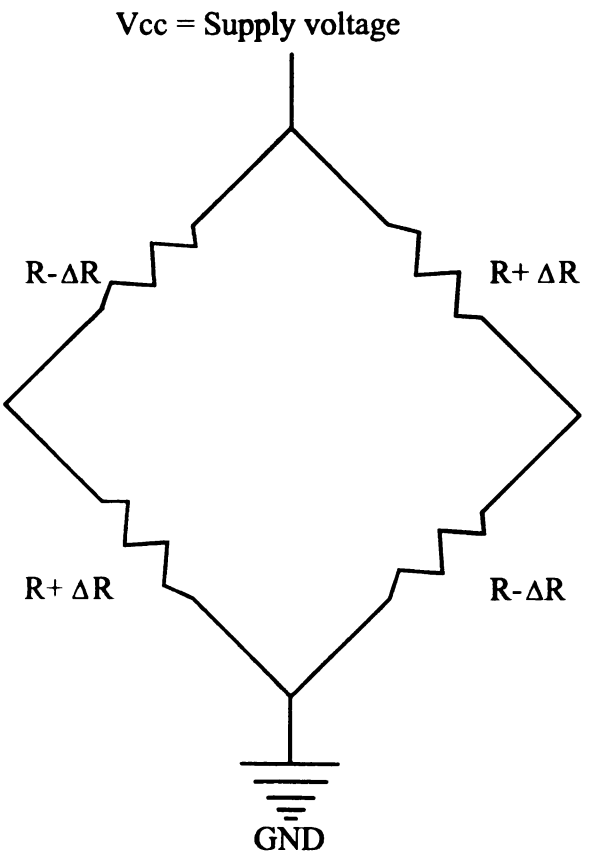

Figure B.2: Four element bridge configuration

The almost linear elasticity of the single crystal silicon is utilized by etching the back of the wafer to form the diaphragm as shown in Figure B.3. In the integrated construction, the high output of the bonded strain gauge is combined with the low hysteresis of the deposited strain gauge.

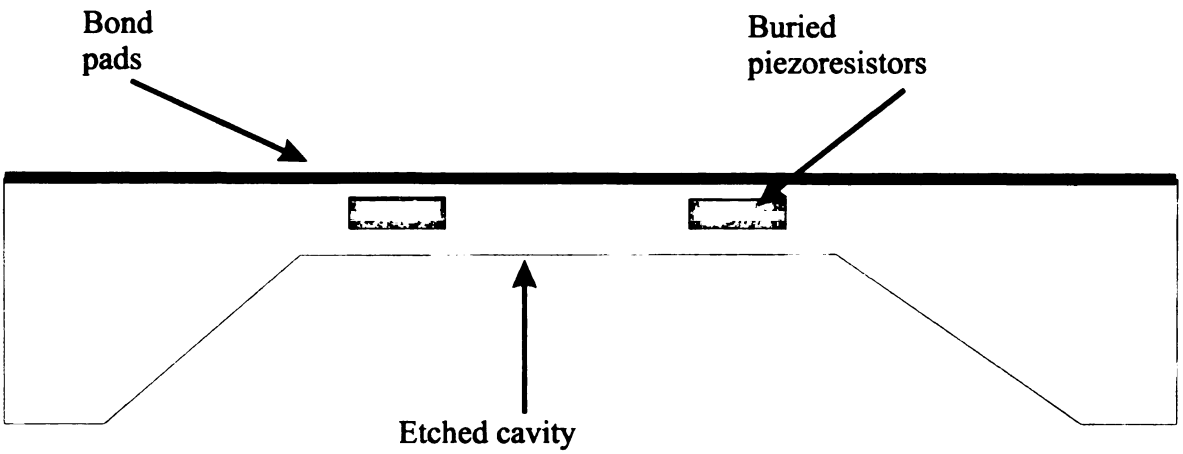

Figure B.3: Diaphragm of a piezoresistive pressure sensor

These piezoresistive pressure sensors can be configured to provide the absolute, differential or gauge pressure readings, depending on the reference. In Figure B.4, the diaphragm is shown deflecting under applied differential pressures.

(A)

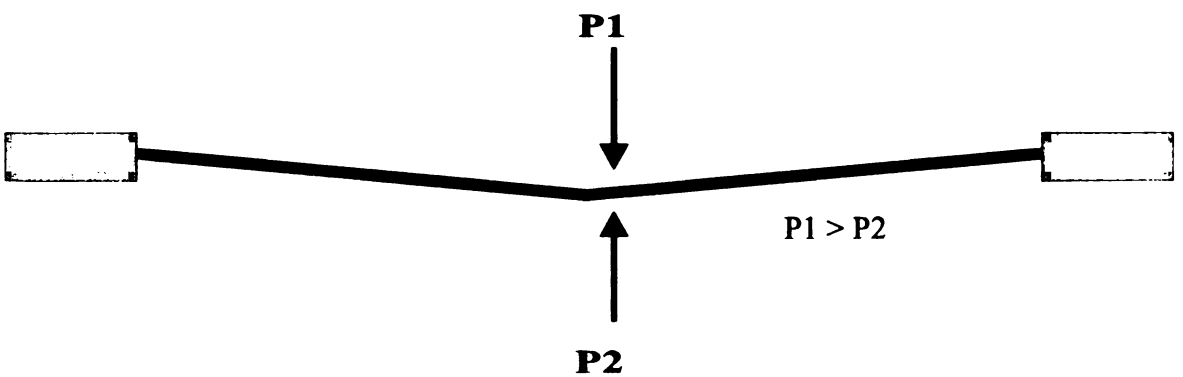

(B)

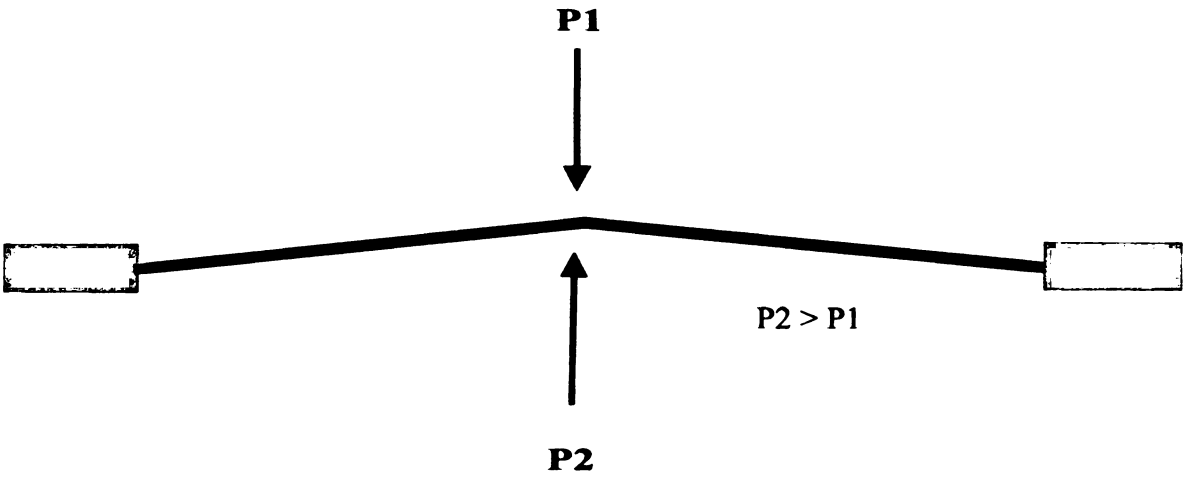

Figure B.4: Deflection of diaphragm under pressure

The circuitry needed for amplification, temperature compensation, and calibration is also included on the same IC. Various pressure ranges are accommodated by varying the diaphragm thickness and, for very low pressures, by selecting a large diaphragm diameter. Also, the small size means that it has a wide frequency response and may be used for dynamic pressure measurements without concerns about errors. Mechanical vibration and acceleration also have a negligible effect due to its small size.

B.3 Pressure Sensor Parameters

The pressure sensor used was the Entran EPE-N21-541 whose parameters are listed in Table B.1 below.

Pressure Range	2 PSI
Resonant Frequency	80KHz

Excitation	10 Volts DC
Thermal Sensitivity Shift	±4%/50 °C
Output (nom/min)	300/120
Thermal Zero Shift/50°C	±3% FSO
Zero Offset at 20°C	± 10 mV typical
Pressure Reference	Vented (gauge/relative)

Table B.1: Different parameters of sensors

B.3.1 Thermal Zero Shift (TZS)

The change of zero offset as a function of temperature is the thermal zero shift. It is expressed as either a %FSO for a specific temperature change such as ±1%FSO/50°C or in voltage units as ± 1mV/50°C and is a non-linear function. The specifications provided concern thermal equilibrium conditions for slow and stable changes of temperature within the compensated temperature range of the sensor. Thermal shocks or temperature gradients around the sensing surface of the sensor may cause zero offset changes greater than those specified. Thermal zero shift specifications are also a function of the heat sinking of the sensing diaphragm which results from the heat dissipation characteristics of the working fluid with the time allowed for the sensing element to warm up from the beginning of the excitation. During the experiments it was routine to

permit a 30 minute warm up before taking any experimental data. Powering a sensor with an excitation other than the one for which it was compensated for may also cause the thermal zero shift to vary from the stated specifications.

B.3.2 Thermal Sensitivity Shift (TSS)

The expected change in the sensitivity of the sensor as a function of temperature is the thermal sensitivity shift. It is usually expressed as a percent bandwidth change in sensitivity for a specified change in temperature such as ±2%FSO/50°C and is generally linear with moderate temperature changes. The thermal sensitivity shift specification is intended to apply within the compensated temperature range of the sensor when it has had adequate time to warm up. As the sensor is calibrated at the specific temperature of use, any errors due to thermal sensitivity shift can be eliminated or minimized by using sensitivity numbers determined at or near to the temperature of use. In our case the temperature of the working fluid was nearly same as the calibration temperature.

B.3.3 Zero Offset

The electrical output of the sensor when there is no applied pressure is the zero offset. For vented side sensors for gauge or relative pressure measurement, the zero offset is determined when the sensing side is at the same pressure as the vented side.

Appendix C Load Cells

C.1 Operating Principle and Design

Load cells are utilized in nearly every electronic weighing system. An entire system consists of load cells, cables, a junction box, signal conditioners and a data acquisition system. A load cell is classified as a force transducer since it converts force or weight into an electrical signal.

The strain gauge is the heart of a load cell; a device that changes resistance when a force is applied. The gauges are developed from an ultra-thin heat-treated metallic foil and are chemically bonded to a thin dielectric layer. "Gauge patches" are then mounted to the strain element with specially formulated adhesives. The precise positioning of the gauge, the mounting procedure and the materials used all have a measurable effect on the overall performance of the load cell. Each gauge patch consists of one or more fine wires cemented to the surface of the beam, ring or column (the strain element) within the load cell. As the surface to which the gauge is attached becomes strained, the wires stretch or compress changing their resistance in proportion to the applied load.

One or more strain gauges are used in a load cell. Multiple strain gauges are connected to create the four legs of a Wheatstone-bridge configuration. When an input voltage is applied to the bridge, the output is a voltage proportional to the applied force on the cell. The output can be amplified and processed by conventional electrical instrumentation. A detailed mathematical derivation is given in the following paragraphs.

A simple uni-axial link type load cell with strain gauges is shown in Figure C.1. The load P can be either a tensile load or a compressive load. The four strain gauges are

bonded to the link such that two are in the axial direction and two are in the transverse direction. The four gauges are wired to a Wheatstone bridge with the axial gauges in arms 1 and 3, and the transverse gauges in arms 2 and 4, as shown in Figure C.2.

When the load P is applied to the link, axial and transverse strains ε_a and ε_t develop in the link and are related to the load by expressions

$$\varepsilon_a = \frac{P}{AE} \tag{C.1}$$

and

$$\varepsilon_t = -\frac{\nu P}{AE} \tag{C.2}$$

where A is the cross-sectional area of the link, E is the modulus of elasticity of the link material, and ν is the Poisson's ratio of the link material. A strain gauge exhibits a resistance change $\Delta R/R$ that is related to the strain ε as

$$\frac{\Delta R}{R} = S_g \varepsilon \tag{C.3}$$

where S_g is the gauge factor or calibration constant for the gauge. The response of the gauges to the applied load P is given by using equations (C.1),(C.2) and (C.3) as

$$\frac{\Delta R_1}{R_1} = \frac{\Delta R_3}{R_3} = S_g \varepsilon_a = \frac{S_g P}{AE} \tag{C.4}$$

and

$$\frac{\Delta R_2}{R_2} = \frac{\Delta R_4}{R_4} = S_g \varepsilon_t = \frac{\nu S_g P}{AE} \tag{C.5}$$

The output voltage E_0 from the Wheatstone bridge can be expressed in terms of the load P by substituting equations (C.4) and (C.5) into the constant voltage Wheatstone bridge equation. Assuming that all the strain gauges on the link are identical i.e. $R_1 = R_2$ we get

$$E_0 = \frac{S_g P(1+\nu)E_i}{2AE} \tag{C.6}$$

or

$$P = \frac{2AE}{S_g(1+\nu)E_i} E_0 = CE_0 \tag{C.7}$$

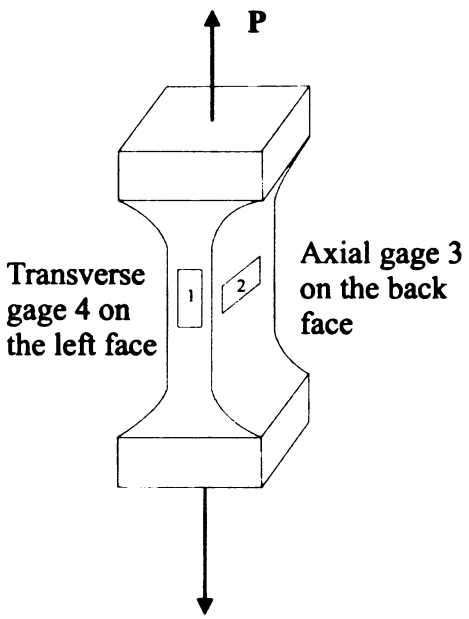

Figure C.1: Load cell elastic element with strain gages

Equation (C.7) indicates that the load P is linearly proportional to the output voltage E_0 and the constant of proportionality is $C = 2AE/S_g(1+\nu)E_i$. The sensitivity of the load cell-Wheatstone bridge combination is given by $S = E_o/P = 1/C$.

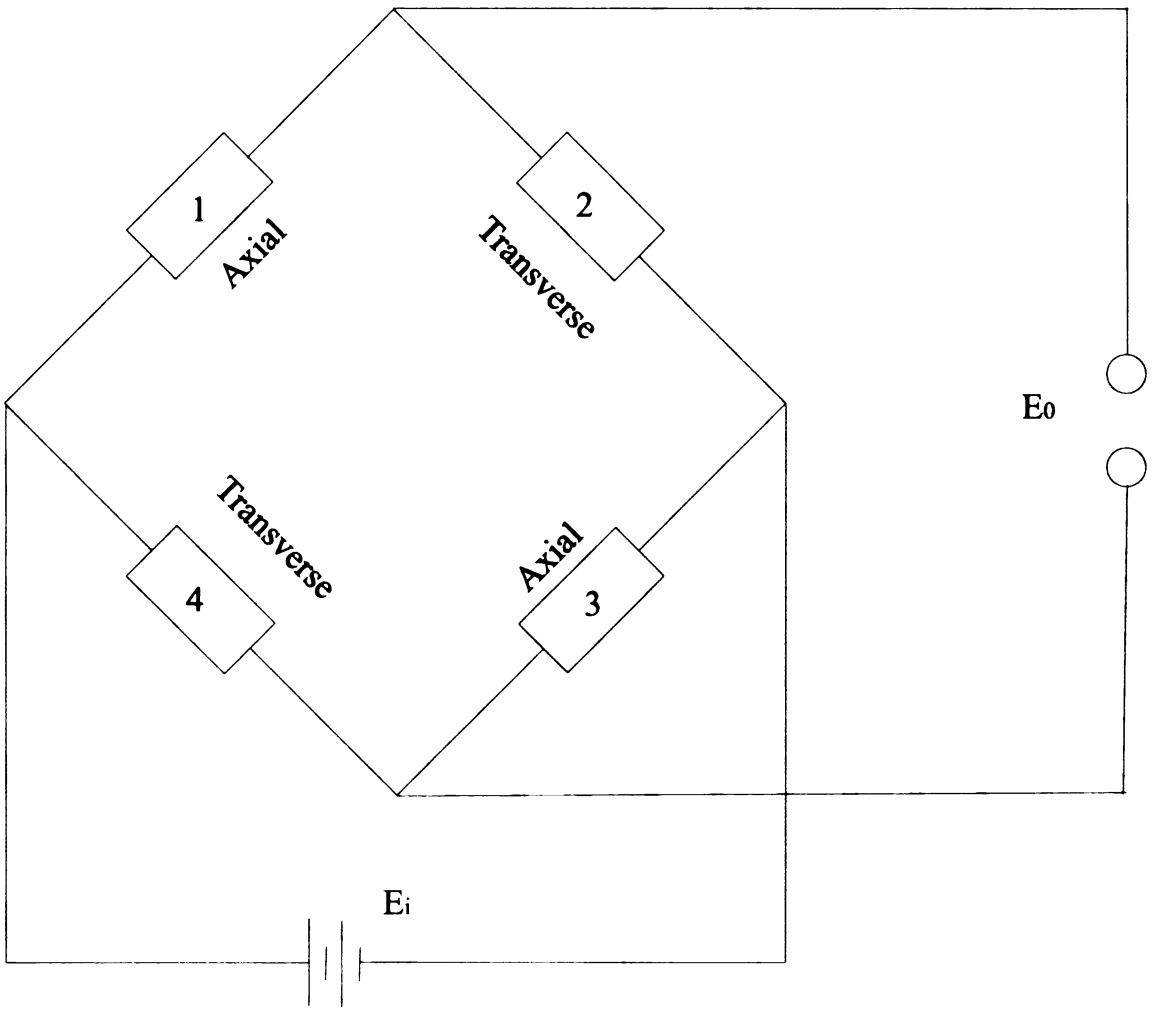

Figure C.2: Gage positions in the Wheatstone bridge.

C.2 Specifications of Load Cells

The technical specifications of Interface model SMT1-2.2 load cell and Futek model L2357 are given in Table C.1. The load cell specifications do not include the frequency response of these sensors. A frequency response analysis of each load cell was deduced and is described in the following paragraphs.

Specification	*SMT1-2.2*	*L2357*
Capacity	2.2 Lbs	5 Lbs
Rated Output (R.O.)	1 mV/V nom	1 mV/V nom
Excitation VDC	10 max	10 max
Non-Linearity	± 0.05% of R.O.	± 0.1% of R.O.
Hysteresis	± 0.03% of R.O.	± 0.1% of R.O.
Zero Balance	3% of R.O.	3% of R.O.
Temp. Shift Zero	± 0.15/100°F	± 0.004 - 0.01% of R.O./°F

Table C.1: Specifications of load cells

C.3 Frequency Response of the Load Cells

In order to analyze the quality of measurement under dynamic loading conditions, the response of the load cells to impulse and ramp inputs was analyzed. The frequency response for the two load cells was needed in order to evaluate the operating bandwidth of these sensors, as no data was available from the technical details provided by the respective manufacturers.

C.3.1 Impulse Response of the Load Cell

The most widely useful mathematical model for the study of measurement system dynamic response is the ordinary linear differential equation with constant coefficients. The relationship between any particular input q_i and output q_0 can be written in the form

$$a^n \frac{d^n q_0}{dt^n} + a^{n-1} \frac{d^{n-1} q_0}{dt^{n-1}} + \ldots + a \frac{dq_0}{dt} + a_0 q_0 = b^m \frac{d^m q_i}{dt^m} + b^{m-1} \frac{d^{m-1} q_i}{dt^{m-1}} + \ldots + b \frac{dq_i}{dt} + b_0 q_i \qquad \text{(C.8)}$$

For a second order system, equation(C.8) reduces to

$$a_2 \frac{d^2 q_0}{dt^2} + a_1 \frac{dq_0}{dt} + a_0 q_0 = b_0 q_i \tag{C.9}$$

Dividing equation (C.9) by a_0 and simplifying yields

$$\left(\frac{D^2}{\omega_n^2} + \frac{2\zeta D}{\omega_n} + 1 \right) q_0 = k q_i \tag{C.10}$$

where $k = b_0/a_0$ is the static sensitivity, $\omega_n = \sqrt{a_0/a_2}$ is the undamped natural frequency and $\zeta = a_1/2\sqrt{a_0 a_2}$ is the damping ratio. For a step input of the size q_{is}, the solution in the non-dimensional form is

$$\frac{q_o}{k q_{is}} = \frac{e^{-\zeta\, \omega_n t}}{\sqrt{1-\zeta^2}} Sin\left(\sqrt{1-\zeta^2}\, \omega_n t + \phi \right) + 1 \tag{C.11}$$

where $\phi = Sin^{-1}\sqrt{1-\zeta^2}$. In equation (C.11), the static sensitivity k was evaluated from the static sensitivity calibration curve. An experiment was carried out to evaluate the remaining parameters. In the particular experiment, a mass in the midrange of each sensor was dropped from a height of one inch from the load cell and its response was recorded at a sampling rate of about 1 KHz. From the known load and the steady output of the load cell, the parameters on the left-hand side of the equation (C.11) was determined. The damping ratio was calculated using the relationship

$$\delta = \ln\left(\frac{x_1}{x_2} \right) = \frac{2\pi}{\sqrt{1-\zeta^2}} \zeta \tag{C.12}$$

This gave the damping ratio as $\zeta = 0.51$. The natural frequency of the load cell was then calculated using the expression

$$\tau_d = \frac{2\pi}{\omega_n \sqrt{1-\zeta^2}} \tag{C.13}$$

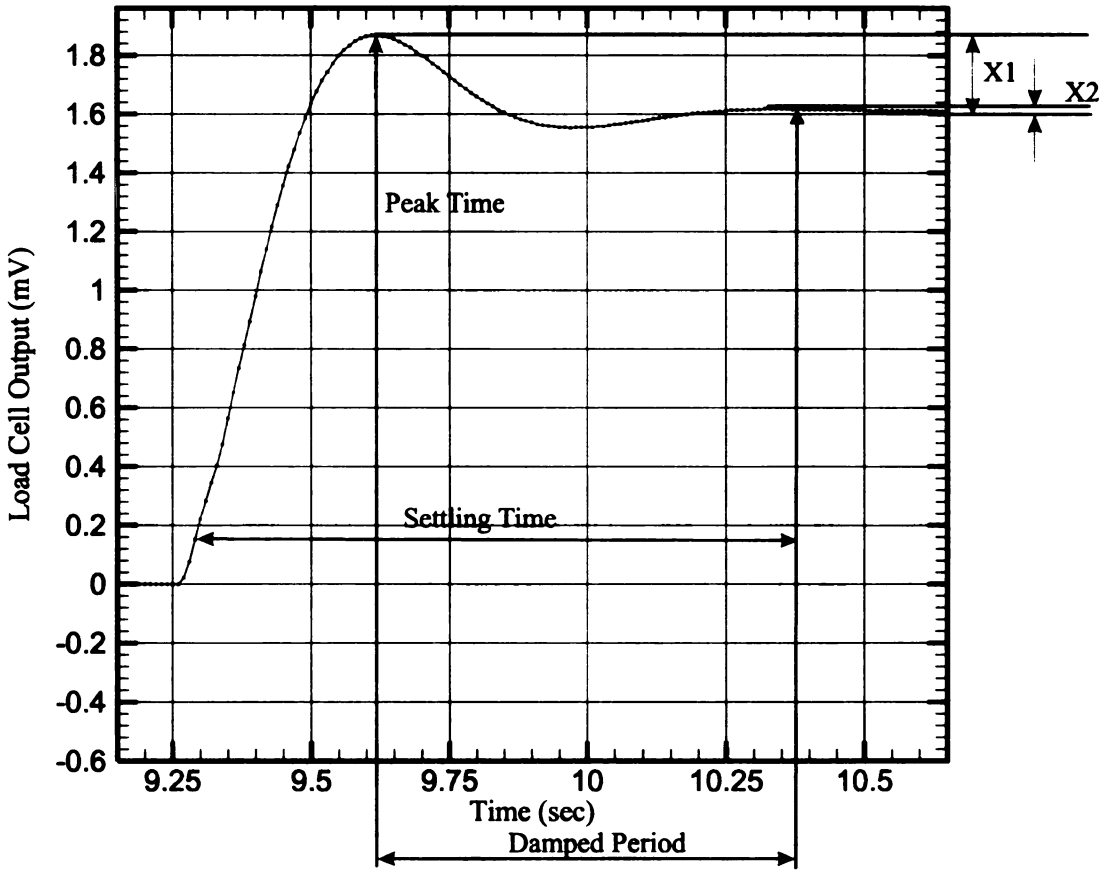

Figure C.3: Impulse response of the load cell.

where τ_d is the damped period between two successive peaks as shown in figure C-4. The amplitude response of the system was determined using the relationship

$$\frac{q_0}{kq_i} = -10\log\left[\left(1-(\omega/\omega_n)^2\right)^2 + 4\zeta^2(\omega/\omega_n)^2\right] dB \tag{C.14}$$

As can be observed from the Figure C.4, the amplitude response of the load cell is nearly flat for the lower frequencies, followed by an increase in the amplitude ratio ω_n, then attenuation. The bandwidth of the load cell was determined to be one radian per second for 95% accuracy. This value restricted the oscillating experiments that could be performed to within the limitation of 0.16 cycle per second or less.

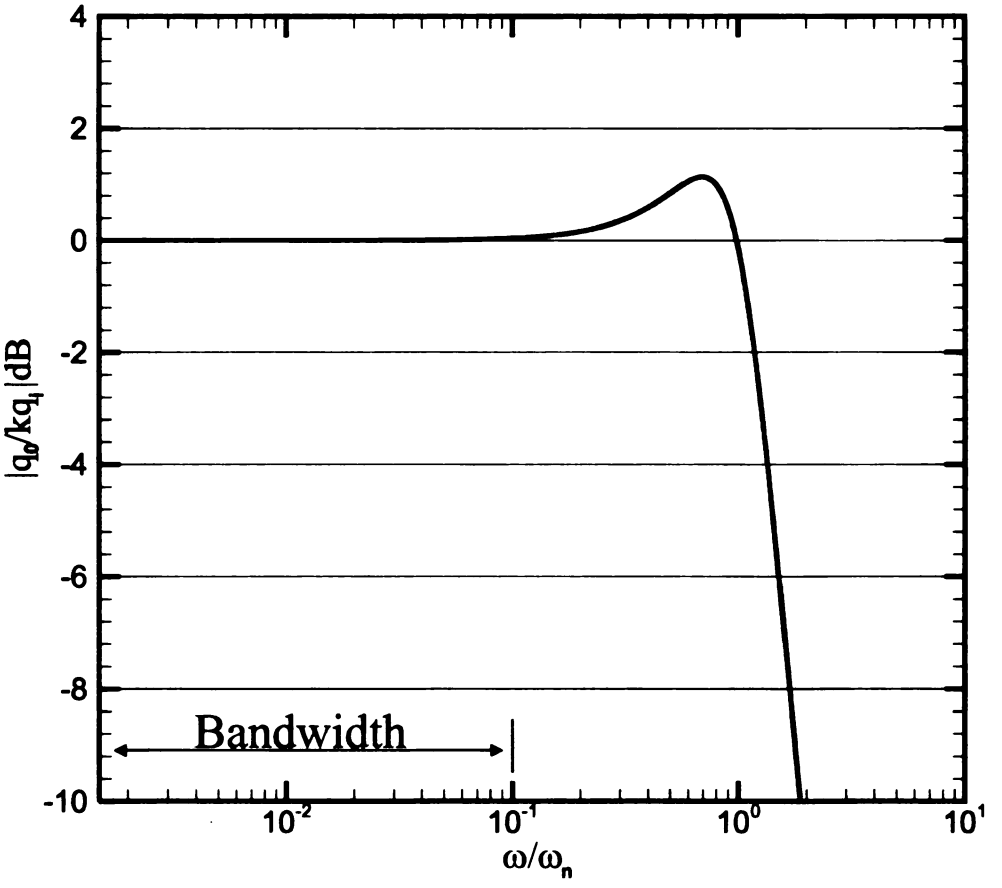

Figure C.4: Amplitude response of the load cell

C.3.2 Ramp Response of Load Cells

The ramp response of the load cell was determined by gradually increasing the load while recording the load cell output. The purpose of this experiment was to record the steady state time lag when collecting liquid mass during accelerating and decelerating flows.

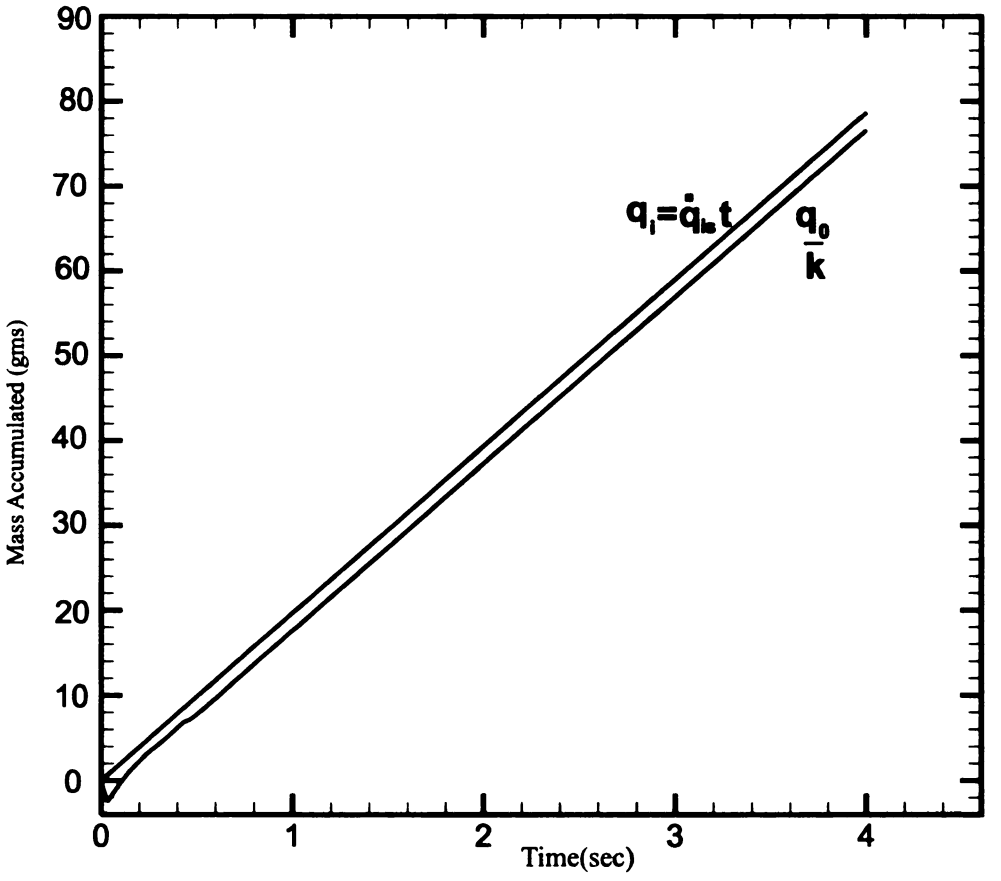

Figure C.5: Ramp response of load cell

The ramp response of the second order system is obtained by applying the initial conditions $q_0 = dq_0/dt = 0$ at $t = 0^+$ in equation (C.10). The solution of equation (C.10) is

$$\frac{q_0}{k} = \dot{q}_{is} t - \frac{2\zeta \dot{q}_{is}}{\omega_n}\left[1 - \frac{e^{-\zeta\,\omega_n t}}{2\zeta\sqrt{1-\zeta^2}} Sin\left(\sqrt{1-\zeta^2}\,\omega_n t + \phi\right)\right] \tag{C.15}$$

where

$$\tan\phi = \frac{2\zeta\sqrt{1-\zeta^2}}{2\zeta^2 - 1} \tag{C.16}$$

In the above expression, the steady state error is $2\zeta\dot{q}_{is}/\omega_n$, where $\dot{q}_{is}$ is the mass flow rate during accelerating and decelerating flow. The estimated steady state time delay was found as 0.1 second. The ramp response curve during accelerating flow is shown in Figure C.5.

Appendix D Sensor Thermal Sensitivity

Verification of Sensor Temperature Drift due to Heat Loss from Convection Heat Transfer

The thermal boundary layer develops within a laminar or turbulent hydrodynamic boundary layer over the sensor surface of diameter D_s in the streamwise directions. The thermal boundary layer is produced by a sudden jump in the surface temperature from a constant value of ambient temperature T_e to the higher constant value of T_0 as shown in the Figure D.1.

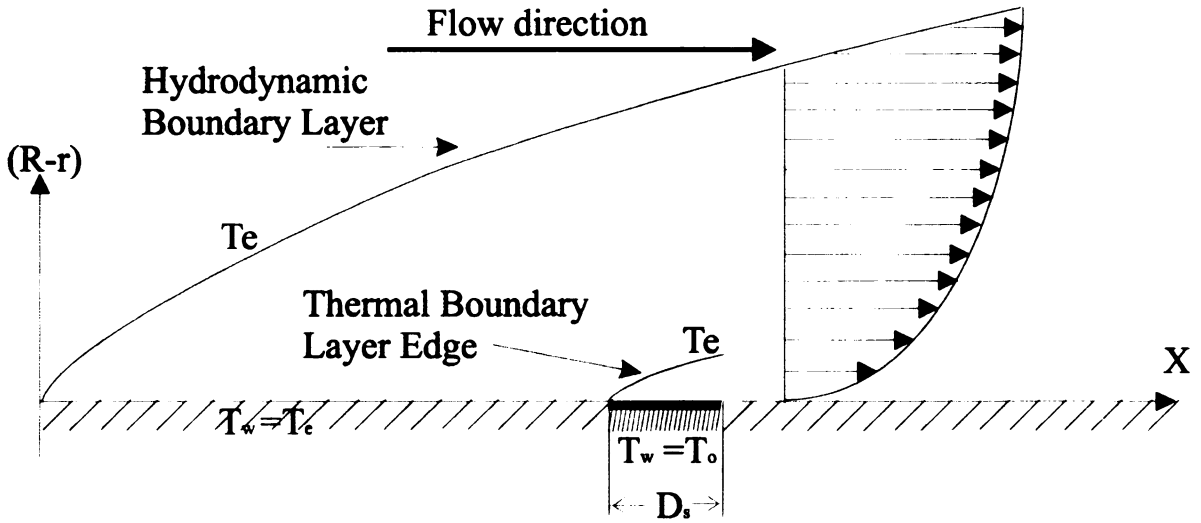

Figure D.1: Thermal boundary layer and related geometry

Due to high thermal drift of the sensors, it was decided to evaluate the temperature difference between the sensor surface and the fluid in contact with it. Higher thermal gradients would cause higher heat losses that might affect pressure sensor data. The analytical solution proposed by Ramaprian and Menendez [43] was used as a starting

point for this analysis. Ramaprian and Menendez gave the following results relating skin friction to the flush mounted rectangular hot-film gauge sensor heat transfer as

$$\tau_w = -\frac{\mu L}{(1-n)ac_p\rho k^2}\left(\frac{Q_{wl}}{\Delta T_0}\right)^3 + \frac{bk}{2a}\left(\frac{\partial p}{\partial x}\right)_L\left(\frac{\Delta T_0}{Q_{wl}}\right) + \frac{\mu L}{ak}\frac{Q_{wl}^2}{\Delta T_0}\frac{\partial}{\partial t}\left[\frac{c}{(1-n)Q_{wl}}\right] \quad \text{(D.1)}$$

here L is the length of the sensor, τ_w is the wall shear stress, Q_{wl} is the heat transfer from wall to the fluid at $x = x_0 + L$ and $\Delta T_0 = T_0 - T_e$. Equation (D.1) can be simplified using the assumptions that flow is steady with negligible pressure gradient along the sensor surface. Replacing the area of the hot film WL by the surface area of the pressure sensor, equation (D.1) becomes

$$\tau_w = -\frac{(1-n)^2\mu}{ac_p\rho k^2\pi r_s^3\Delta T_0^3}\left(\frac{E^2}{\mathbb{R}} - Q_s\right)^3 \quad \text{(D.2)}$$

where Q_s is the heat loss to the substrate, considered to be much less than the heat generated from the sensor. Replacing the wall shear stress term by the flow rate using the relations $Q = \pi D^4\Delta p/128l\mu$ and $\tau_w = \Delta pD/4l$ and rearranging for ΔT_0

$$(\Delta T_0)^3 = \frac{(1-n)^2 R^3}{8ac_p\rho k^2\pi r_s^3 Q}\left(\frac{E^2}{\mathbb{R}}\right)^3 \quad \text{(D.3)}$$

Using the values shown in the Table E.1, values of ΔT_0 were calculated for water and ethylene glycol solutions as 0.86 K and 0.687 K respectively at a Reynolds number of 1900. It was therefore concluded that a temperature difference of less than 1degree Kelvin was unlikely to have much effect in terms of convection heat transfer that might cause erratic output of the sensor.

Properties	***Ethylene Glycol***	***Water***
Shape factor (a)	0.23	0.23
n for laminar flow	0.29	0.29
ρ Density (kg/m^3)	1077	998
C_p constant specific heat ($J/Kg.K$)	3400	4181
K Thermal conductivity ($W/m.K$)	0.389	0.602
μ Dynamic viscosity ($kg/m.Sec$)	5.6×10^{-3}	9.68×10^{-4}
r_s Sensor radius (m)	1.18×10^{-3}	1.18×10^{-3}
E supply voltage ($Volts$)	5	5
R radius of the tube (m)	4.7625×10^{-3}	4.7625×10^{-3}
$\mathbb{R}$ sensor resistance ($ohms$)	1000	1000

Table D.1: Properties of the fluids and sensors used in equation (D.3)

E.1

kno

unc

exp

perc

X_i

i.e.

unc

and

E.2

instr

biase

the

by c

appa

calib

prese

Appendix E Uncertainty Analysis

E.1 Uncertainty Analysis

Every measurement includes some level of error, and this error can never be known exactly. However a probable bound on the error can be estimated, known as its uncertainty. The purpose of this appendix is to quantify the uncertainty in the experimental results presented earlier. The uncertainties are stated at a confidence percentage of 95% or odds of 19:1. The bound typically has the form $X_i = X_i(measured) \pm \delta X_i$ *(n:1)*, where δX_i is the uncertainty estimated at odds of *n:1* i.e. only one measurement in *n* will have an error greater than δX_i. When estimating uncertainty, two types of errors are normally considered: precision error (random error) and bias error (systematic error).

E.2 Bias Errors

These errors occur the same way each time a measurement is made i.e. if an instrument reads high by a certain percentage, then the entire set of measurements are biased by that percentage above the true value. Fixed offset errors also contribute towards the biased errors. The only direct method for uncovering bias error in a measurement is by comparison with measurement made using a separate and presumably more accurate apparatus. Bias uncertainty is also estimated using experience and understanding of calibrations and manufacturing tolerances. The estimate of the bias uncertainty is presented with a confidence level of 95%.

E.3 Precision Errors

Precision errors are also called the random errors. They may be different for each successive measurement but have an average value of zero. In this case readings of the same quantity differ slightly, creating a distribution of values surrounding the true value. In such cases, a statistical analysis can be carried out to estimate the likely size of the error. The precision error is presumed to behave randomly, with zero mean. The precision error in repeat-sampled data reveals its own distribution, enabling us to bound its magnitude using statistical methods. The potential precision error underlying a single measurement of a random variable can be estimated from the resolution of the instrument, the precision with which the instrument can repeat the reading and how much its reading fluctuates during the test.

E.4 Propagation of Uncertainty

If a calculated result is a function of several independent measured variables, then each measured value has some uncertainty and these uncertainties lead to an overall uncertainty in calculated results. Uncertainty in results due to uncertainty in independent variables is called the propagation of uncertainty, expressed mathematically (Beckwith et al. [44]) as

$$U_y = \left(\left(\frac{\partial y}{\partial x_1} u_1 \right)^2 + \left(\frac{\partial y}{\partial x_2} u_2 \right)^2 + \ldots\ldots + \left(\frac{\partial y}{\partial x_n} u_n \right)^2 \right)^{1/2} \qquad \text{(E.1)}$$

In the above expression all the uncertainties have the same odds and are independent of each other. The uncertainties U_y are either bias uncertainties or precision uncertainties. Both of these uncertainties propagate separately. The overall uncertainty U_y is calculated by combining B_y and P_y as

$$\frac{U_y}{y} = \left(\left(\frac{B_y}{y} \right)^2 + \left(\frac{P_y}{y} \right)^2 \right)^{1/2} \tag{E.2}$$

E.5 Uncertainty Analysis of Experimental Results

The uncertainty analysis of the data was carried out based on manufacturer's data sheets, calibration results and knowledge of the experimental procedures. In this research, the objective was to compare the cumulative mass inferred from pressure sensor data with true accumulated mass indicated by the load cell. The uncertainty of each measurement was recorded first and then the propagation of uncertainty was estimated based on these individual uncertainty measurements.

E.5.1 Uncertainty in Density Measurement

For the density of the working fluid, the volume of the fluid was measured using a graduated cylinder and the mass of the fluid contained in the cylinder was measured using an electronic weigh scale. The uncertainty in density measurements is tabulated below.

Parameter	Systematic Uncertainty (%)	Random Uncertainty (%)	Overall Uncertainty (%)
Mass	0.5	0.1	0.51
Volume	0.1	1	1.005
Density	0.5	1	1.12

Table E.1: Uncertainty in density, volume and mass

E.5.2 Uncertainty in Mean Velocity Measurement

The velocity of the fluid was measured using the relationship $U = \dot{m}/\rho A$, where $\dot{m}$ was calculated from the load cell data. The cross sectional area of the tube was determined as $A = (\pi/4)d^2$. The calculated uncertainty in velocity measurement is tabulated below.

Parameter	Systematic Uncertainty (%)	Random Uncertainty (%)	Overall Uncertainty (%)
Mass flow rate (load cell)	0.06	0.04	0.07
Pipe diameter	0.25	0	0.25
Velocity	0.1	1	1.004

Table E.2: Uncertainty in velocity, flow rate and diameter measurements

E.5.3 Uncertainty in Reynolds Number

The Reynolds number was an important parameter used to indicate whether flow was in the laminar or turbulent regime. The Reynolds number was calculated using the relationship $Re = Ud/\nu$, where the uncertainty in the velocity and pipe diameter has already been shown in table E.2. The kinematic viscosity was measured using a Cannon-Fenske viscometer. Although uncertainty measurements in viscosity involve the uncertainty in time due to errors associated with using a stopwatch, this is ignored since the time involved was relatively long, of the order of 80 seconds. The calculated uncertainty in the kinematic viscosity and the Reynolds number is tabulated overleaf.

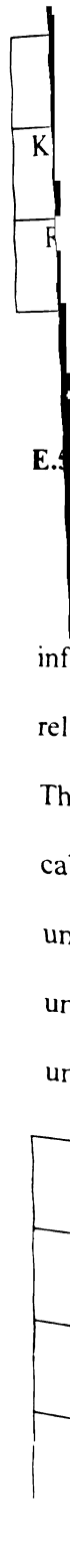

Parameter	Systematic Uncertainty (%)	Random Uncertainty (%)	Overall Uncertainty (%)
Kinematic viscosity	1	0.15	1.011
Reynolds number	1.3	1.4	1.91

Table E.3: Uncertainty in the Reynolds number and kinematic viscosity

E.5.4 Uncertainty in Pressure Drop and Inferred Accumulated Mass Measurements for Laminar Flow Experiments

Using the exact laminar flow relationship $\Delta p = 8\nu l\dot{m}/\pi R^4$, the pressure drop inferred from mass flow rate was used for the calibration of the pressure sensor. In this relationship, the uncertainty in all the parameters except length has already been discussed. The overall uncertainty in the pressure sensor calibration involves uncertainty in the calibration curve and uncertainty in the other factors in the above relationship. These uncertainties are combined in the overall uncertainty in the pressure drop data. The overall uncertainty in the inferred accumulated mass is tabulated below along with the uncertainties in length and pressure drop data.

Parameter	Systematic Uncertainty (%)	Random Uncertainty (%)	Overall Uncertainty (%)
Pipe length	0	0.25	0.25
Pressure drop	2.25	2.0	3.01
Inferred accumulated mass	2.7	2.0	3.36

Table E.4: Uncertainty in inferred accumulated mass, pressure drop, and pipe length measurement in laminar flow experiments

E

Th

un

to

un

ex

co

pr

b

E.5.5 Uncertainty in Pressure Drop and Inferred Accumulated Mass Measurements for Turbulent Flow Experiments

In this case the uncertainty in the pressure drop measurement was calculated first. The relationship $dp = \lambda\left(\frac{L}{d}\right)\frac{U^2\rho}{2}$ was used for calibrating the pressure sensor. The uncertainty in λ is associated with the Reynolds number since $\lambda = 0.316\, Re_d^{-0.25}$ was used to determine λ. The uncertainty in L, d, Re, ρ and U has been discussed earlier, when the uncertainty in pressure drop data was evaluated. For accumulated mass in turbulent flow experiments, the uncertainty in the evaluation of a or $v_t(0)$, and the uncertainty contribution due to R, ρ and ν was also considered. The uncertainties calculated in pressure drop and inferred accumulated mass in turbulent flow experiments are tabulated below.

Parameter	Systematic Uncertainty %	Random Uncertainty %	Overall Uncertainty %
a	1	0.25	1.03
Pressure drop	2.67	2.97	4.0
Inferred accumulated mass	3.07	3.15	4.4

Table E.5: Uncertainty in inferred accumulated mass, pressure drop and *a* measurement in turbulent flow experiments.

List of References

[1]. Arasi, T. A., "Results Mixed From Pulsating Flow Tests of Orifice –Plate Meter," Oil and Gas Journal, October 1992, pp 77-82.

[2]. Sexl, T., "Uber den von E.G. Richardson entdecten annulareffkt," Zeitschrift fur Physik, Vol. 61, 1930, pp.349.

[3]. Szymanski, P., "Some Exact Solutions of the Hydrodynamic Equations of a Viscous Fluid in case of a Cylindrical Tube," Journal Math. Pure et Applique'es, Vol. 11, pp 67-107.

[4]. Uchida, S., "The Pulsating Viscous Flow Superimposed on the Steady Laminar Motion of Incompressible Fluid in a Circular Pipe", Zeischrift fur angewandte Mathematik und Physik, Vol. 7, 1956, pp. 377.

[5]. Wormersley, J, R., " Method for the Calculation of Velocity Rate of Flow and Viscous Drag in Arteries When the Pressure Gradient is Known," Journal of Physiology, Vol. 127, 1955,pp.553.

[6]. Leonhard, A. "Determination of Transients Response from Frequency Response," "Frequency Response" edited, R. Oldenburger, The Macmillan Company, New York, N. Y., 1956.

[7]. Brown, F.T., "The Transient Response of Fluid Lines," ASME, Journal of Basic Engineering, vol. 84, Dec 1962, pp 547-553.

[8]. Brown, F. T., and Nelson, S. E., "Step Responses of Liquid Lines with Frequency Dependent Effects of Viscosity," Journal of Basic Engineering, Transaction. ASME, Series D, Vol. 87, No. 2, June 1965, pp. 504- 510.

[9]. D'Souza, A. F., and Oldenburger, R., "Dynamic Response of Fluid Lines," Journal of Basic Engineering, Transaction. ASME, Series D, Vol. 86, No. 3, Sept. 1964, pp. 589- 598.

[10]. Holmboe, E. L., and Rouleau, W. T., "The Effect of Viscous Shear on Transients in Liquid Lines," Transactions of ASME, March 1967, pp 174-180.

[11]. W. Zielke," Frequency-dependent Friction in Transient Pipe Flow," J. Basic Eng., Trans. ASME, 90, 109, (1968).

[12]. Trikha, A. K., "An efficient Method for Simulating Frequency-dependent Friction in Transient Liquid Flow," Journal of Basic Engineering, Transaction. ASME, Series D, Vol. 97, No. 1, March 1975, pp. 97-105.

[13]. Tsang, S. H. L., "Periodic Air Flow in Volume- Loaded Tubes by the Fast Fourier Transform Method Forum On Unsteady Flow-1986," The Winter Annual meeting of ASME, Anaheim California, December 1986, pp 13-15.

[14]. Lisheng, S., and Wylie, E. B., "Impulse Response Method for Frequency Dependent Pipe Line Transients," Journal of Fluid Engineering, Transaction. ASME, Vol. 111, December 1989, pp. 478-482.

[15]. Brereton, G. J., " The Interdependence of Friction, Pressure Gradient, and Flow Rate In Unsteady Laminar Parallel Flows," Physics of Fluids, Volume 12, Number 3, March 2000, pp 518-530.

[16]. Kataoka, K., Kawabata, T., and Miki, k., "The Start Up Response of Pipe Flow to a Step Change in Flow Rate," Journal of Chemical Engineering of Japan, Vol. 8, No. 4 1975, pp 266-271.

[17]. Muto, T., and Nakane, K., "Unsteady Flow in Circular Tube. Velocity Distribution of Pulsating Flow," Bulletin of the JSME, Vol. 23, No. 186, 1980, pp 1990-1996.

[18]. Kurokawa, J., and Morikawa, M., "Accelerated and Decelerated Flows in Circular Pipe," First Report, Bulletin of JSME, Vol. 29, No. 249, March 1986, pp 758-765.

[19]. Ohmi, M., and Iguchi, "Flow Patterns and Frictional Losses in Pulsating Pipe Flow. Part 6: Frictional Losses in a Laminar Flow," Bulletin of the JSME, Vol. 24, No. 196, 1981, pp 1756.

[20]. Hershy, D., and Song, G., "Friction Factors and Pressure Drop for Sinusoidal Laminar Flow of Water and Blood in Rigid Tubes," AIChE Journal, Vol. 13, No 3, 1967, pp. 491-496.

[21]. Yokota, S., Kim, D., and Nakano, K., " An Unsteady Flow Rate Measurement Method Utilizing Dynamic Characteristics Between Pressure and Flow Rate Along a Pipeline," JSME International Journal, Series III, Vol. 35, No. 4, 1992, pp591-597.

[22]. Shuy, E. B., " Wall Shear Stress in Accelerating and Decelerating Turbulent Pipe Flows", Journal of Hydraulic Research, Vol. 34, No 2, 1996, pp 173-183.

[23]. Lefebvre, P. and White, F., "Detailed Measurements of accelerating-Flow Properties in Pipes", Contributed papers in fluid engineering, ASME 1992, FED-Vol. 139, pp 27-35.

[24]. Jackson, J. D. and He, S., "A Study of Turbulence under Conditions of Transient Flow in a Pipe" J. Fluid Mech. Vol.408, 2000, pp 1-38.

[25]. Gerrard, J. H., "Experimental Investigation of Pulsating Water Flow in a Tube," Journal of Fluid Mechanics, Vol. 46, 1971, pp43-64.

[26]. Schultz-Grunow, F., " Pulsierrender Durchfluss durch Rohre," Forsch. Ing.-Wesen, 170, 1960.

[27]. Daily, J. W., Hankey, W. L., Olive, R. W., and Jordaun, J. M., " Resistance Coefficients for Accelerated and Decelerated Flows Through Smooth Tubes and Orifices," ASME Paper no 55-SA78, 1955.

[28]. Kirmse, R. E., " Investigation of Pulsating Turbulent pipe Flow", Transactions of ASME, Vol. 101, Dec 1979, pp 436-444.

[29]. Baired, M. H. I., Round, G. F. and Cardenas, J. N., " Friction Factors in Pulsed Turbulent Flow", The Canadian Journal of Chemical Engineering, Vol. 49, April 1971, PP. 220-223.

[30]. Ohmi, M., and Iguchi, "Flow Patterns and Frictional Losses in Pulsating Pipe Flow. Part 4: General Representation of Turbulent Frictional Losses," Bulletin of the JSME, Vol. 24, No.187, 1981, pp 67-74.

[31]. Ohmi, M., Kyomen, S. and Usui, T., "Analysis of Velocity Distribution in Pulsating Turbulent Pipe Flow with Time Dependent Friction Velocity," Bulletin of the JSME, Vol. 21, No.157, 1978, pp 1137.

[32]. Kita, Y., Adachi, Y. and Hirose, K., "Periodically Oscillating Flow in a Pipe", Bulletin of the JSME, Vol. 23, No.179, 1980, pp 656.

[33]. Brown, F. T., Margolis, D. L. and Shah, R. P., "Small Amplitude Frequency Behavior of Fluid Lines with Turbulent Flow," Journal of Basic Engineering, Transaction. ASME, Vol. 91, No. 4, 1969, pp. 678.

[34]. Gilbrech, D. A., and Combs, G. D., "Critical Reynolds Numbers for Incompressible Pulsating Flow in Tubes," Proceedings of the first Southeastern Conference on Theoretical and Applied Mechanics, 1962, pp. 292.

[35]. Lefebvre, P. J. and White, F. M., "Experiments on Transition to Turbulence in a Constant Acceleration Pipe Flow," Transaction of ASME, Vol. 111, December 1989, pp 428 –432.

[36]. Letheusser, H. J., and Lan, K. W., "Laminar to Turbulent Transition in Acceleration Motion," Proc. 17th Cong. IAHR, Part A118, pp 343-350.

[37]. Kataoko, K., Kawabata, T., and Miki, K., "The Start Up Response of Pipe Flow to a Step Change in Flow Rate," J. Chem. Eng. Japan, Vol.8, No 4, 1975, pp 266-271.

[38]. Van der Sande, E., "Velocity Profiles in Accelerating Pipe Flows Starting from Rest," Proc. 3rd int. Conf. On Pressure Surges, Canterbury, England, 1980, pp 1-14.

[39]. Moss, E. A., "The identification of Two Distinct Laminar to Turbulent Transition Modes in Pipe Flows Accelerated from Rest," Experiments in Fluids, Vol. 7, 1989, pp 271-274.

[40]. Ramaprian, B. R., and Tu, S. W., " An Experimental Study of Oscillatory Pipe Flow at Transitional Reynolds Numbers," J. Fluid Mech. Vol. 100, Part 3, 1980, pp 513-544.

[41]. Hino, M., Sawamoto, M., and Takasu, S., "Experiments on Transition to Turbulence in an Oscillatory Pipe Flow," J. Fluid Mech. Vol. 75, Part 2, 1976, pp 193-207.

[42]. Arpaci, S. V., and Larson, P. S., "Convection Heat Transfer," Prentice-Hall, 1984.

[43]. Ramaprian, B. R. and Menedez, A. N., " The Use of Flush-mounted Hot-film Gauges to Measure Skin Friction in Unsteady Boundary Layers," J. Fluid Mech. Vol. 161, 1985, pp 139-159.

[44]. Beckwith, T. G., Marangoni, R.D. and Lienhard, J. H., "Mechanical Measurements," Addison-Wesley Publishing Company, Inc., 5th Edition, 1993.

[45]. Watson, E. J., "Laplace Transform and Applications," Van Nostrand Reinhold, New York, 1980.

[46]. Streeter, V. L. and Wylie, E.B., "Hydraulic Transients," McGraw-Hill, New York, 1967.

[47]. White, F. M., "Fluid Mechanics," McGraw-Hill inc., 3rd Edition, New York, 1994.

[48]. Kim, J., Moin, P. and Moser, R., " Turbulence Statistics in Fully Developed Channel Flow at Low Reynolds Number," J. Fluid Mech. Vol. 177, 1987, pp 133-166.

[49]. Sandham, N. D., "A Model Equation for Transition and Turbulence in Plane Channel Flow," Eighth Symposium on Turbulent Shear Flows, Technical University of Munich, 1991.